Salt Coupled THMC Processes Research Activities at LBNL: FY2019 Progress

Spent Fuel and Waste Disposition

Prepared for

U.S. Department of Energy

Spent Fuel and Waste Science and Technology

Jonny Rutqvist, Yuxin Wu, Mengsu Hu, Michael Commer, Jiannan Wang, and Jens Birkholzer

Lawrence Berkeley National Laboratory

August 16, 2019

LBNL-2001230

SFWD Working Document: External Release

Revision 5
01/15/2018

APPENDIX E

NTRD DOCUMENT COVER SHEET [1]

Name/Title of Deliverable/Milestone/Revision No.	Salt Coupled THMC Processes Research Activities at LBNL: FY2019 Progress M3SF-19LB010303023
Work Package Title and Number	Salt Disposal R&D - LBNL/Salt International Collaborations - LBNL
Work Package WBS Number	SF-19LB01030302/ SF-19LB01030305
Responsible Work Package Manager	Jonny Rutqvist (signature on file)
	(Name/Signature)

Date Submitted **8/16/2019**

Quality Rigor Level for Deliverable/Milestone[2]	☐ QRL-1 Nuclear Data	☐ QRL-2	☐ QRL-3	☒ QRL 4 Lab-specific

This deliverable was prepared in accordance with Lawrence Berkeley National Laboratory (LBNL)
(Participant/National Laboratory Name)

QA program which meets the requirements of
☒ DOE Order 414.1 ☐ NQA-1 ☐ Other

This Deliverable was subjected to:

☐ Technical Review

Technical Review (TR)

Review Documentation Provided

☐ Signed TR Report or,
☐ Signed TR Concurrence Sheet or,
☒ Signature of TR Reviewer(s) below

Name and Signature of Reviewers

Kunhwi Kim (signature on file)
Boris Faybishenko (signature on file)

☐ Peer Review

Peer Review (PR)

Review Documentation Provided

☐ Signed PR Report or,
☐ Signed PR Concurrence Sheet or,
☐ Signature of PR Reviewer(s) below

Name and Signature of Reviewers

NOTE 1: *Appendix E should be filled out and submitted with each deliverable. Or, if the PICS:NE system permits, completely enter all applicable information in the PICS:NE Deliverable Form. The requirement is to ensure that all applicable information is entered either in the PICS:NE system or by using the FCT Document Cover Sheet.*

- *In some cases there may be a milestone where an item is being fabricated, maintenance is being performed on a facility, or a document is being issued through a formal document control process where it specifically calls out a formal review of the document. In these cases, documentation (e.g., inspection report, maintenance request, work planning package documentation or the documented review of the issued document through the document control process) of the completion of the activity, along with the Document Cover Sheet, is sufficient to demonstrate achieving the milestone.*

NOTE 2: *If QRL 1, 2, or 3 is not assigned, then the QRL 4 box must be checked, and the work is understood to be performed using laboratory specific QA requirements. This includes any deliverable developed in conformance with the respective National Laboratory / Participant, DOE or NNSA-approved QA Program.*

NOTE 3: *If the lab has an NQA-1 program and the work to be conducted requires an NQA-1 program, then the QRL-1 box must be checked in the work Package and on the Appendix E cover sheet and the work must be performed in accordance with the Lab's NQA-1 program. The QRL-4 box should not be checked.*

This page intentionally left blank.

CONTENTS

LIST OF FIGURES

LIST OF TABLES

ACRONYMS

BGR	Bundesanstalt für Geowissenschaften und Rohstoffe
CWIPP	Crushed Salt WIPP model
DOE	Department of Energy
DTS	Distributed Temperature SMRMTensing
EDM	Explicit Discretization Method
EDZ	Excavation Damaged Zone
ENSI	Swiss Federal Nuclear Safety Inspectorate, Switzerland
EOS	Equation-of-State
ERT	Electrical Resistivity Tomography
ETH	Swiss Federal Institute of Technology
EWASG	Equation-of-State for Water, Salt, Gas
FEM	Finite Element Method
FEPs	Features, Events and Processes
FLAC	Fast Lagrangian Analysis of Continua
FVM	Finite Volume Method
GRS	Global Research for Safety
LANL	Los Alamos National Laboratory
LBNL	Lawrence Berkeley National Laboratory
M-D	Multimechanism deformation
MINC	Multiple INteracting Continua
MRMT	Multi-Rate Mass Transfer
NE	Nuclear Energy
NCG	Non-condensable Gas
R&D	Research & Development
RTD	Resistance Temperature Detector
SFWD	Spent Fuel and Waste Disposition
SFWST	Spent Fuel and Waste Science and Technology
SNL	Sandia National Laboratories
TFC	TOUGH2-FLAC3D-Coupling
THM	Thermal-Hydrological-Mechanical
TH	Thermal-Hydrological
THMC	Thermal-Hydrological-Mechanical-Chemical
TM	Thermal-Mechanical
TOUGH	Transport of Unsaturated Groundwater and Heat
TSDE	Thermal Simulation for Drift Emplacement

TUC	Clausthal University of Technology, Germany
UFD	Used Fuel Disposition
UFDC	Used Fuel Disposition Campaign
WIPP	Waste Isolation Pilot Plant
XFVM	Extended Finite Volume Method

1. INTRODUCTION

Salt coupled THMC processes R&D activities are being conducted at Lawrence Berkeley National Laboratory (LBNL) as part of the Spent Fuel and Waste Disposition (SFWD), Spent Fuel and Waste Science and Technology (SFWST) program of the Department of Energy's (DOE) Office of Nuclear Energy (NE). These activities are focused on understanding and modeling coupled processes and impacts of the Excavation Damaged Zone (EDZ) and high-temperature on parameters and processes relevant to performance of a salt repository. Salt coupled THMC processes in salt host rocks are particularly complex, as heat released from the waste package will trigger strongly coupled Thermal-Hydrological-Mechanical-Chemical (THMC) processes that could impact the long-term performance of a nuclear waste repository.

Given the complexity of these interrelated processes and the time scales that need to be considered (typically, thousands or even millions of years for heat-generating nuclear waste), the performance assessment of an underground repository requires an application of suitable numerical modeling based on the state-of-the-art and physically-based knowledge. Since 2012, LBNL's work related to Salt R&D has been focused on developing and testing of a numerical modeling tool that can be applied to predict coupled THMC processes associated with nuclear waste disposal in salt formations. The work has a strong component of international collaboration with Clausthal Technical University (TUC) in Germany, a world leading institution on salt geomechanics testing and modeling. LBNL and TUC collaborate on development and application of coupled THMC models, including the development and testing of advanced constitutive models for evaluating the long-term coupled THMC behavior of salt.

The THMC model under development has the capabilities of predicting important coupled processes illustrated in Figure 1-1, including the long-term compaction and permanent sealing the repository tunnels. However, there are considerable uncertainties in the input parameters and material properties for such a complex THMC model. Field testing and interpretative modeling of such field tests are the most effective methods for reducing the uncertainties in evaluation of parameters and to increase the understanding of the different processes affecting the long-term behavior of salt host rock exposed to high temperature.

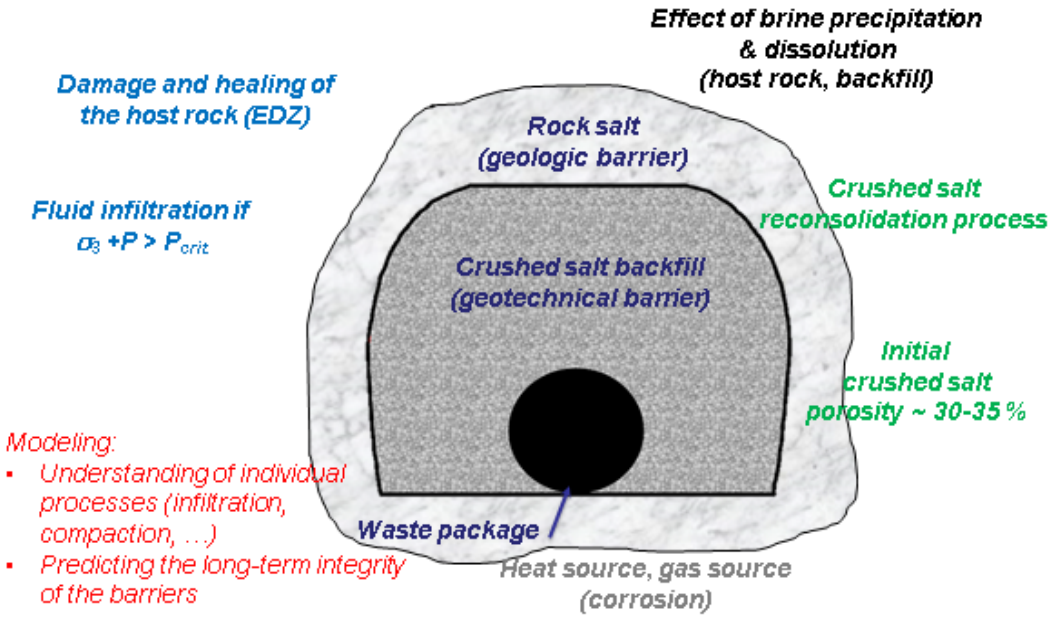

Figure 1-1. Schematic illustration of coupled THMC processes around a nuclear waste emplacement drift in salt.

The research activities of LBNL address the key Features, Events and Processes (FEPs), which have been ranked in importance from medium to high, as listed in Table 7 of the Research and Development Roadmap (FCRD-USED-2011-000065 REV1) (Nutt 2012). Specifically, they address FEP 2.2.01, Excavation Disturbed Zone, for salt, by investigating how coupled processes affect EDZ evolution; FEP 2.2.05, Flow and Transport Pathways; FEP 2.2.08, Hydrologic Processes; and FEP 2.2.07, Mechanical Processes by studying near-field coupled Thermal-Hydrological-Mechanical (THM) processes in salt repositories. The activities documented in this report also address a number of research topics that were identified in R&D Plan for the previous DOE-NE Used Fuel Disposition Campaign (UFDC) Natural System Evaluation and Tool Development (Wang, 2011), including Topics S3, Disposal system modeling – Natural system; P14, Technical basis for thermal loading limits; and P15 Modeling of disturbed rock zone evolution (salt repository).

This report documents LBNL's FY2019 Salt R&D Milestone M4SF-19LB010303021, related to LBNL's research activities on salt coupled THMC processes. In particular, LBNL conducts coupled THM modeling in support of the design of a small-diameter borehole heater test that is conducted at the Waste Isolation Pilot Plant (WIPP) (Kuhlman et al., 2018; Johnson et al., 2018; Mills et al., 2019). LBNL modeling support of the experiment is focusing on THM mechanisms of brine-release and brine-inflow and borehole mechanical closure rate for both heated and non-heated borehole experiments. In addition to the coupled THM modeling, LBNL also provides support of the experimental design for the monitoring of the planned small diameter borehole test, in particular related to Cross-borehole Electrical Resistivity Tomography (ERT) as well as fiber optical sensing of temperature and strain.

The structure of the report is as follows. In Section 2, we provide an overview of LBNL's work within the DOE-NE, SFWST (and former Used fuel disposition (UFD)) Salt R&D program during FY12-FY19. In Section 3, we report the status of the Transport of Unsaturated Groundwater and Heat (TOUGH)–Fast Lagrangian Analysis of Continua (FLAC) simulator for modeling salt-coupled processes. In Section 4, we present the status of the development and testing of a new dual continuum model for brine-migration, including brine inclusions in salt grains. In Section 5, we present new results of the BenVaSim code comparison project. In Section 6, we summarize the LBNL's new modeling activities related to the small-diameter field test at WIPP. In Section 7, we present the results of an ongoing work on geophysical monitoring of coupled processes during the salt heater testing at WIPP. In Section 8, we conclude with a summary of achievements in FY19 and proposed work for FY20.

2. OVERVIEW OF LBNL SALT R&D PROGRESS IN FY 2012-2019

LBNL's work on the modeling of coupled THMC processes in salt was initiated in FY12, focusing on exploring and demonstrating the capabilities of an existing LBNL modeling tool (TOUGH-FLAC) for simulating temperature-driven coupled flow and geomechanical processes in salt. The TOUGH-FLAC simulator (Rutqvist, 2011; 2017) is based on linking the TOUGH2 multiphase flow and heat transport simulator (Pruess et al., 2012) to the FLAC^{3D} geomechanical simulator (Itasca, 2011). In this approach, TOUGH2 is used for solving multiphase flow and heat transport equations, whereas FLAC^{3D} is used for solving geomechanical stress-strain equations.

An important component in this code development and applications is LBNL's collaboration with a research group led by Professor Lux at Clausthal University of Technology (TUC) in Germany, a world-leading research institution in salt geomechanics. The DOE-NE and LBNL have greatly benefited from TUC's experience in salt geomechanics and modeling of salt thermal-mechanical (TM) processes using FLAC^{3D}. Similarly, TUC has benefited from LBNL's expertise in modeling multiphase and heat transport processes at high temperature with TOUGH2, as well as LBNL's experience with the TOUGH-FLAC simulator, for the modeling coupled THM processes, which are expected to take place in the subsurface due to nuclear waste isolation. By leveraging on existing complementary capabilities of the LBNL and TUC, we have developed and validated an advanced state-of-the-art numerical simulation tool for modeling of coupled THM processes in salt and have demonstrated its applicability to the problems associated with nuclear waste isolation. A summary of collaboration between LBNL and TUC for the period since 2012 is given below.

In FY13, the work was focused on implementation and testing of constitutive models for salt host rocks and crushed salt. In particular, we implemented the *Lux/Wolters* model for modeling of creep, damage, sealing, and healing of the salt as a function of stress, temperature, and pore pressure. We used the TOUGH-FLAC code with this newly implemented model together with other constitutive models for crushed salt backfill, and for the first time successfully completed model simulations of a generic salt-based repository for a period of over 100,000 years.

In FY14, LBNL's work was focused on testing, application, and improvement of TOUGH-FLAC relevant to spend fuel disposal in salt. This included improvements to the TOUGH-FLAC simulator related to salt constitutive models and the use of a Voronoi discretization to improve accuracy of flow simulations. Based on these model improvements, updated simulations of long-term THM behavior of a generic repository were performed, and we conducted code benchmarking in collaboration with the TUC research team.

In FY15, we conducted further verification, validation, and application of the TOUGH-FLAC model. We conducted the first full 3-D (86,000 elements) TOUGH-FLAC modeling of a salt repository (heater experiment); the Thermal Simulation for Drift Emplacement (TSDE) test in Asse Mine, Germany, and extended TOUGH-FLAC for simulations of salt precipitation and dissolution, i.e., coupled THMC processes. The following two journal papers were published in peer-reviewed journals in FY15:

- Blanco-Martín et al. (2015a), "Long-term modeling of the thermal-hydraulic-mechanical response of a generic salt repository for heat-generating nuclear waste" in *Engineering Geology*.
- Blanco-Martín et al. (2015b), "Comparison of two simulators to investigate thermal-hydraulic-mechanical processes related to nuclear waste isolation in saliniferous formations" in *Computers and Geotechnics*.

The above-mentioned long-term modeling included updated two-phase flow properties, capillary pressure curves, which are generally not available for natural salt, and improved modeling of water filtration induced at high pore-pressure.

In FY16, we completed the code validation against the Asse Mine TSDE experiment, and published the results in a peer-reviewed journal paper:

- Blanco-Martín et al. (2016), "Thermal-hydraulic-mechanical modeling of a large-scale heater test to investigate rock salt and crushed salt behavior under repository conditions for heat-generating nuclear waste" in *Computers and Geotechnics*.

Modeling of the TSDE resulted in the evaluation of updated creep deformation parameters for salt rock, parameters that are difficult to determine in laboratory. In FY16, we also conducted model validation against a 1980s *in situ* brine-release experiment at WIPP, Room A1, as well as new model verification against analytical solutions.

In FY17, we continued THM model development, verification and validation, with the purpose of providing support to the phased field test plan, involving the design of the initial small-diameter borehole heater test. Another peer-reviewed journal paper was published related to the extension of the TOUGH-FLAC simulator to large deformations that is necessary for modeling drift closure and compaction of backfill:

- Blanco-Martín et al. (2017), "Extension of TOUGH-FLAC to the finite strain framework" *Computers & Geosciences*.

Related to the planned small-diameter borehole heater test at WIPP, in FY17, we conducted modeling focusing on THM mechanisms for brine-inflow and estimated of borehole closure, and conducted modeling of historic borehole closure experiments at WIPP. A continuum modeling approach for migration of brine inclusions and a new coupled THM approach based on finite volume method were launched.

In FY18, the work within salt R&D was focused the development of a test plan for the small-diameter borehole test at WIPP, including coupled THM modeling in support of the design of the experiment, and ERT instrumental testing. Along with these activities, LBNL has continued a main task of salt THMC coupled processes model development, including TOUGH-FLAC and the dual-continuum model for brine migration. Another journal paper was published related to the model development, testing and application of TOUGH-FLAC:

- Blanco-Martín et al. (2018), "Coupled Processes Modeling in Rock Salt and Crushed Salt Including Halite Solubility Constraints: Application to Disposal of Heat-Generating Nuclear Waste" in *Transport in Porous Media*.

In FY19, we have continued the design and implementation of the small-diameter borehole test at WIPP in coloration with Sandia National Laboratories (SNL) and Los Alamos National Laboratory (LANL), with much more emphasis on field work in addition to the coupled THM modeling. We continue our collaboration with the Clausthal University of Technology (TUC) in upgrading TOUGH-FLAC with improved salt constitutive models, whereas most efforts have been focused on field work at WIPP for implementing geophysical monitoring methods and on modeling the small-diameter diameter borehole test.

3. STATUS OF TOUGH-FLAC SIMULATOR FOR SALT COUPLED PROCESSES

Since 2013, the TOUGH-FLAC simulator (Rutqvist et al., 2002; Rutqvist, 2011) has been adapted for modeling salt coupled THM processes and brine migration. As mentioned, an important component in this work is LBNL's international collaboration with the TUC in Germany. Through the collaboration with TUC, we have implemented an advanced constitutive model for salt geomechanics, the *Lux/Wolters* model, and have closely collaborated on improving the TOUGH-FLAC simulator along with a model verification, validation and application related to the short- and long-term performance of nuclear waste disposal in salt formations. In the following subsections we present more details on the status of the TOUGH-FLAC, including the status of the numerical framework for coupled THM modeling and salt geomechanics constitutive models, followed by a list of completed code verification and validation.

3.1 TOUGH-FLAC Coupled THM Framework

Figure 3-1 shows a schematic of linking of TOUGH2 and FLAC^{3D}, and Figure 3-2 shows a schematic of the sequential coupling of the two codes. The main advantages of such a sequential coupling scheme include the use of existing robust and well-established simulators for each subproblem, the resolution of smaller systems of equations, the use of different time-stepping algorithms, and the possibility to study different domains in each subproblem (Dean et al., 2006). The coupling scheme between TOUGH2 and FLAC^{3D} is based on the fixed stress-split method (Kim et al., 2011). In this method, the flow problem is solved first (with an explicit evaluation of the volumetric total stress), and the pore pressure and temperature are prescribed during the geomechanical calculation, which therefore requires drained rock-mechanical properties, i.e., properties obtained when pore-fluid is able to dissipate during loading (Kim et al, 2011).

In order to accommodate the large strains and time-dependent processes associated with saliniferous materials (creep, mesh distortions, crushed salt reconsolidation, etc.), TOUGH-FLAC required some updates. Indeed, FLAC^{3D} has the capability to deal with large strains, but TOUGH2 does not. TOUGH-FLAC included an algorithm to update the mesh in the flow subproblem as the geomechanics mesh deforms (Blanco-Martín et al., 2017). The balance equations solved in TOUGH2 account for geometrical changes to ensure mass conservation. This way, after every FLAC^{3D} call, mass is conserved, but density is not. The geometrical update is made at the first iteration of the TOUGH2 Newton-Raphson process (Pruess et al., 2012). In this iteration, the primary variables (pore pressure, temperature, and saturation) and porosity remain equal to those at the end of the previous time step (only geometrical data are different), and we check whether the system continues to be in thermodynamic equilibrium for a new time increment and new geometry. If the maximum residual exceeds a preset convergence tolerance, an iterative process is carried out. In this process, the geometry is kept unchanged (i.e., the geometry is updated in TOUGH2 after every FLAC^{3D} call, but is constant during each TOUGH2 run) and consistency in the balance equations is ensured through the porosity-variation formulation, adapted from (Kim et al., 2012). The balance equations for a grid block *n* read:

$$\frac{d\left(M_n^\kappa V_n\right)}{dt} = \sum_m A_{nm} F_{nm}^\kappa + q_n^\kappa \rightarrow \frac{dM_n^\kappa}{dt} + M_n^\kappa \frac{dV_n}{Vdt} = \frac{1}{V_n}\left(\sum_m A_{nm} F_{nm}^\kappa + q_n^\kappa\right) \tag{3.1}$$

for κ=[1, *NK*], and *NK* is the total number of fluid components—air, water, etc. In Equation (3.1), M_n^κ is the accumulation term, V_n is the volume of the grid block (new volume after FLAC^{3D} call), q_n^κ represents the sink/sources, and F_{nm}^κ is the flux of component κ across surface A_{nm} (new value after FLAC^{3D} call). Note that for second and further iterations, the term $M_n^\kappa \frac{dV_n}{Vdt}$ is not computed. The accumulation terms read

$$M_n^\kappa = \phi \sum_\beta S_\beta \rho_\beta \chi_\beta^\kappa \tag{3.2}$$

where ϕ is porosity, S_β is the phase saturation, ρ_β is the density of phase β, and χ_β^κ is the mass fraction of component κ in phase β. Porosity changes during a time step (for second and further iterations) are calculated adding a porosity variation $d\phi$, which includes a correction term, $\Delta\phi$, from geomechanics (therefore, it accounts for volume changes). This term is constant for a given time step. This way, the geometrical data used during the iterations of a time step are consistent, and mass conservation is ensured. The porosity variation has the form

$$d\phi = A(\alpha, \phi, K)dP + B(\alpha_{th})dT + \Delta\phi \tag{3.3}$$

where α [-] is the Biot coefficient, α_{th} [K^{-1}] is the linear thermal expansion coefficient, K [MPa] is the drained bulk modulus, and $\Delta\phi$ is the porosity correction from geomechanics. A detailed explanation of this formulation can be found in Kim et al. (2012).

In a TOUGH-FLAC simulation, TOUGH2 moves the simulation forward, and FLAC^{3D} is executed once within a TOUGH2 time step, just before the Newton-Raphson iteration process to solve the residual nonlinear equations (Figure 3-2). The pressure, P^n, temperature, T^n, liquid saturation, $S_l{}^n$, and porosity, ϕ^n, of each grid block computed at the end of the previous time step (from t^{n-1} to t^n) are transferred to FLAC^{3D}. Note that the pressure transferred depends on the definition of pore pressure, such as weighted average of liquid pressure and gas pressure (Coussy, 2004; Kim et al., 2013).

For coupling direction from fluid flow to geomechanics, the pore-pressure change, $\Delta P=P^n-P^{n-1}$, and the temperature change, $\Delta T=T^n-T^{n-1}$, corresponding to two successive TOUGH2 time steps are accounted for as a correction to the total stress tensor, σ_{ij} (direct coupling). These changes are computed internally in FLAC^{3D} once the new values P^n and T^n are transferred. The corrected total stress tensor, σ_{ij}^c, has the form

$$\sigma_{ij}^c = \sigma_{ij} - \alpha\Delta P\delta_{ij} - 3\alpha_{th}K\Delta T\delta_{ij} \tag{3.4}$$

where δ_{ij} [-] is the Kronecker delta. Compressive stresses are defined negative here. From Equation (3.4), it can be inferred that the coupling from flow to geomechanics (TOUGH2 to FLAC^{3D}) affects only the volumetric component of the stress tensor. Porosity and liquid saturation are used to update the body forces in the quasi-static governing equations of the geomechanical analysis (Kim et al., 2012). Note that these equations account for the thermal strains that result from the temperature change ΔT.

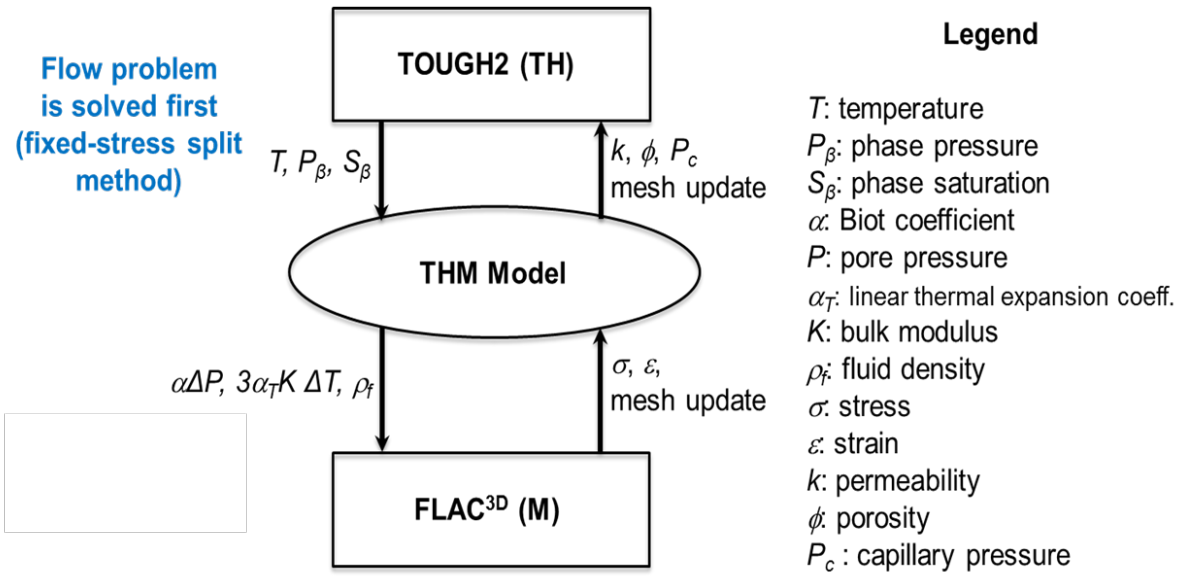

Figure 3-1. Schematic diagram of linking of TOUGH2 multiphase and heat transport simulator with FLAC^{3D} geomechanical simulator for modelling coupled.

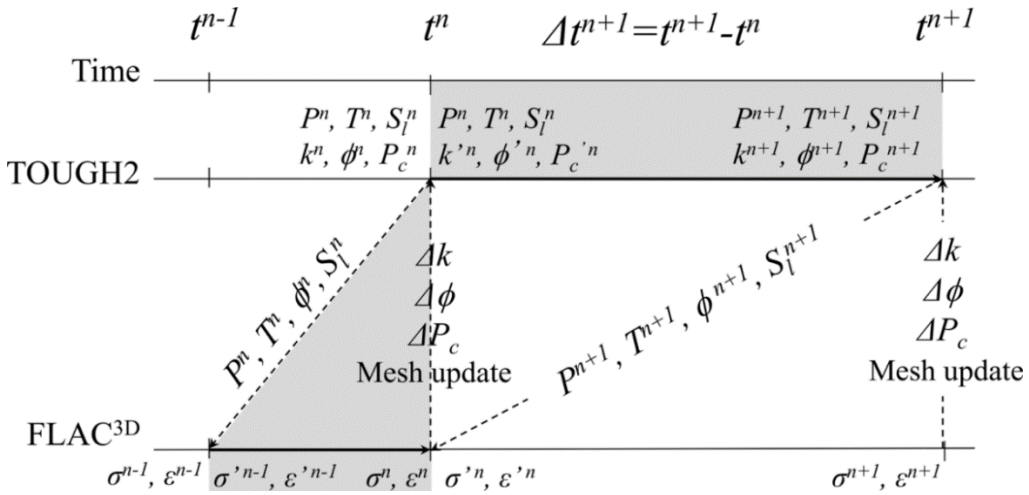

Figure 3-2. Explicit sequential THM analysis scheme (adapted from Rutqvist et al., 2002). The highlighted zones correspond to the time step between times t^n and t^{n+1}.

Once all the updates are made, FLAC^{3D} runs in creep and large strain modes from time t^{n-1} to time t^n. A new equilibrium mechanical state is obtained at time t^n (stresses σ^n and strains ε^n in Figure 3-2). In FLAC^{3D} the new static equilibrium is established internally through a dynamic-solution approach, solving the equation of motion in which the inertial terms are used as numerical means to reach the equilibrium state of the system under consideration. The established new static equilibrium brings about a new strain tensor and a new effective stress tensor (i.e., a new mechanical state).

From geomechanics to flow, geometrical changes are first incorporated. The geometrical data updated in TOUGH2 are volume of the elements, distances of the centroids of two connected elements to their common interface, common interface area, and cosine of the angle between the gravitational acceleration vector and the line between the centroids of two connected elements. In addition, as explained before, in the first

Newton-Raphson iteration, the accumulation terms in the balance equations are updated to account for possible volume changes.

Additionally, the new mechanical state obtained at t^n is used through several coupling functions to compute mechanically induced changes in permeability and capillary pressure (Δk and ΔP_c in Figure 3-2). The coupling functions depend on each material (and the phenomena it goes through) and should be based on specific laboratory and theoretical results. The mechanically modified flow properties (k'^n, ϕ'^n and $P_c'^n$ in Figure 3-2) are used to solve the residual equations of the flow problem. Within each time step, the Newton-Raphson iteration process is continued until the residuals are reduced below a preset convergence tolerance. At the end of the current time step (time t^{n+1} in Figure 3-2), a new set of primary thermodynamic variables (P^{n+1}, T^{n+1} and S_l^{n+1} in Figure 3-2) and new flow properties (k^{n+1}, ϕ^{n+1} and P_c^{n+1} in Figure 3-2) are obtained.

In TOUGH-FLAC, Voronoi discretization can be used in the flow subproblem, even when the mesh deforms over time due to the creep and the large strains. Since the resolution method used in TOUGH2 is based on the Voronoi partition (Pruess et al., 2012), more accurate solutions will be obtained when the discretization of the flow subproblem conforms to this technique. If the domain under study deforms over time, the partition used in the flow subproblem should still comply with the resolution method of the code. Bearing this in mind, we use the software library Voro++ (Rycroft, 2009) to ensure that the mesh used in TOUGH2 conforms to the principles of the Voronoi tessellation.

As the mesh deforms in the geomechanics subproblem, Voro++ is executed to compute the corresponding Voronoi tessellation. This operation is performed every time the mesh deforms with respect to strains a preset value, typically 2–5 % (Benz, 2007). In the current approach, the centroids of the deformed geomechanical mesh are transferred to Voro++, which computes the corresponding Voronoi discretization. Geometrical data of the new Voronoi mesh (volumes, common interface area between two adjacent grid blocks, etc.) are then transferred to TOUGH2.

Figure 3-3 shows a detail of two grids (flow and geomechanics) used in a THM simulation (initial mesh and deformed mesh after 20 years). As can be seen, the flow subproblem uses Voronoi cells, both in the initial and the deformed configurations. The grid blocks at the boundary between two different domains (waste package, backfill, and host rock) are slim and have the same thickness (Figure 3-3). In this way, Voro++ will conserve the volume of each domain even when the mesh deforms (the generators of the Voronoi mesh are the centroids of the mesh used in FLAC^{3D}).

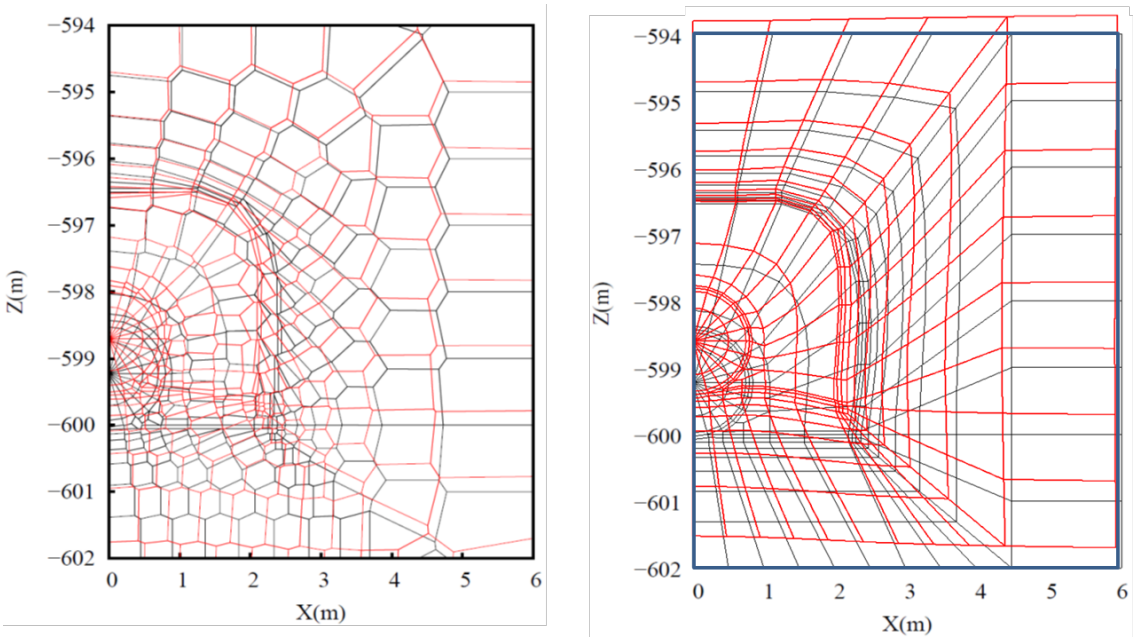

Figure 3-3. Mesh update in large strain mode. Example of initial and deformed discretization in the (left) flow subproblem and (right) geomechanics subproblem.

TOUGH-FLAC can also consider the flow of brine and halite dissolution/precipitation effects. This means that we consider three components in the flow subproblem: water, air, and halite. The liquid phase is composed of brine (solution of halite in water) with dissolved air. Halite (sodium chloride, NaCl) is very soluble in water, and solubility increases with temperature. However, if the mass fraction of halite in the liquid phase exceeds the solubility limit (which is a function of temperature), precipitation of solid halite will occur. Conversely, dissolution of solid salt will occur if the mass fraction of halite in the liquid phase is lower than the solubility limit at the current temperature. Halite solubility constraints introduce a new phase into the flow subproblem, so that in addition to the gas and liquid phases, a solid phase is also possible.

The flow of brine and halite dissolution/precipitation are considered in TOUGH-FLAC by the use Equation-of-State for Water, Salt, Gas (EWASG), an equation-of-state (EOS) module of TOUGH2 (Battistelli et al., 1997; Battistelli, 2012; Pruess et al., 2012), which effectively account for the thermo-physical properties of fluids of variable salinity. EWASG was developed for the modeling of hydrothermal systems containing salt and a non-condensable gas (NCG), such as air. The standard version of this EOS fluid property module has been recently improved to overcome some limitations (Battistelli, 2012), some of which are related to the correlations used for brine and halite, and which were derived from different sources (with a potential risk for limited internal coherence). Additionally, the effects of NCG were evaluated with an approach limited to low partial pressures.

Currently, the TOUGH-FLAC numerical THM framework includes the most relevant coupled THM processes, including multiphase fluid flow (advective flow and diffusion), heat transfer (advective and conductive), and non-linear geomechanics. In the current model, osmotic suction is not considered and the advective flow is exclusive taking place in the connected pore network between salt grains. One potential important process currently not included is the migration of brine through the movement of small brine-filled inclusions within salt crystals. In Section 4, we present the development of continuum model related to brine-inclusion movements that will eventually be implemented and tested in the TOUGH-FLAC numerical THM framework.

In the next two sub-sections, we present the status of THM constitutive models for natural and crush salt, which are critical for the prediction of damage and long-term sealing and healing of the salt rock when exposed to high temperatures.

3.2 Salt Constitutive THM Models in TOUGH-FLAC

In this section, we summarize a constitutive model that have been implemented into FLAC^{3D} code and used for modeling salt coupled processes with TOUGH-FLAC. The *Lux/Wolters* constitutive model is the main model applied in TOUGH-FLAC, whereas an alternative FLAC^{3D} WIPP reference model is also available. Moreover, a modified Crushed salt WIPP model (CWIPP) model is available in TOUGH-FLAC for modeling of crushed salt backfill.

3.2.1 Lux/Wolters Constitutive THM Model for Rock Salt

The behavior of the natural salt is modeled in TOUGH-FLAC using the *Lux/Wolters* constitutive model, developed at TUC. This model has been under development and improvement since the 1980s (Hou, 2003; Hou and Lux, 2000, 1999, 1998; Hou et al. 1998; Lux, 1984; Wolters et al., 2012). Based on continuum damage mechanics, it has been established using a series of laboratory tests designed to study, from a macroscopic viewpoint, the mechanisms involved in the short- and long-term responses of rock salt. This model was validated against field- and laboratory-scale data (Hou, 2003) and implemented as a plug-in (user-defined model) in FLAC^{3D}. Most recently, a new methodology was developed to improve the modeling, spanning the range of moderate to intense salt mechanical deformation processes (Lux et al., 2018). The development of such a model relies on new laboratory strategy with three carefully designed components: (1) the development of damage is first investigated based on triaxial short-term tests with varied minimal stresses and different deformation rates; (2) long-term tests for a supplementary purpose to verify the transferability of the physical modeling approach to other stress states with lower strain rates relevant to situ deformation rates; and (3) long-term tests to increase the precision of derived material parameters determined in the short-term tests in terms of damage threshold and damage development.

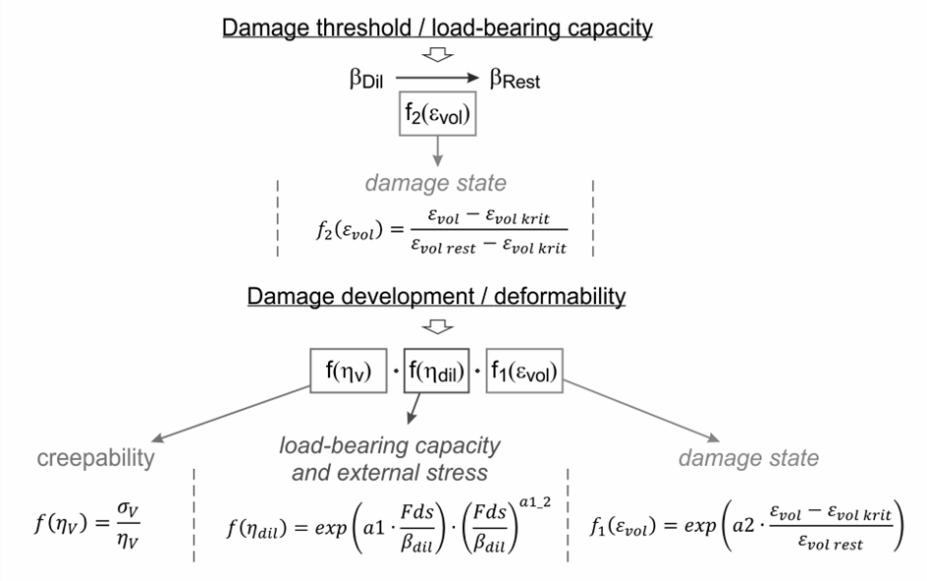

Figure 3-4. Structure of the new damage model (Lux et al., 2018)

As described by Lux et al. (2018), the basic structure of the newly formulated material approach includes three main variables and functional dependencies of the damage on each of the main influencing variables. Those are shown in Figure 3-4. As shown clearly in Figure 3-4, the three influencing variables are: η_V, denoting the current total viscosity of the material and defining creepability of the material corresponding

to the actual external stresses and the loading history; η_{dil}, denoting the actual loading factor related to the damage boundary and defining the actual load-bearing capacity of material based on the external stresses on the material and its degree of damage; and ε_{vol}, denoting damage-induced dilatancy and defining the material's damage.

Correspondingly, four basic phases are defined in the new damage approach (Figure 3-5): (I) damage-free creep phase, (II) damage initiated phase once after the damage threshold $\beta_{dil}$is exceeded, (III) damage acceleration phase once when the critical dilatancy value $\varepsilon_{vol,crit}$ is reached, and (IV) creep at the residual strength once the residual strength threshold is reached.

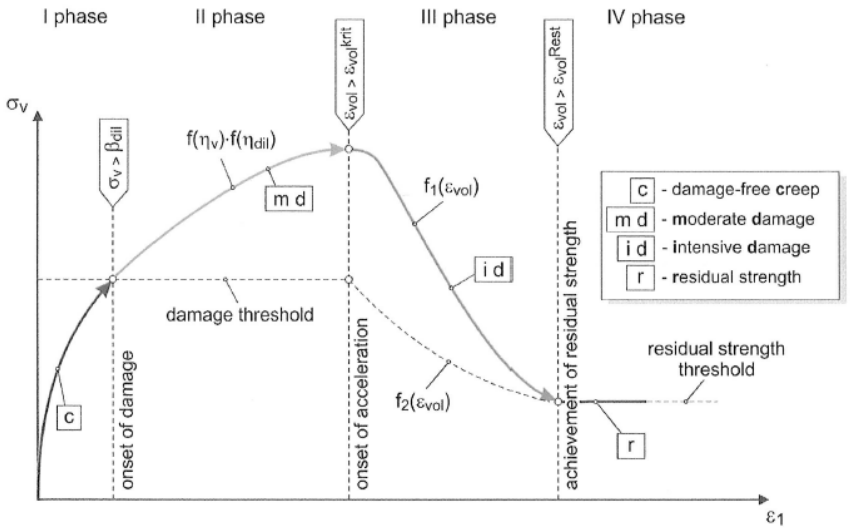

Figure 3-5. Schematic of a four-phase stress-strain relationship representing a new damage approach (Lux et al., 2018)

In brief, the *Lux/Wolters* model integrates the effects of a range of different deformation mechanisms (diffusion, dislocation, consolidation, strain hardening, fabric damage, and healing). It is assumed that different creep rates resulting from different deformation mechanisms are combined by superposition, yielding an overall strain rate tensor, $\dot{\varepsilon}_{ij}$ [s^{-1}], given by

$$\dot{\varepsilon}_{ij} = \dot{\varepsilon}^{e}_{ij} + \dot{\varepsilon}^{ie}_{ij} = \dot{\varepsilon}^{e}_{ij} + \dot{\varepsilon}^{vp}_{ij} + \dot{\varepsilon}^{d}_{ij} + \dot{\varepsilon}^{h}_{ij} \tag{3.5}$$

where $\dot{\varepsilon}^{e}_{ij}$ is the elastic strain rate tensor, $\dot{\varepsilon}^{ie}_{ij}$ is the inelastic strain rate tensor, $\dot{\varepsilon}^{vp}_{ij}$ is the viscoplastic (i.e., transient and stationary) strain rate tensor, $\dot{\varepsilon}^{d}_{ij}$ is the thermomechanically-induced damage strain rate tensor, and $\dot{\varepsilon}^{h}_{ij}$ is the thermomechanically-induced damage reduction (i.e., healing) strain rate tensor. All the components of the strain rate tensor in Equation (3.5) are expressed in [s^{-1}], and take into account a damage-induced reduction of the load-bearing cross-sectional area, according to a previous study (Kachanov, 1986). (This way, the load-bearing cross-sectional area is the original area multiplied by 1-*D*, where *D* [-] is a damage parameter.) A current description of the constitutive model *Lux/Wolters* is given in Blanco-Martín et al. (2016), including the influence of temperature on the rock salt creep deformation, and also damage/dilatancy processes, healing/sealing, and yield and potential functions of constitutive terms.

The elastic strain rate tensor, $\dot{\varepsilon}^{ie}_{ij}$, is described by Hooke's constitutive model, whereas viscoplastic strain rate tensor, $\dot{\varepsilon}^{vp}_{ij}$, is described by a modified version of the constitutive model *Lubby2* (Lux, 1984), including the damage-induced reduction of the load-bearing cross-sectional area, by means of the damage parameter *D* [-].

Within the *Lux/Wolters* model, the damage process involves the creation of micro-fissures in the rock salt material accompanied by an increase of its volume (i.e., dilatancy). The damage process can be induced by stress states exceeding the dilatancy boundary, or by fluid pressure exceeding the minimum principal stress. If the dilatancy boundary is exceeded, an additional damage-induced strain rate tensor, $\dot{\varepsilon}_{ij}^{d}$, occurs. However, the damage of rock salt may be sealed or even healed if the stress state falls below the sealing/healing threshold.

The thermomechanically-induced creation of micro-fissures is accompanied by the generation of secondary permeability (e.g., permeability associated with damage or fractures). Finally, if the fluid pressure exceeds the minimum compressive principal stress, a hydraulically-induced damage process starts. This process is mainly characterized by the creation of a secondary permeability due to the opening of originally closed grain boundaries, resulting in a flow of the fluid through these open grain boundaries. Therefore, this process is also called pressure-driven fluid infiltration.

The physical modeling and numerical simulation of sealing/healing processes need the consideration of micro-fissure orientation resulting from the stress state evolution, in which only stresses perpendicular to the micro-fissures may cause closing micro-fissures. The closure of micro-fissures is modeled with an additional sealing/healing-induced strain rate tensor, $\dot{\varepsilon}_{ij}^{h}$, and the damage parameter D is reduced. According to laboratory observations, in the *Lux/Wolters* model, the recovery of damage is faster at the beginning of the healing process (due to a rapid volume contraction), while in a second stage, slower mechanisms such as re-crystallisation or diffusion dominate (Hou, 2003).

The current implementation of the *Lux/Wolters* model includes a damage dependence of the Biot coefficient. In the undisturbed state, the Biot coefficient of rock salt is very close to zero (Hou, 2003), but increases as damage takes place. From the interpretation of laboratory-scale results, the Biot coefficient is described by

$$\alpha_{salt} = \max\left(\frac{D}{D_{\alpha}},\ 1-\exp\left(\frac{\sigma_v m D}{D-D_{\alpha}}\right)\right) \tag{3.6}$$

where D [-] is a damage parameter, D_{α}=0.1 [-] is a constant, σ_v [MPa] is von Mises equivalent stress, and m<0 [MPa^{-1}] is a parameter that enhances Maxwell viscosity (Wolters et al. 2012). Note that during healing, the initial value of the Biot coefficient can be recovered.

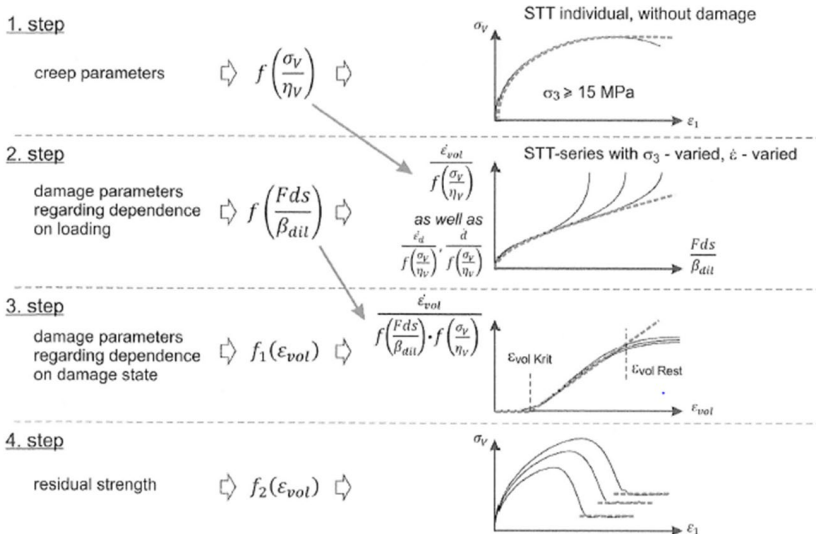

Figure 3-6. Illustration of the definition of parameters corresponding to four phases of stress-strain relationship (modified from Lux et al., 2018)

In total, the *Lux/Wolters* constitutive model includes 34 parameters needed to describe a salt deformation under stress. However, the number of parameters used in simulations may be reduced depending on phenomena under investigation. As a large number of parameters are involved, determination of these parameters is critical. As shown in Figure 3-6, the parameters are determined in four coordinated steps. Each step involves isolated depiction of the relevant functional dependencies, and parameters determined in the previous steps are further incorporated in the current steps until all the parameters are defined (Lux et al., 2018).

3.2.2 WIPP Constitutive TM Model for Rock Salt

We include a description here on the empirical WIPP reference model, because it serves in this work as an alternative or complement to the more complex *Lux/Wolters* model, especially for application to the WIPP site. It should be noted that the WIPP reference model implemented in FLAC^{3D} is different from the more advanced and complex Multimechanism Deformation (M-D) model (Munson and Dawson, 1984) that have been extensively applied for the analysis of WIPP room closure (Munson, 1997). The empirical WIPP reference model implemented in FLAC^{3D} is based on the creep model described by Hermann et al. (1980a, b) and differently expressed by Senseny (1985).

Conventionally, the volumetric stress is assumed to be very elastic, whereas for the deviatoric part, the creep strain rate is given by

$$\dot{\varepsilon}_{ij}^{c} = \dot{e}_{ij}^{c} = \frac{3}{2}\frac{s_{ij}}{\sigma_v}\dot{\varepsilon} \tag{3.7}$$

The scalar strain rate $\dot{\varepsilon}$ is composed of a primary and a secondary creep rate, which read respectively

$$\dot{\varepsilon}_p = \begin{cases} (A - B\varepsilon_p)\dot{\varepsilon}_s & \dot{\varepsilon}_s \geq \dot{\varepsilon}_{ss} \\ [A - B(\dot{\varepsilon}_{ss}/\dot{\varepsilon}_s)\varepsilon_p]\dot{\varepsilon}_s & \dot{\varepsilon}_s < \dot{\varepsilon}_{ss} \end{cases} \tag{3.8}$$

and

$$\dot{\varepsilon}_s = D\sigma_v^n exp(-Q/RT) \tag{3.9}$$

where R is the universal gas constant, T is temperature, and Q is the activation energy. The mean primary creep strain is calculated in the iterations using

$$\varepsilon_p = \varepsilon_p^{old} + \dot{\varepsilon}_p \Delta t/2 \tag{3.10}$$

The material properties required by the WIPP model are K, G, A, B, $\dot{\varepsilon}_{ss}$, D, n and Q.

Finally, the WIPP model is combined with the Drucker-Prager criterion (shear and tensile yielding) in the WIPP-Creep Viscoplastic Model implemented in FLAC^{3D}. Again, the volumetric response in this case is elastoplastic. In addition, softening behavior is included using the second invariant of the deviatoric plastic strain increments:

$$\varepsilon^{dp} = \varepsilon^{dp} + \Delta t\sqrt{\dot{\varepsilon}_{ij}^{dp}\dot{\varepsilon}_{ij}^{dp}/2} \tag{3.11}$$

One appealing feature with the WIPP-creep viscoplastic model implemented in FLAC^{3D} is it requires only 8 parameters, which is much less that the number of parameters required for the M-D and Lux/Wolters models. It is attractive for evaluating temperature dependent creep closure, whereas it does not include features for dilatant induced porosity and permeability changes needed for modeling brine-migration.

3.2.3 Modified CWIPP Constitutive TM Model for Crushed Salt

The *cwipp* model available in FLAC^{3D} to model the reconsolidation process of granular salt is based on previous studies on crushed salt compaction (Callahan and DeVries, 1991; Sjaardema and Krieg, 1987) and on the *wipp* model for natural salt, also implemented in FLAC^{3D} (Itasca, 2011).

The main characteristic of the *cwipp* model is that it allows for modeling volumetric strain changes associated with creep processes (classically, viscoplasticity occurs at a constant volume). The total strain rate tensor, $\dot{\varepsilon}_{ij}$, comprises a nonlinear elastic component, a viscous compaction component and a viscous shear contribution. The latter is adapted from the *wipp* model and is purely deviatoric. The total strain rate tensor reads

$$\dot{\varepsilon}_{ij} = \dot{\varepsilon}_{ij}^{e} + \dot{\varepsilon}_{ij}^{vc} + \dot{\varepsilon}_{ij}^{vs} \tag{3.12}$$

where superscripts *e*, *vc* and *vs* stand for elastic, viscous compaction, and viscous shear, respectively. As reconsolidation occurs, density increases towards that of the natural salt. In the *cwipp* model, density is a monotonically increasing with the compaction density rate derived from experimental results (Callahan and DeVries, 1991; Sjaardema and Krieg, 1987). The viscous compaction term in the model accounts for the density evolution during compaction. This term is only active if the mean effective stress is compressive and if the monotonic density has not yet reached the intact salt density (i.e., there is no further compaction beyond the intact salt density). During compaction, the elastic properties (shear, *G,* and bulk, *K,* moduli) increase as the density increases according to a nonlinear empirical expression given by

$$a = a_{salt} \exp\left(a_1 \left[\rho - \rho_{salt}\right]\right) \tag{3.13}$$

where $a=\{K,G\}$. Variables ρ and ρ_{salt} stand for the drained densities of the crushed salt and the natural salt, respectively. Parameter a_1 [kg^{-1}m^3] is obtained from the condition that the moduli take their initial value at the initial value of density. When $\rho=\rho_{salt}$, the elastic moduli are those of the natural salt, $K=K_{salt}$ and $G=G_{salt}$. In total, the *cwipp* model is characterized by 17 parameters.

We have made some important improvement of the *cwipp* model for the purpose of simulations of crushed salt. Indeed, in the original *cwipp* model, density is constant, and therefore cannot increase even if the mean compressive stress increases. To avoid this limitation, we developed a modified version in which density honors the volumetric strain evolution, but keeping other features of the original *cwipp* model.

As the bulk modulus increases toward that of the intact salt, the Biot coefficient decreases from almost 1 to that of the host rock; therefore, the poromechanical effects within the backfill will be stronger before substantial compaction occurs. The Biot coefficient is calculated using

$$\alpha_{crushed\ salt} = 1 - \frac{K}{K_s} \tag{3.14}$$

where K is the drained bulk modulus, and K_s is the bulk modulus of the solid material.

It is important to highlight that the long-term mechanical responses predicted by the *cwipp* and the *Lux/Wolters* models are similar: due to the creep over time, stresses tend toward the isotropic state, and therefore the deviatoric components of both models tend to zero. For the crushed salt, the compaction component vanishes after full reconsolidation, and for the natural salt, damage and healing counteract each other. Consequently, only the elastic components prevail. Given that after reconsolidation the elastic moduli of the crushed salt are assumed be equal to those of the natural salt, the modeled long-term response of the two materials is similar.

A shortcoming of the current crushed salt constitutive model is that it does not consider the effects of temperature and saturation on the compaction rate. Temperature and saturation dependency should be included once additional data on temperature and saturation effects on the crushed salt compaction are available from laboratory or field tests.

3.3 Status TOUGH-FLAC verification and validation

The coupled THMC processes in salt are complex, but can be analyzed using coupled numerical modeling with adequate constitutive models, verified and validated against laboratory and field tests. Such validation is also important for uncertainty reduction related to long-term model predictions. Below we list completed verifications and validations of TOUGH-FLAC related to salt coupled processes and references were those activities are documented.

- Brine infiltration laboratory experiments validating implementation of *Lux/Wolters* model in TOUGH-FLAC for brine infiltration (Rutqvist et al., 2012; Blanco-Martín et al., 2015a)
- Triaxial compression test to validate TOUGH-FLAC with *Lux/Wolters* model regarding mechanical behavior under shear stress and strain (Rutqvist et al., 2013)
- Modeling of Terzaghi's 1-D consolidation problem, Mandel's poroelastic problem, and Booker and Savvidou's thermos-poroelastic problem with comparison to analytic solution to verify TOUGH-FLAC hydraulic and mechanical sequential coupling algorithm (Rutqvist et al., 2016; Blanco-Martín et al., 2017)
- Modeling TSDE experiment validating THM model including drift closure and crushed salt compaction at a realistic scale (Rutqvist et al., 2015; Blanco-Martín et al., 2016)
- Modeling WIPP Room A1 THM-induced brine-migration experiment (Rutqvist et al., 2016; Blanco-Martín et al., 2018)
- Modeling salt dissolution/precipitation laboratory experiment under thermal gradient (Rutqvist et al., 2015; Blanco-Martín et al., 2018)
- Code-to-code verification between TOUGH-FLAC and FLAC-TOUGH for various benchmark examples, including long-term repository behavior and TSDE experiment (Blanco-Martín et al., 2015b; 2016). Recall that TUC's FLAC-TOUGH simulator is based the same basic codes (TOUGH2 and FLAC^{3D}), but the numerical schemes for linking the two codes are different from that in TOUGH-FLAC.

In addition, LBNL is currently involved in a newly started international code-comparison project called BenVaSim, which is led by TUC (Rutenberg et al., 2018). The description of the BenVaSim project and our current progress as a modeling partner in this international collaborative project are presented in Section 5 of this report. We would also like to emphasize that there are numerous validations of the *Lux/Wolters* constitutive model conducted at TUC, the *cwipp* crushed salt model documented in FLAC^{3D} manual (Itasca, 2011), as well as numerous verifications and validations of the respective codes TOUGH2 (Pruess et al., 2012) and FLAC^{3D} (Itasca, 2011). Such extensive testing over a wide range of applications and conditions provides further confidence in the application of the TOUGH-FLAC simulator for simulations of salt coupled THMC processes.

This page is intentionally left blank.

4. DUAL-CONTINUUM MODEL FOR BRINE MIGRATION IN SALT

4.1 Short overview of dual-continuum models

The general form of basic equations describing transient processes, such as advection, diffusion, and heat conduction, driven by external sources, in heterogeneous media can be given by

$$\alpha \frac{\partial u_1}{\partial t} + \beta \frac{\partial u_2}{\partial t} = f(u_1) + g(u_2) \tag{4.1}$$

where u_1 and u_2 are the field variables, α and β are coefficients, and $f(u_1)$ and $g(u_2)$ are different functions. Equation (4.1) can represent the mass balance, energy balance, etc.

When the flow and transport processes in different material domains are governed by the same law and can be averaged through a certain domain volume, Equation (4.1) can be simplified as:

$$\gamma \frac{\partial \bar{u}}{\partial t} = h(\bar{u}) \tag{4.2}$$

where γ, $\bar{u}$ and $h(\bar{u})$ are averaged values corresponding to the terms of Equation (4.1). Equation (4.2) represents an equivalent continuum model schematically shown in Figure 4-1a.

The dual-continuum concept is commonly used to represent media with different material domains. There are two types of the dual-continuum models: the dual-porosity model, and the dual-permeability model.

The dual-porosity model is based on the assumption that both of the media components are porous and characterized by different porosity values, but one of the components is characterized by low permeability. In this case, Equation (4.1) can be converted into a system of two equations given by:

$$\begin{cases} \alpha \frac{\partial u_1}{\partial t} + \beta \frac{\partial u_2}{\partial t} = g(u_2) \\ \alpha \frac{\partial u_1}{\partial t} = L(u_1, u_2) \end{cases} \tag{4.3}$$

where $L(u_1, u_2)$ represents a simplified coupling term. A schematic representation of the dual-porosity model is given in Figure 4-1b.

The dual-continuum model to describe flow and transport in heterogeneous media is based on the assumption that flow and transport occur in both continua, and Equation (4.1) can be converted to a system of two equations given by:

$$\begin{cases} \alpha \frac{\partial u_1}{\partial t} = f(u_1) + C(u_1, u_2) \\ \beta \frac{\partial u_2}{\partial t} = g(u_2) - C(u_1, u_2) \end{cases} \tag{4.4}$$

where $C(u_1, u_2)$ is the coupling term used to describe the interaction between the two continua. A schematic representation of the dual-continuum model is given in Figure 4-1c.

The idea of solving Equation (4.1) to Equation (4.4) is similar to sequential coupling scheme for analyzing coupled hydro-mechanical processes in porous media. When the coupling between the two media is very strong, the coupling term $C(u_1, u_2)$ should be carefully derived, which is to obtain accurate and stabile numerical solutions. Birkholzer and Rouvé (1994) discussed and compared existing dual-continuum approaches and provided a detailed derivation of the coupling term based on a solid physical explanation of transport problems.

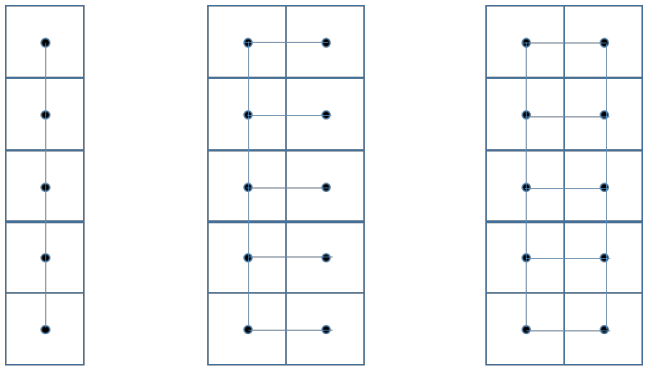

Figure 4-1. Schematic of 1-D models: (a) single continuum, (b) dual-porosity, and (c) dual-permeability (Doughty, 1999).

To improve the accuracy of simulations, in the case of high flow and transport gradients in one of the two continua, the application of the fine mesh discretization of the entire domain is needed. A series of increased-order models were developed to address such a problem. Figure 4-2 illustrates several types of increased-order models.

Figure 4-2a shows the MINC model used in TOUGH2 (Pruess et al., 2012), where the rock matrix continuum is discretized into several grids. These grids share the same center, and the interaction with each other can be simplified into several 1-D models of flux exchange in different directions. Such a model was shown to be very effective in comparison with the original first-order TOUGH2. Figure 4-2b shows another model named explicit discretization method (EDM) proposed by Wu and Pruess (1988). EDM is computationally more expensive due to the explicit equidimensional discretization requiring finer mesh compared with MINC. Moreover, the conformity between the rock matrix and fractures is problematic. As reported by Wu and Pruess (1988), compared with EDM, MINC gives more accurate solution for water imbibition. Figure 4-2c shows another formulation of immobile continuum regions (such as rock matrix) consisting of N blocks connected to each mobile continuum region (such as a fracture). This formulation is named multi-rate mass transfer (MRMT) as described by Silva et al. (2009). The fundamental equation of the immobile blocks is represented by the second equation in Equation (4.3), with $L(u_m, u_{im,j}) = \alpha_j(u_m - u_{im,j})$, representing the interaction among the mobile and the jth immobile block. Using the analytical solution for $u_{im,j}$, u_m can be numerically determined. Such a scheme does not explicitly refine the mesh in immobile blocks; instead, the application of several immobile regions enhances the approximation order by producing a piecewise-linear approximation. Using this approach, non-linear, high-gradient problems can be solved.

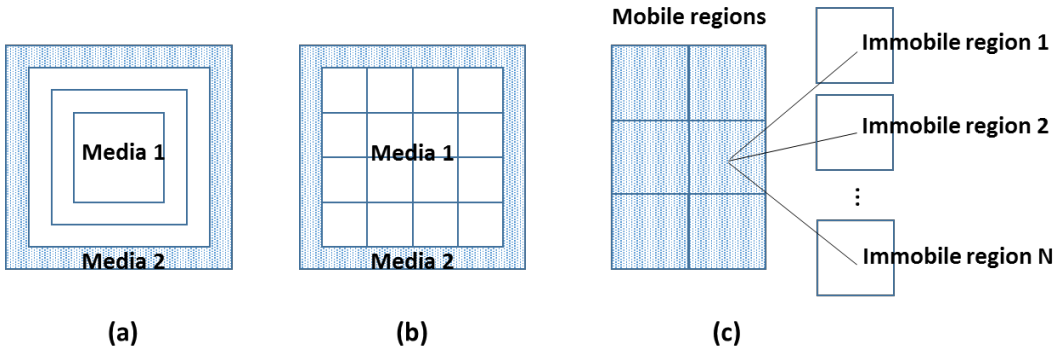

Figure 4-2. Schematic illustrations of dual-continuum-concept-based increased-order models.

Taking into account the advantages of numerical simulations using a dual-continuum model, we developed a dual-continuum model for simulations of brine migration in salt.

4.2 Conceptual model and simplification

For porous water and brine migration in salt grains, we assume two types of continua: the interconnected pores as the primary continuum, and the salt grains as the secondary continuum. In the entire dual-continuum system, two components are considered—salt and water. The salt could be dissolved in water or be present in solid phase, and be affected by dissolution and precipitation processes. Water could be present in liquid or gaseous phases, and be affected by vaporization or condensation. These two components exist in the two continua. The schematic of the dual-continuum model is shown as Figure 4-3.

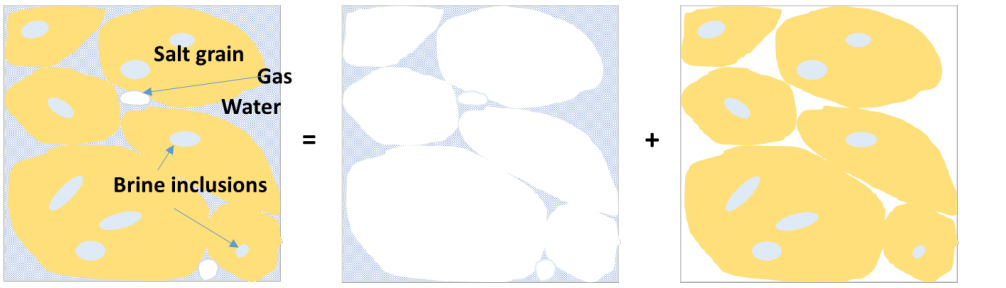

Components	In primary continuum	In secondary continuum
Salt	Salt (solid or dissolved)	Salt (solid or dissolved)
Water	Water (liquid and gas)	Water (liquid)

Figure 4-3. Schematic of the dual-continuum model for salt migration

The following simplifications and assumptions are made for the application of the dual-continuum model: (1) Water vapor is the only component in the gaseous phase. There may be a small amount of dry air and dissolved air contained in the pores, but the specific components may slightly differ from case to case. Therefore, to simplify the model, in this study, we consider only the water vapor, without additional gas components.

(2) Salt grains contain no gas. In rare cases, when brine inclusions contain gaseous bubbles, water evaporates at the hot side of these bubbles, migrates down to the cold side and condenses. Assuming that brine inclusions do not significantly affect brine migration, we assume no gas in the salt grains.

4.3 Dual-Continuum Model for Brine Migration

4.3.1 Governing Equations

The constitutive laws considered in the new dual-continuum model for brine migration are listed in Table 4-1.

Table 4-1. Constitutive laws used in the dual-continuum model.

Components	Primary continuum	Secondary continuum	Coupling
Salt	Darcy`s law Fick`s law	Brine migration law	Brine migration-related salt migration flux as a sink/source
Water	Darcy`s law Fick`s law	Brine migration law	Brine migration flux as a sink/source

The mass balance of the salt in interconnected pores is expressed as:

$$\frac{\partial(X_l^s \rho_l S_l \varphi)}{\partial \mathrm{t}} = \nabla \cdot (X_l^s \mathbf{q}_l + \mathbf{F}_l^s) + Q_{migration}^s + q_{source}^s \tag{4.5}$$

where X_l^s is the mass fraction of salt in the liquid in pores, ρ_l is the density of the liquid in pores, S_l is the liquid saturation, φ is the porosity, $Q_{migration}^s$ is the brine-migration induced salt source in pores (which will be presented later), and q_{source}^s is the salt source in pores. Darcy`s law for advective flux, and Fick`s law for diffusive flux are given by

$$\mathbf{q}_l = -\rho_l \frac{k k_{rl}}{\mu_l} (\nabla \mathrm{P}_l - \rho_l \mathbf{g}) \tag{4.6}$$

$$\mathbf{F}_l^s = -\varphi \tau_0 \tau_l \rho_l d_l^s \nabla X_l^s \tag{4.7}$$

where k is the absolute permeability of liquid, k_{rl} is the relative permeability, μ_l is the viscosity, P_l is the liquid fluid pressure, $\mathbf{g}$ is the gravitational acceleration, $\tau_0 \tau_l$ represents the tortuosity of the liquid, and d_l^s is the molecular diffusion coefficient of salt in the liquid.

The mass balance of the salt in salt grains is expressed as:

$$\frac{\partial[(1-\varphi) X_s^s \rho_s]}{\partial \mathrm{t}} = \mathrm{F}_{migration}^s - Q_{migration}^s \tag{4.8}$$

where $\mathrm{F}_{migration}^s$ represents the salt content in the flux of brine, which will be discussed later.

The mass balance of water in interconnected pores is expressed as:

$$\frac{\partial(X_l^w \rho_l S_l \varphi + X_g^w \rho_g S_g \varphi)}{\partial \mathrm{t}} = \nabla \cdot \left(X_l^w \mathbf{q}_l + \mathbf{q}_g + \mathbf{F}_l^w + \mathbf{F}_g^w\right) + Q_{migration}^w + q_{source}^w \tag{4.9}$$

where X_l^w is the mass fraction of water in the liquid, X_g^w is the mass fraction of water in the gas, ρ_g is the gas density, S_g is the gas saturation, $Q_{migration}^w$ is the brine-migration induced water source in the pores (which will be introduced later), and q_{source}^w is the water source in the pores. Darcy`s law for advective flux in gas and Fick`s law for diffusive flux in liquid and gaseous water are given by

$$\mathbf{q}_g = -\rho_g \frac{k k_{rg}}{\mu_g} \left(\nabla \mathrm{P}_g - \rho_g \mathbf{g}\right) \tag{4.10}$$

$$\mathbf{F}_l^w = -\varphi \tau_0 \tau_l \rho_l d_l^w \nabla X_l^w \tag{4.11}$$

$$\mathbf{F}_g^w = -\varphi \tau_0 \tau_g \rho_g d_g^w \nabla X_g^w \tag{4.12}$$

where k is the intrinsic permeability, k_{rg} is the gas relative permeability, μ_g is the viscosity of gas, P_g is the gas pressure, and d_l^w and d_g^w are the molecular diffusion coefficients of water in the liquid and gaseous phase, respectively.

The mass balance of water in the salt grains is:

$$\frac{\partial[(1-\varphi)X_s^w\rho_s]}{\partial t} = F_{migration}^w - Q_{migration}^w \tag{4.13}$$

where $F_{migration}^w$ represents the water content in the flux of brine migration, which will be discussed later.

To satisfy the above equations, the following relationships should hold:

$$P_l = P_g + P_{capillary} \tag{4.14}$$

$$S_l + S_g = 1 \tag{4.15}$$

$$X_g^w = 1 \tag{4.16}$$

$$X_l^s + X_l^w = 1 \tag{4.17}$$

$$X_s^s + X_s^w = 1 \tag{4.18}$$

The energy balance in the entire system is:

$$\frac{\partial[(1-\varphi)\rho_s C_s T+\rho_g S_g \varphi u_g+\rho_l S_l \varphi u_l]}{\partial t} = \nabla\cdot\mathbf{H} + f_{heat} \tag{4.19}$$

where u_g and u_l are the specific internal energy in gas and liquid, f_{heat} is the heat source, and

$$\mathbf{H} = -\lambda\nabla T + h_l\mathbf{q}_l + h_g\mathbf{q}_g \tag{4.20}$$

where λ is the thermal conductivity, h_l and h_g are the specific enthalpy in liquid and gas, respectively.

The above equations represent a system of governing equations describing coupled fluid flow and heat transfer processes in the dual-continuum system.

4.3.2 Implicit Approach for Modeling of Brine Migration

To explicitly simulate the thermal gradient induced brine migration, we need to consider dissolution/precipitation induced by the temperature gradient. To represent dissolution/precipitation, additional source/sink terms need to be introduced into the model:

$$F_{migration} = (1-\varphi)\rho_s R_P f(X - X_{equilibrium}) \tag{4.21}$$

where R_P is the reaction rate, $f(X - X_{equilibrium})$ is the function of mass fraction relevant to the equilibrium mass fraction. However, after trying several functions including linear, exponential and logarithmic, we find that the results are dependent on the choice of reaction rate. Therefore, explicit modeling of reactive transport requires a model to accurately represent the reaction rate.

Alternatively, according to Anthony and Cline (1971), brine migration induced by thermal gradient could be implicitly reflected by the flux as a function of the thermal gradient. Ratigan (1984) and Olivella et al. (1994) used this concept to express the migration velocity $\mathbf{v}_{migration}$ and migration-induced sink/source $q_{migration}$ as follows:

$$\mathbf{v}_{migration} = -\rho_s\sigma(1-\varphi)D\nabla T \tag{4.22}$$

$$q_{migration} = \frac{|\mathbf{v}_{migration}|}{d} \tag{4.23}$$

where ρ_s is the density of the salt, σ is the soret coefficient ($℃^{-1}$), D is the diffusivity of the brine, d is the ratio of the crystal volume to the crystal surface area.

The following functions for Equations (4.5)- (4.13) are defined:

$$Q^s_{migration} = X^s_s q_{migration} \tag{4.24}$$

$$Q^w_{migration} = X^w_s q_{migration} \tag{4.25}$$

$$\mathrm{F}^s_{migration} = \nabla \cdot (X^s_s \mathbf{v}_{migration}) \tag{4.26}$$

$$\mathrm{F}^w_{migration} = \nabla \cdot (X^w_s \mathbf{v}_{migration}) \tag{4.27}$$

4.4 Extended Finite Volume Method for Mechanical Analysis

The finite volume method (FVM) is a widely used for numerical simulations of multiphase, multicomponent flow and heat transfer, and is implemented in the TOUGH family codes (Pruess et al., 2012; Jung et al., 2017). The finite element method (FEM) projects differential equations with weighted average to integral equations on the volume. The FVM integrates the differential equations directly on the volume (and further converts to integration on area based on the divergence theorem), leading to the high accuracy of local conservation. However, the application of the traditional FVM is limited when dealing with anisotropic problems, such as mechanical problems with over one dimension. This limitation could be explained from the perspective of partition of unity, the interpolation field that the traditional FVM constructs is piecewise linear in each direction. As shown in Figure 4-4, in FVM, the weight function is linear in each direction with a constant patch function.

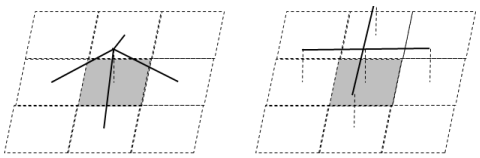

Figure 4-4. Schematic illustration of the traditional finite volume approximation: (a) weight function, and (b) patch function.

In order to address this fundamental problem, in this study an extended finite volume method (XFVM) is proposed to perform a fully coupled THM analysis.

To achieve higher approximation in the entire space, a straightforward approach is to introduce an overlap in each direction, as shown in Figure 4-5a. Therefore, for an *n*-dimensional problem, *n*-dimensional partition of unity can be constructed. However, for cells of arbitrary shape, such as those generated by the Voronoi tessellation, overlapping cells with different number of edges makes conformability and completeness of the approximation unrealistic, unless a rectangle-based cell system is used. For high flexibility, we developed alternative formulations for higher-order approximation, which could be used for regular Voronoi tessellated mesh including rectangles, as shown in Figures 4-5(b-d).

For a randomly tessellated Voronoi mesh as shown in Figure 4-5b, each triangle (in dashed lines) is the basis for interpolation fields, while the edges of the Voronoi cell are integration boundaries (edges in 2-D, in solid lines). In each triangle, the variables at the vertices (i.e., the centers of different Voronoi cells) could be constants, linear, or *n*-th order. Thereby, linear, second-order or (*n*+1)th-order approximation can be achieved.

If rectangular grids (solid lines in Figure 4-5) are used, there might be different ways to construct the interpolation triangles (dashed lines), leading to different interpolation approaches (Figures 4-5c and 4-5d). For example, Figure 4-5c illustrates the application of eight interpolation triangles for one rectangular cell, and Figure 4-5d shows the use of six interpolation triangles, which are shown by solid lines of different color. For comparison, if using constant nodal variables, the scheme shown in Figure 4-5a leads to bi-linear full-space approximation, and the schemes in Figure 4-5(b-d) lead to linear approximation.

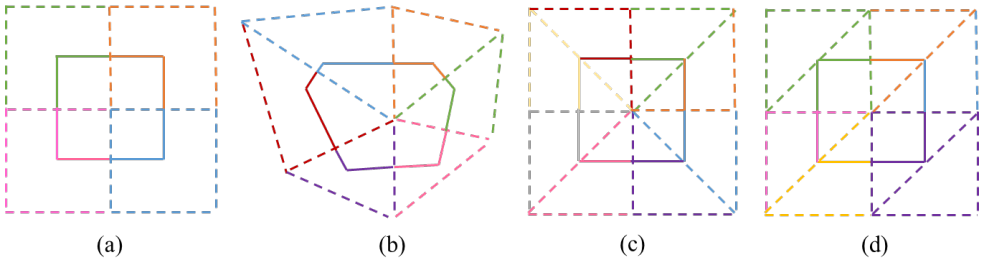

Figure 4-5. Four types of increased-order approximation.

4.5 Verification examples

To verify the model, we show some simulated results of 1-D problems and compare with available analytical solutions or simulations by TOUGH2. The conceptual schematics of the verification examples are shown in Figure 4-6.

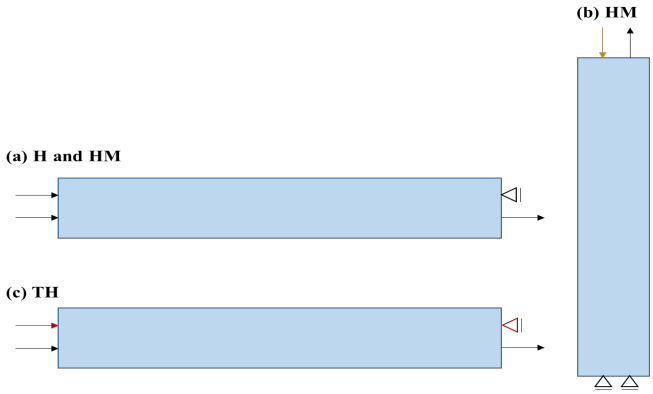

Figure 4-6. Conceptual schematics of the verification examples: model scenarios and geometry.

4.5.1 Flooding induced hydro-mechanical changes

In this example, we simulated 1-D coupled hydro-mechanical processes due to a sudden rise of the pressure at one end of the model domain (Figure 4-6a). The hydro-mechanical properties are listed in Table 4-2, and the initial and boundary conditions are listed in Table 4-3.

Table 4-2. Hydro-mechanical properties

Parameters	Symbols	Values	Units
Young's modulus *(dr.)*	E	150	MPa
Poisson's ratio	ν	0	
Porosity	ϕ	0.15	--
Intrinsic permeability	K	10^{-20}	m^2
Biot coefficient	α	1	
Liquid viscosity	η_l	10^{-9}	$MPa \cdot s$
Liquid bulk modulus	$\breve{K}_l$	2100	MPa

Table 4-3. Initial and boundary conditions

Parameters	Symbols	Values	Units
Total stress	σ_{tot0}	0	MPa
Pore-water pressure	p_{l0}	0	MPa
Liquid saturation	S_{l0}	1	
Left-hand side total stress	σ_{tot}	1	MPa
Left-hand side pressure	p_l	1	MPa
Right-hand side pressure	p_l	0	MPa

First, we validated the programming C code for fluid flow (without considering mechanics) based on a comparison of the results of simulations with the analytical solution for the pressure evolution:

$$p(\mathrm{x},\mathrm{t}) = p_{left} * \left[\left(1-\frac{x}{L}\right) - \frac{2}{\pi}\sum_{n=1}^{\infty} e^{-n^2\pi^2\bar{t}}\left(\frac{sinn\pi\frac{x}{L}}{n}\right)\right] \tag{4.34}$$

Figure 4-7 demonstrates a good agreement between the numerical results and the analytical solution of Equation (4.34)

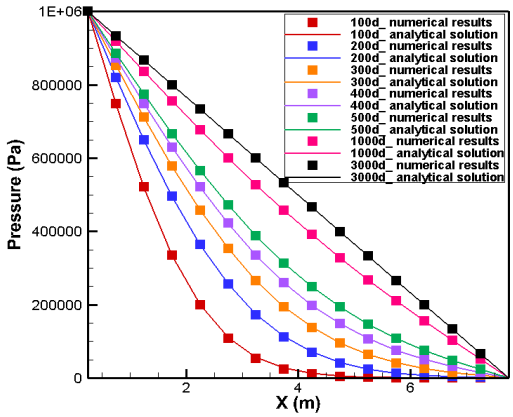

Figure 4-7. Pressure evolution without considering mechanics: numerical results compared with analytical solution. (Numbers in the legend indicate the time in days of predictions.)

Then, we validated the model and the code, which were developed for coupled hydro-mechanical modeling. We selected to use the same order models for pressure and displacement as the primary variables. The time step of 10 days was set and the simulation ran for 100,000 days. The analytical solution of this problem was provided by BenVaSim project (Rutenberg et al., 2018). Figures 4-8 and 4-9 show the calculated pressure evolution and displacement at steady state compared with the analytical solution. We find very good agreement, indicating high accuracy of our new model.

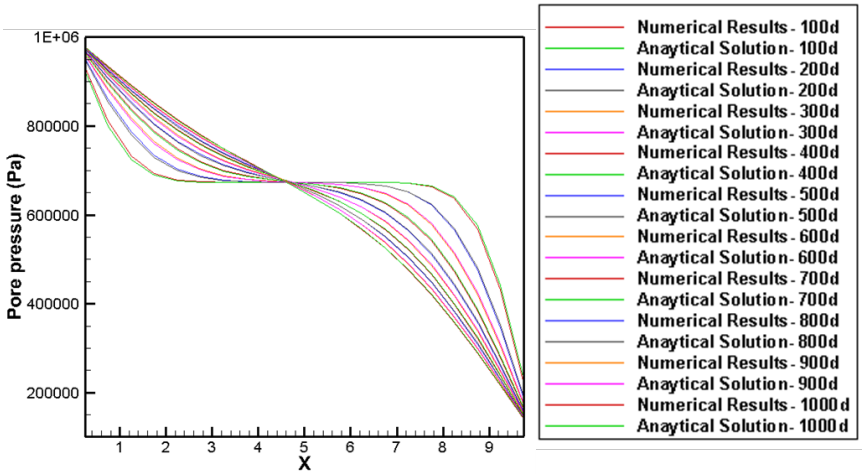

Figure 4-8. Pressure evolution considering mechanics: numerical results compared with analytical solution. (Numbers in the legend indicate the time in days of predictions.)

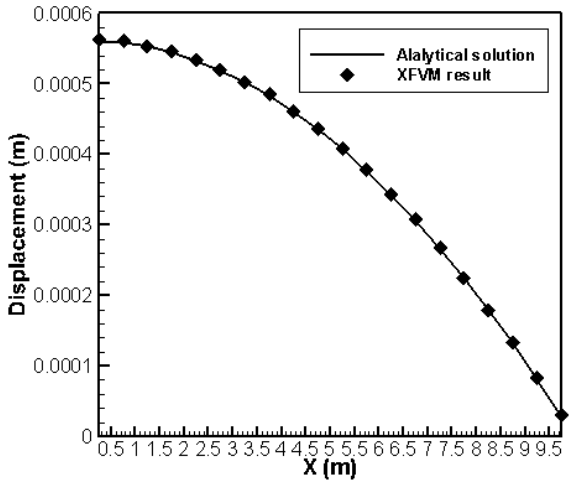

Figure 4-9. Distribution of displacement at steady state: XFVM results compared with analytical solution.

4.5.2 Pore-Volume Coupling

In order to demonstrate the accuracy of the new code for modeling coupled HM behavior of porous deformable media, we simulated as an example a 1-D poroelastic column, supporting vertical loading on the top boundary (Figure 4-6b). The column is 80 m high and 20 m wide. 200 kPa loading was evenly applied on the top boundary of the column. Table 4-4 lists the hydro-mechanical properties.

Table 4-4. Hydro-mechanical properties

Parameters	Symbols	Values	Units
Young's modulus *(dr.)*	E	3.7	MPa
Poisson's ratio	ν	0.35	
Porosity	ϕ	0.15	
Intrinsic permeability	K	$2e10^{-15}$	m^2
Biot coefficient	α	1	
Liquid viscosity	η_l	10^{-9}	$MPa \cdot s$

The time step used for the simulation was 100 days and the simulated time span was 20,000 days (≈ 55 years). The analytical solution of the settlement and the fluid pressure evolution for this problem derived by Biot (1941) is given by:

$$w_s(\mathrm{t}) = \frac{8}{\pi^2} a h_c F_0 \sum_{n=0}^{\infty} \frac{1}{(2n+1)^2} \left\{ 1 - e^{\left[-\left(\frac{(2n+1)\pi}{2h_c} \right)^2 ct \right]} \right\} \tag{4.35}$$

$$p(\mathrm{y}, \mathrm{t}) = \frac{4}{\alpha\pi} F_0 \sum_{n=0}^{\infty} \frac{1}{(2n+1)} e^{\left[-\left(\frac{(2n+1)\pi}{2h_c} \right)^2 ct \right]} sin \frac{(2n+1)\pi y}{2h_c} \tag{4.36}$$

where h_c is the height of the column, a and c are the final compressibility and consolidation constants defined by Biot (1941). We compared the calculated results of the settlement and pore pressure evolution. Figures 4-10 and 4-11 demonstrate a good agreement between the numerical results and the analytical solution.

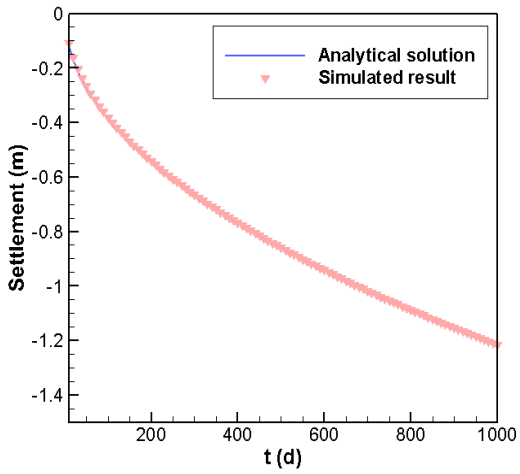

Figure 4-10. Comparison of the calculated settlement evolution with analytical solution.

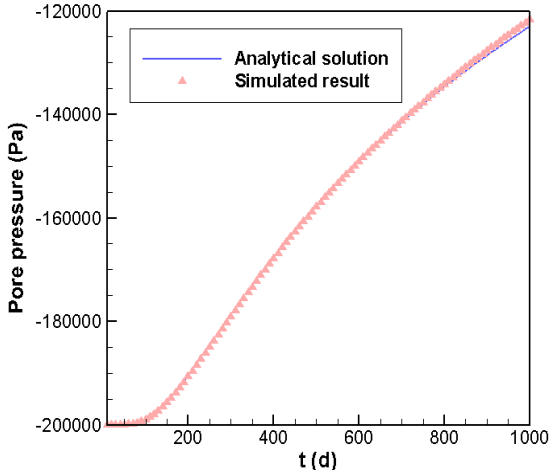

Figure 4-6. Comparison of the calculated pressure evolution with analytical solution.

4.5.3 Thermal-Hydrological (TH) simulation

In this problem, coupling between thermal and flow was simulated. At the beginning, temperature and pressure at the left side of the column were increased suddenly from 25℃ to 85℃ and from 0.1 MPa to 1 MPa, respectively (Figure 4-6c). At the right side end, the temperature and pressure were fixed to their original values of 25℃ and 0.1 MPa. Table 4-5 lists the hydro-thermal properties. Figures 4-12 and 4-13 show a good comparison of the evolution of pressure and temperature simulated using the new C code and the TOUGH2-EOS3 code.

Table 4-5. Hydro-thermal properties

Parameters	Symbols	Values	Units
Pore compressibility	Pc	$5e8$	Pa^{-1}
Porosity	ϕ	0.002	
Intrinsic permeability	K	10^{-20}	m^2
Heat conductivity	λ	1.3	W/m℃

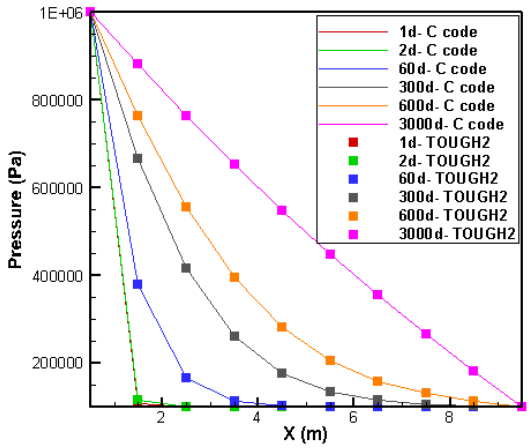

Figure 4-7. Comparison of the pressure evolution simulated using the new C-code and TOUGH2

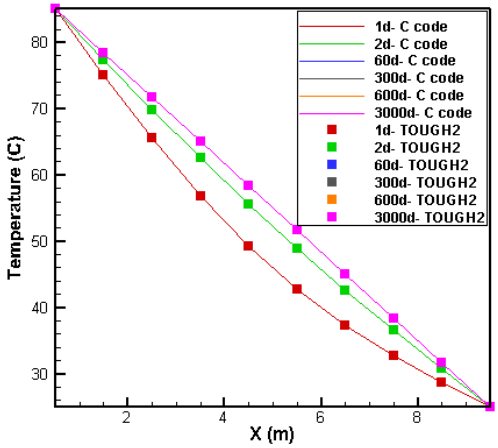

Figure 4-8. Comparison of the temperature evolution using the new C-code and TOUGH2

Simulations showed that as permeability is low and compressibility is relatively high, it takes long time for the pressure to reach steady state. By contrast, as the rock specific heat is low, the temperature reaches steady state rapidly.

4.5.4 Diffusion in the single continuum

In this example, we first set the second continuum as salt-saturated, i.e., without considering the brine inclusion. In this case, diffusion occurs only in the single interconnected pore continuum. Figure 4-14 shows the modeling domain and boundary conditions. The porosity is 0.01, the diffusion coefficient is 1e-9 m^2/s, and the pore compressibility is 1e-7 Pa^{-1}.

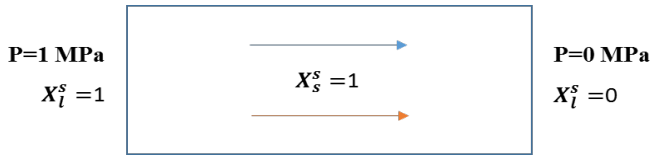

Figure 4-9. Modeling geometry and boundary conditions.

We chose the output times as 100, 200, 2000, 6000, 20,000 200,000 and 1,000,000 days. The results of simulations are shown in Figures 4-15 and 4-16 (on both figures, the legend indicate the time in days of simulations). The steady state conditions were reached in a few time steps. By contrast, it took much longer time for the salt diffusion to reach steady state in the entire domain, as shown in Figure 4-15.

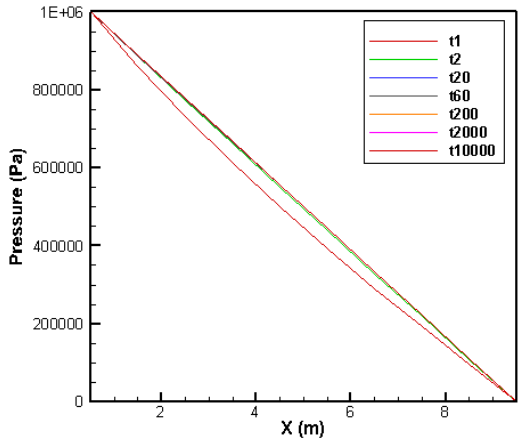

Figure 4-10. Pressure evolution

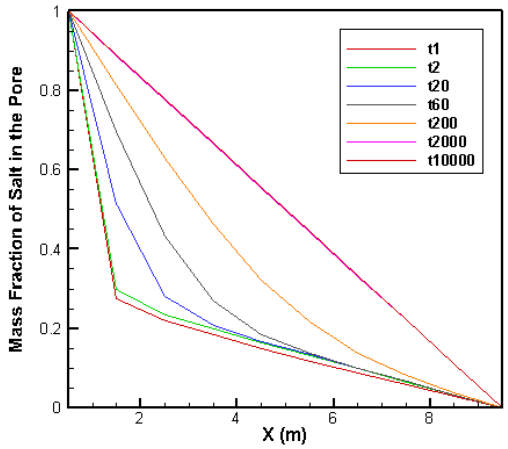

Figure 4-11. Evolution of salt mass fraction

4.5.5 Diffusion in the dual continuum

In this section, we present the results of simulation of diffusion in the salt formation, considering the dual continuum with different values of porosity. The model geometry and boundary conditions are shown in Figure 4-17. For this simulation, pore pressure is uniform and constant, therefore no advection is considered, and pore compressibility is not considered. We simulated the cases when porosity is 0.001 and 0.7. For this homogeneous domain, by using different porosity values, we can consider cases with different portions of brine flow driven by concentration difference.

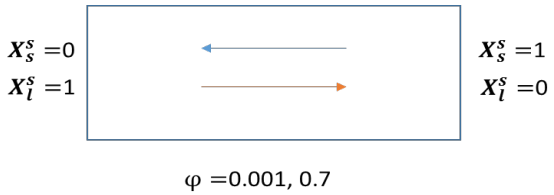

Figure 4-12. Model geometry and boundary conditions.

As pore compressibility is not considered, the transient effects for the first continuum are impacted by mass fraction change of water/salt, and by the brine migration into the interconnected pores. As shown in Figure 4-19, the porosity does not have much impact on the evolution of the diffusion in this continuum. While for the second continuum, i.e., salt grains, due to the loss of brine and its mass change, the porosity has a larger impact on the diffusion, as shown in Figure 4-20.

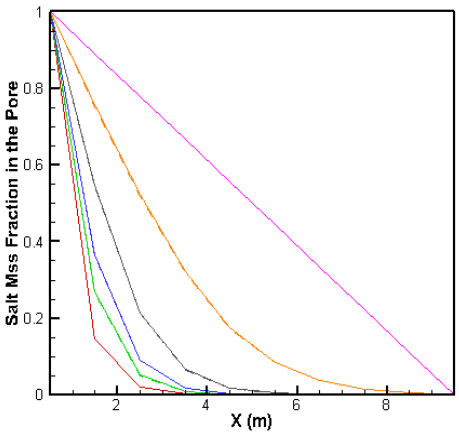

Figure 4-13. Evolution of salt mass fraction in the interconnected pores. Solid and dashed lines correspond to porosity of 0.001 and 0.7, respectively. See legend in Figure 4-16.

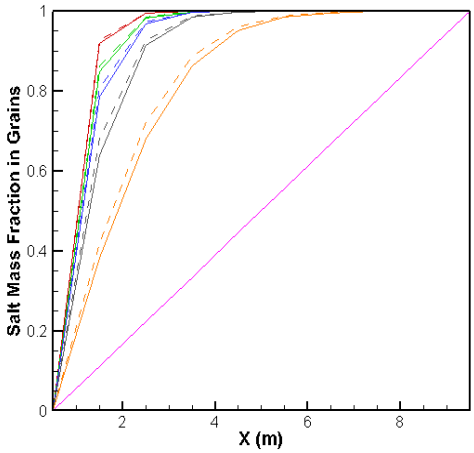

Figure 4-19. Evolution of salt mass fraction in the grains. Solid and dashed lines correspond to porosity of 0.001 and 0.7, respectively. See legend in Figure 4-16.

4.6 Applications

4.6.1 Small-scale modeling of brine inclusion migration toward the heat source

We simulated a process of small-scale brine inclusion migration toward the heat source by using the formulation presented in Section 4.3, and applying Equations (4.22)-(4.23). As inspired by laboratory experiments on salt in Caporuscio et al (2013), we applied a very high temperature gradient across a 4mm × 6mm column through a temperature difference of 120°C (top) and 100°C (bottom). In this model, we deactivated one continuum and only used a single continuum and a single component to capture the water and salt in the brine inclusion. The result of brine migration is shown in Figure 4.20, which agrees quite well with the experimental results of Caporuscio et al (2013). This example demonstrates the capability of the formulation of capturing small-scale behavior of the moving interfaces induced by a thermal gradient. Note that a more rigorous treatment would involve solving for salt dissolution and precipitation

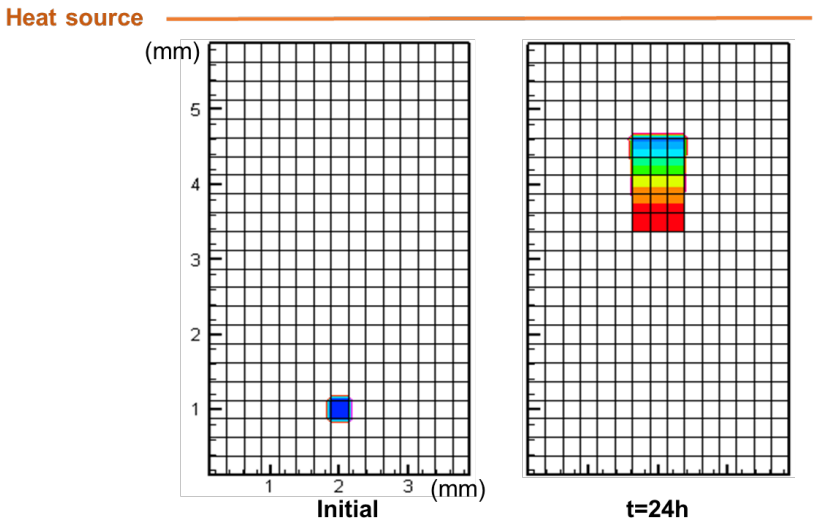

Figure 4-20. A single brine inclusion migrating toward the heat source

4.6.2 Analysis of thermal gradient effects on brine migration

In this part, we used the developed model to analyze the effect of the thermal gradient on the brine inclusion migration. The modeling geometry and boundary conditions are shown in Figure 4-21. The soret coefficient is 0.01.

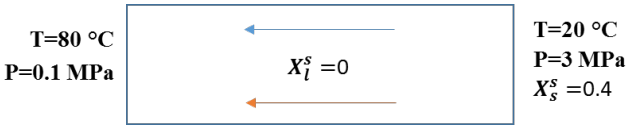

Figure 4-14. Model geometry and boundary conditions.

As the rock conducts heat rapidly, temperature was changed linearly rapidly (Figure 4-22), and the pore pressure reached steady state after 10 days, as shown in Figure 4-23. However, it took long time for the brine inclusion to migrate driven by the elevated temperature. Figure 4-24 shows the evolution of salt mass fraction in the grains. The decreased salt mass fraction close to the heat source indicates the dissolution of salt. We further calculated the flux to the left side, including the advective flux, diffusive flux and the flux associated with the brine inclusion migration. Figure 4-25 demonstrates that after 1000 days the flux, associated with the brine inclusion migration, becomes dominant and starts to surpass the advective flux. As the system gradually reaches a steady state, the flux drops. Such a case may not be realistic, but demonstrates the capability of the new model of simulating larger scale brine migration induced by a thermal gradient.

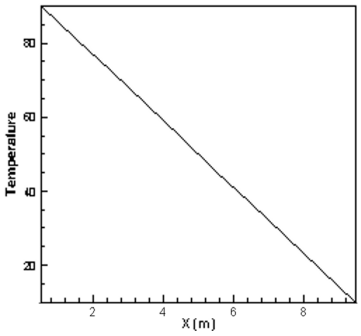

Figure 4-15. Temperature distribution

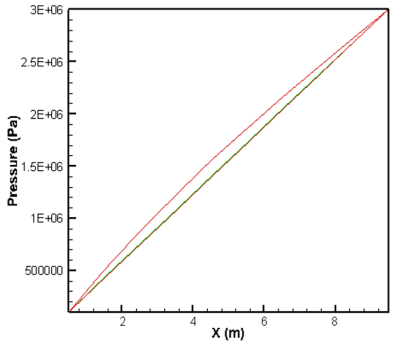

Figure 4-16. Pressure evolution

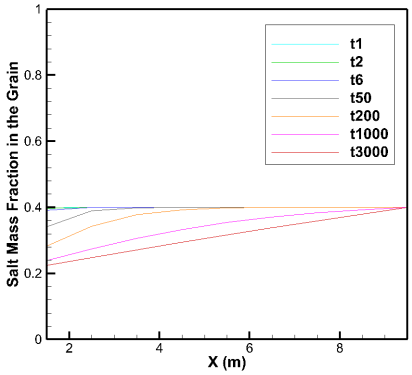

Figure 4-17. Evolution of salt mass fraction in the grains.

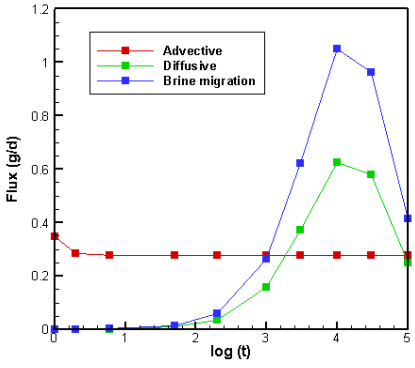

Figure 4-18. Flux change with time (day).

4.7 Summary and Perspectives

We developed a dual-continuum model for modeling brine migration in salt induced by heat that can be generated at a nuclear waste disposal site. The dual-continuum model considers flow in the interconnected pore space in terms of diffusive and advective fluxes, and also in the salt grains in terms of diffusive and thermo-diffusive fluxes. The mass balance of salt and water in these two continua are considered separately, and their coupling is represented by the flux associated with brine migration. Together with energy balance, such a system produces a coupled TH model with a strong nonlinear feature. An implicit approach, considering migration velocity as a function of temperature gradient, was used to simulate brine migration induced by thermal gradient.

An extended finite volume method (XFVM) was proposed to perform a geomechanics analysis. This method is originated based on the perspective of partitioning of unity by extending the traditional FVM linear approximation in each direction to a higher-order approximation in the entire space. We presented four different approximation approaches to construct the higher-order approximation. Within this framework, we can adaptably choose different approximation orders for mechanics, fluid flow and heat transfer for enhancing the stability of the fully coupled numerical modeling.

Step by step verification of the model was performed to assess its capabilities, including verification of hydro-mechanical coupling, thermal-hydrological coupling, diffusion in a single continuum and in dual continua. This model was further applied in both small-scale and large-scale analysis of brine migration. The results were quite reasonable. However, further verification should be conducted to compare with field experiments to build the confidence for future application.

Most of the effort in FY19 was to develop the capabilities of the geomechancis of XFVM for fully coupled analysis. Further, as XFVM is rigorous for continuum analysis, we can simulate continuum damage to detect damage on interpolation triangles and then detect failed boundaries along the cells for fracturing analysis.

5. BENVASIM CODE COMPARISON

BenVaSim is an international project for benchmarking and validation numerical simulators used for analysis of long-term coupled processes associated with nuclear waste disposal in salt. The BenVaSim project is motivated by the need of performing quality assurance of the existing numerical simulators to be able applied for real repository design. Benchmarking of coupled THM models frequently shows large variance among different researching groups. The reasons for the variance might be the use of different constitutive models, different assumptions and consideration of the processes, or different simulators. The simulators differ in the methods of discretization (such as Finite difference method, FEM, FVM), the solvers for the equations (which are based on the application of different methods to linearize the nonlinear equations and to solve the linearized equations), the equations of coupling of different physical fields and methods to realize the couplings (monolithically or sequentially). BenVaSim is proposed and designed as a benchmarking platform for different research groups to enhance the confidence for different simulators to be applied in the real nuclear waste disposal projects.

5.1 BenVaSim Benchmark Stages and Modeling Teams

BenVaSim program is divided into four stages with benchmark problems of increasing complexity. Stage 1 includes simulations of only 1-D problems, involving couplings among hydro-thermal, hydro-mechanical, or thermal-hydro-mechanical processes in homogeneous or heterogeneous media. Some of these problems have analytical solutions. Stage 2 includes simulation of problems with gradually increased complexity, starting from a simple domain geometry, and then changing drift geometry (even with multiple drifts), different creep processes, and heterogeneity (such as fault zones). Stage 3 will include 3-D simulations to demonstrate suitability of different simulators for large models. The last stage, Stage 4, will include *in-situ* or laboratory tests to be used for verification of the results of simulations (tests with and without consideration of the material viscous behavior will be designed).

Currently, the BenVaSim project has drawn interests from six different international research groups with different simulators. In particular, TUC, is using FLAC-TOUGH Kopplung simulator; Bundesanstalt für Geowissenschaften und Rohstoffe (BGR)—OpenGeoSys; Swiss Federal Nuclear Safety Inspectorate—TOUGH-FLAC, OpenGeoSys, or COMSOL; Global Research for Safety (GRS)—CODE_BRIGHT; Global Research for Safety (GRS)—TOUGH2-FLAC^{3D}-Coupling (TFC); and LBNL—TOUGH-FLAC. For BenVaSim, LBNL is also considering the FVM modeling approach as described in Section 4.

Currently, BenVaSim is in Stage 1, involving a set of 1-D problems and a comparison with available analytical solutions, and the code-to-code comparison of numerical models of different research teams. In FY18, the BenVaSim focused on modeling of Problem 1.1, which involved single-phase (liquid) flow within a fully or partially saturated system, and considering modeling of hydro-mechanical coupling. Figure 5-1 presents an overview of different scenarios considered in Problem 1.1. Figure 5-1 (an introductory slide at the BenVaSim workshop) shows the basic geometry of the 1-D problem. The model is mechanically confined (i.e., with no displacement normal to boundaries) for all sides except the left hand side boundary, which is exposed to a constant fluid pressure, corresponding to a constant stress on the left hand side boundary of 1 MPa. The interior of the model domain is subject to the initial stress with the fluid pressure of 0.1013 MPa.

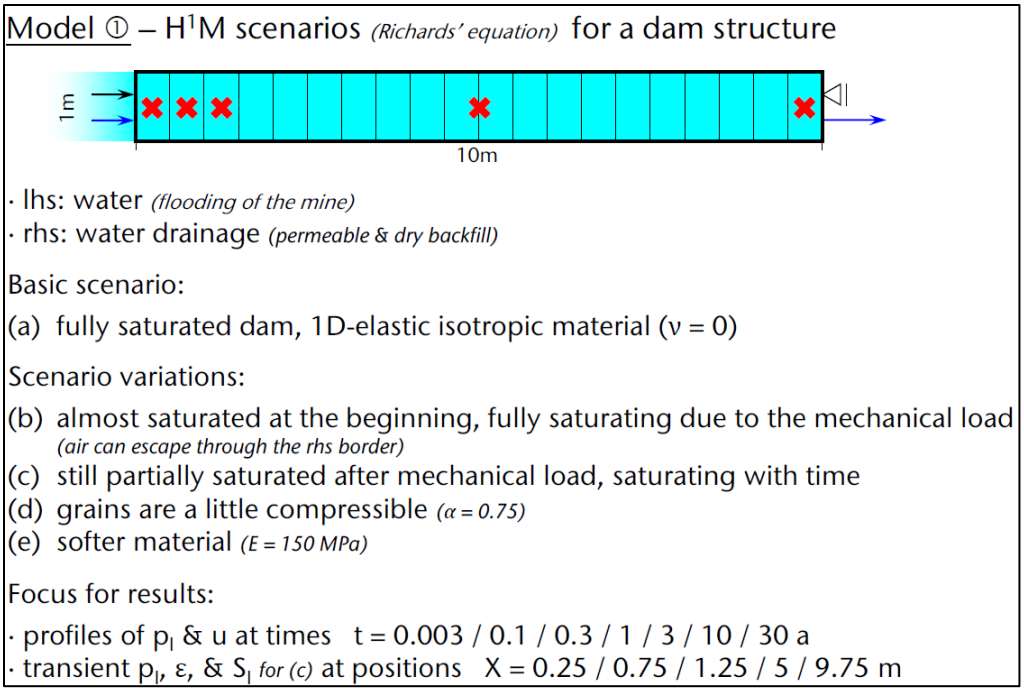

Figure 5-1. Overview of BenVaSim Problem 1.1 with scenarios (a) to (e) as presented in an introductory slide at BenVaSim workshops.

5.2 TOUGH-FLAC Modeling of Problem 1.1

An initial approach of using TOUGH-FLAC was based on the application of a simplified analysis considering "one-way pore-volume coupling" through TOUGH2 equivalent pore-compressibility. With this approach the storage due to pore-volume changes are considered not through two-way interactions with FLAC^{3D}, but through and equivalent pore-compressibility, C_p, which can be estimated by the following equation assuming uniaxial strain:

$$C_p \cong \frac{1}{K\phi}\left(1 - \frac{2(1-2\nu)}{3(1-\nu)}\right) \tag{5.1}$$

where K is the bulk modulus, ϕ is porosity, and ν is Poisson's ratio. The Poisson's ratio was fixed to ν = 0, and Young's modulus was set to E = 8 GPa in a base case, and to E = 150 MPa in a special case of a soft material in Scenario (e) (Figure 5-1). With a Poisson's ratio set ν = 0, the bulk modulus would be exactly 1/3 of Young's modulus, i.e. $K \approx 2.667$ GPa in the base case, and 50 MPa in the soft case. In all cases, the porosity is set to 0.15. Using these values, the pore compressibility can be calculated according to Equation (5.1) as C_p = 8.33e-10 Pa^{-1} in the base case, and C_p = 4.4e-8 Pa^{-1} in the soft material case.

Figure 5-2 shows a conceptual model of TOUGH-FLAC simulations. The basic mesh discretization was represented using a simple 20-element model. In the TOUGH2 simulation part, the two additional elements were added on each side to provide the hydraulic and thermal boundary conditions. Constant pressure boundary conditions were simulated by assuming a very large volume of these elements in the TOUGH2 numerical solution. Assuming a very large volume of these elements is a common TOUGH2 approach to simulate constant pressure or constant temperature conditions. All scenarios (a) to (e) listed in Figure 5-1 were simulated with TOUGH-FLAC, and good agreements were achieved with either analytical solutions or alternative numerical solutions provided by the BenVaSim secretariat at Clausthal University.

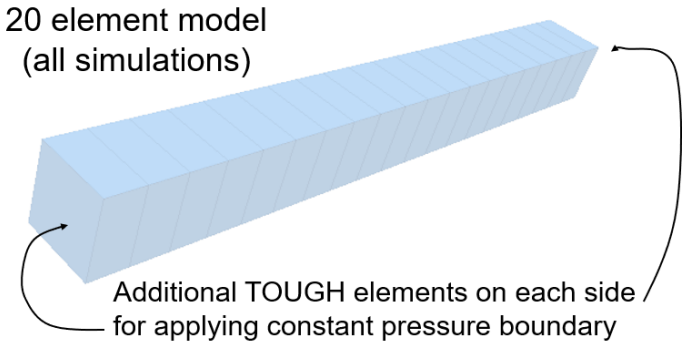

Figure 5-2. TOUGH-FLAC Model for BenVaSim Problem 1.1.

The TOUGH-FLAC simulations were conducted in two steps:

1. Mechanical loading and squeezing simulation in FLAC^{3D}, and
2. TOUGH-FLAC coupling and transient simulation.

During the initial mechanical loading and squeezing, the stress inside the model domain increases as a result of the mechanical loading provided by the fluid pressure applied on the left-hand side of the model domain. The model is also compressed, which results in an instantaneous increase in fluid pressure. In the case of a partially saturated system, the initial compression of the pores first results in an increase in saturation to full saturation and then a pressure increase due to compression of the liquid water within the pores.

Figure 5-3 shows the results for Scenario (e) when the material is soft (E = 150 MPa). In general, this case was challenging to model for the teams in BenVaSim as being prone to numerical instability in the hydro-mechanical coupling. However, when using TOUGH-FLAC with the one-way pore volume coupling through TOUGH2 pore-compressibility, the numerical solution is stable and runs quickly. Figure 5-3a shows a good agreement to the analytical solution when the pore-compressibility value is estimated according to Equation (5.1) with a value of C_p = 4.4e-8 Pa^{-1}. On the other hand, if the pore-compressibility is reduced by a factor of 2 to C_p = 2.2e-8 Pa^{-1}, the numerical results deviated from the analytical solution (Figure 5-3b). This shows that the use of Equation (5.1), which is the simplified one-way pore-volume coupling approach, provides accurate results to the fully coupled solution.

In Figures 5-4 and 5-5, the pressure and strain evolutions are presented for the case where the pore-compressibility has been calculated from Equation (5.1). Figure 5-4 shows that a good agreement is achieved for both pressure and strain over the entire 2000 years of simulations. Figure 5-4b shows an incremental strain during the transient 2nd step of the TOUGH-FLAC transient numerical simulation. During this transient phase the pressure decreases and the model is compressed. Figure 5-5 shows that during the early time some discrepancies can be observed between numerical and analytical results. This indicates that the theoretical assumptions behind Equation (5.1), i.e. uniaxial strain, may not be sufficiently accurate for the very early time.

Figure 5-6 presents the results for Scenario (a), i.e. the base case with a stiffer Young's modulus of 8 GPa. In this case, the fluid storage is much smaller, and is reflected by a much smaller pore-compressibility of C_p = 8.33e-10 Pa^{-1}. As a result, the pressure responds much faster within the model domain, and a steady state flow condition is also reached much faster. An excellent agreement between the numerical simulation results and the analytical solution is achieved for this case (Figure 5-6).

Figures 5-7 through 5-9 present results from modeling of Scenario (c), in which the porous medium is initially partially saturated at the liquid saturation of 0.3. The sample is gradually flooded from the fully

saturated, constant pressure boundary on the left-hand side. For Scenario (c), there is no analytical solution available, and, therefore, the verification is conducted by a code-to-code comparison, i.e. LBNL's TOUGH-FLAC results are compared to an alternative numerical solution provided by the BenVaSim project leaders at Clausthal University. The alternative numerical solution is simulated with FLAC-TOUGH, which is a simulator based on FLAC^{3D} and TOUGH2 developed by the Clausthal University (Blanco-Martín et al., 2015b). This simulator is based on the same basic codes as LBNL's TOUGH-FLAC simulator, but using an alternative way of coupling and running the simulations. For BenVaSim Problem 1.1, Scenario (c), the FLAC-TOUGH simulation by Clausthal University utilized the TOUGH2 EOS9 equation of state. EOS9 can be used to simulate single-phase liquid flow, according to Richards' approach, in which the gas phase is a passive spectator (Pruess et al., 2012). In LBNL's TOUGH-FLAC analysis, the TOUGH2 EOS3 equation of state was applied. EOS3 is used to simulate full multiphase flow, including both liquid and gas flow.

The first comparison of the TOUGH-FLAC-EOS3 and FLAC-TOUGH-EOS9 modeling results showed some discrepancies, which could be attributed to the difference in the EOS3 and EOS9 treatments of the gas phase (Figure 5-7a). Then, by setting artificially high gas permeability, the simulated gas pressure remained constant in the TOUGH-FLAC EOS3 simulation, and the results are in perfect agreement (Figure 5-7b). Figure 5-8 shows a detail of the evolution of liquid saturation and pressure at the 3rd element from the fully saturated constant pressure boundary on the left hand side of the model. The liquid reached this element after about 25 days when it gradually filled up with water and was fully saturated after 60 days. Thereafter, the pressure started to increase more significantly and stepwise along with the filling up of water into additional elements along the model domain. Finally, Figure 5-9 shows a good agreement between these two alternative simulators for pressure and strain.

The model comparison for Scenarios (c) of Problem 1.1 shown in Figure 5-9 was limited to comparison between two numerical simulators TOUGH2 and FLAC^{3D}. In BenVaSim, the comparison is made by the BenVaSim secretariat between all the modeling teams participating in the project. As example, Figure 5-10 shows a good agreement between 6 models related to pressure evolution for Scenario (a) of Problem 1.1.

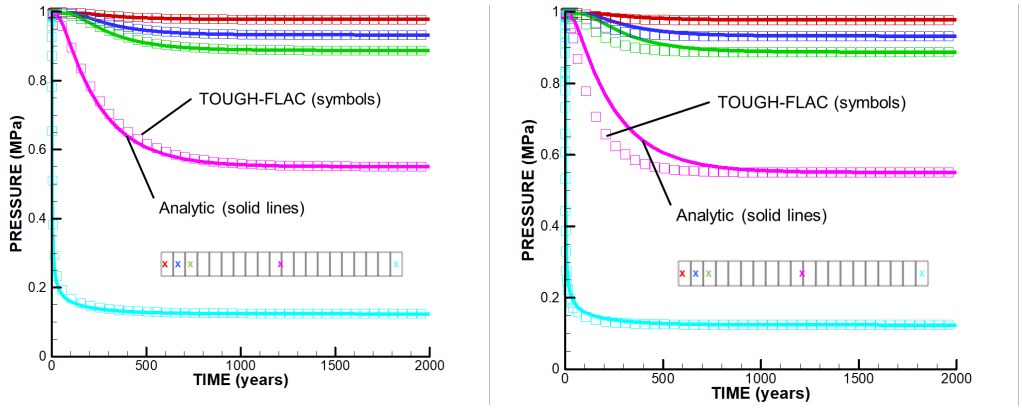

(a) (b)

Figure 5-3. Comparison of TOUGH-FLAC results with the analytical solution of pressure evolution for BenVaSim Problem 1.1, Scenario (e): (a) results when pore-compressibility is C_p = 4.4e-8 Pa^{-1} is correctly calculated from Equation (5.1), and (b) results when the pore-compressibility value of C_p = 2.2e-8 Pa^{-1}.

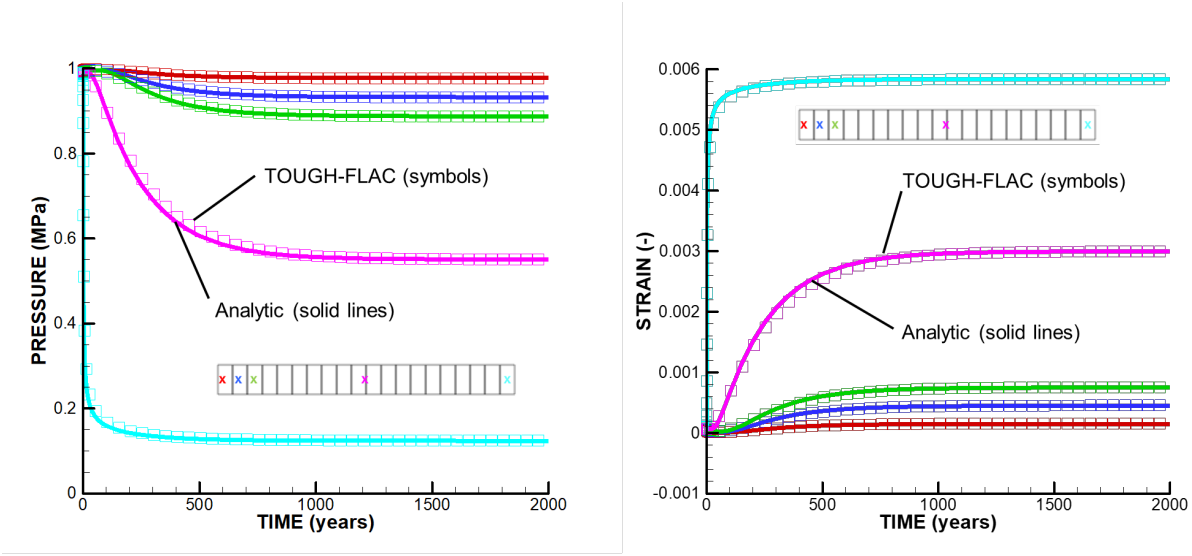

(a) (b)

Figure 5-4. Comparison of TOUGH-FLAC results with the analytical solution for BenVaSim Problem 1.1, Scenario (e): (a) pressure and (b) strain evolutions. For these results pore-compressibility is C_p = 4.4e-8 Pa^{-1} as calculated from Equation (5.1).

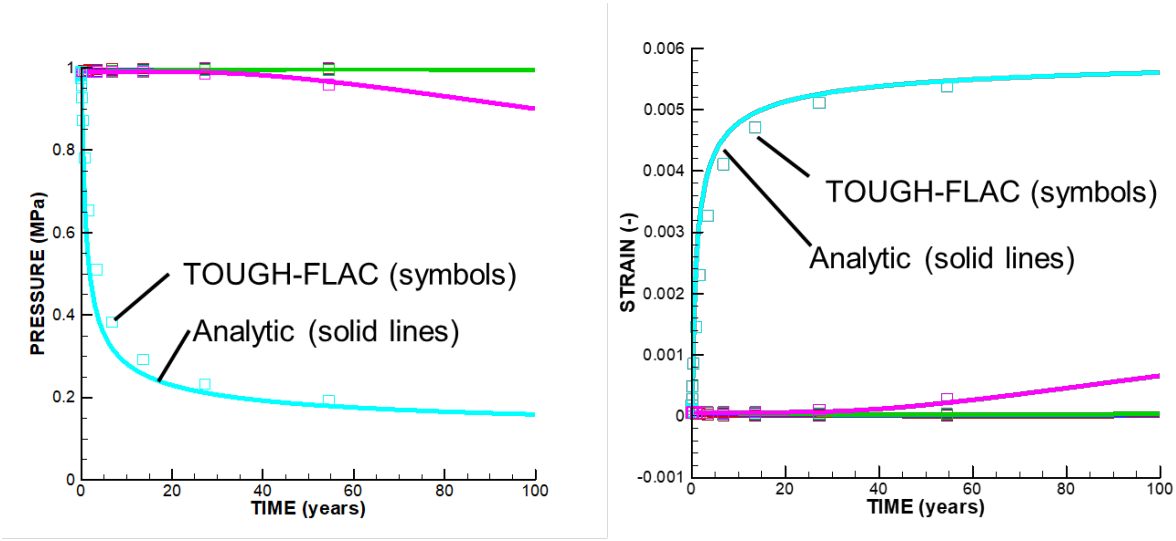

(a) (b)

Figure 5-5. Comparison of TOUGH-FLAC results with the analytical solution for BenVaSim Problem 1.1, Scenario (e): (a) pressure and (b) strain evolutions. Here we look in detail that the early time when some small discrepancies between numerical and analytical solutions can be observed.

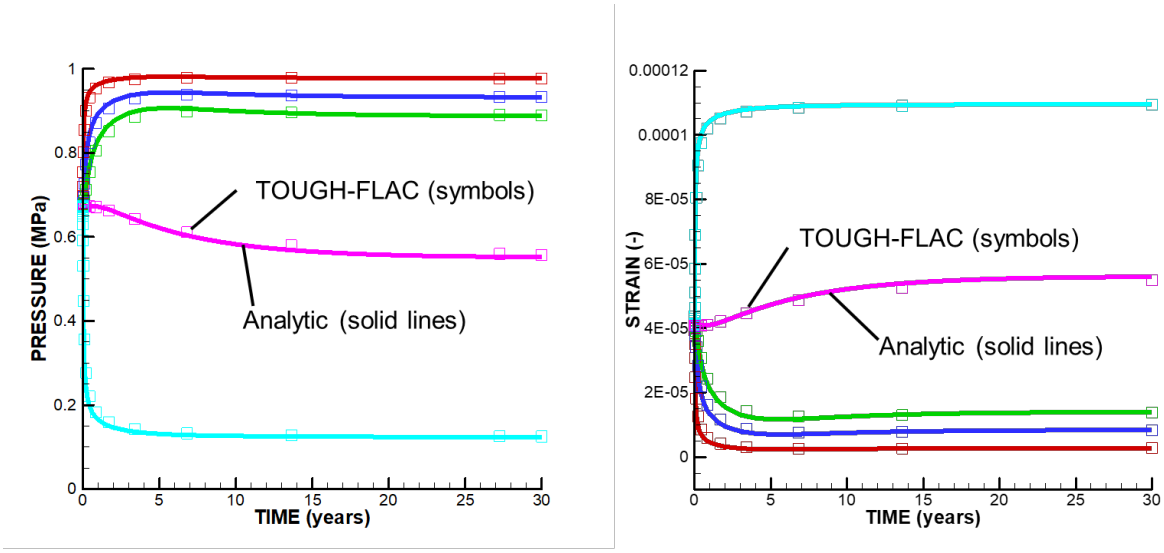

(a) (b)

Figure 5-6. Comparison of TOUGH-FLAC results with the analytical solution for BenVaSim Problem 1.1, Scenario (a): (a) pressure, and (b) strain evolutions. For these cases pore-compressibility is C_p = 8.33e-10 Pa-1 calculated from Equation (5.1).

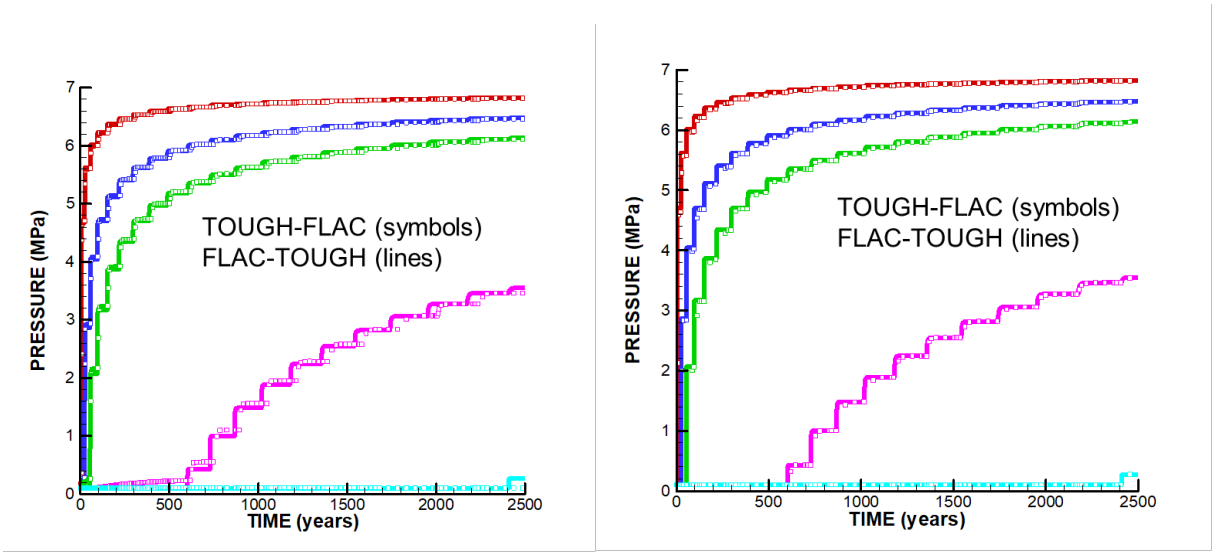

(a) (b)

Figure 5-7. Comparison of LBNL's TOUGH-FLAC-EOS3 results with alternate FLAC-TOUGH-EOS9 numerical solution provided by the BenVaSim secretariat for BenVaSim Problem 1.1, Scenario (c): (a) TOUGH-FLAC-EOS3 multiphase flow solution with slight changes in gas pressure, and (b) TOUGH-FLAC-EOS3 with extremely high gas permeability keeping gas pressure constant.

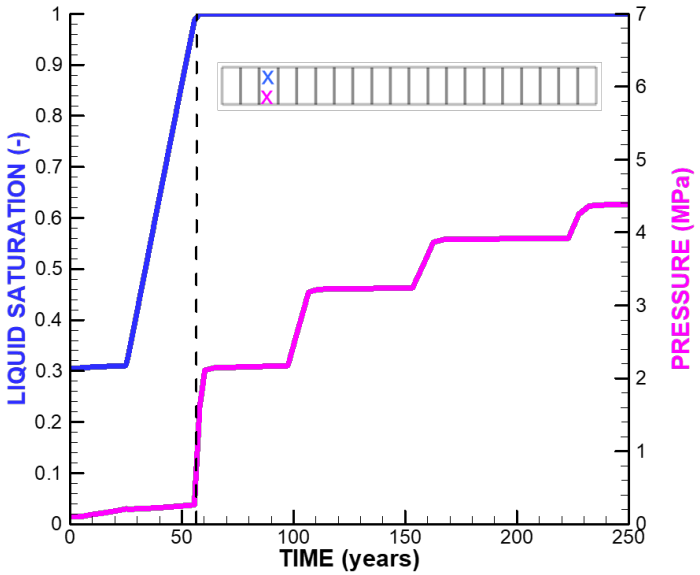

Figure 5-8. TOUGH-FLAC-EOS3 results showing the evolution of liquid saturation and pore pressure at the 3rd element from the injection point for BenVaSim Problem 1.1, Scenario (c).

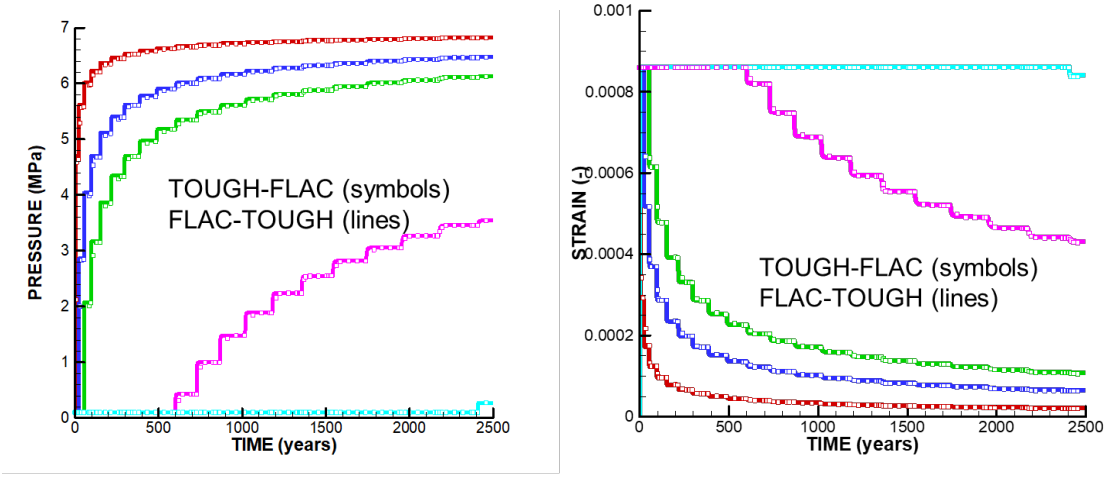

Figure 5-9. Comparison of TOUGH-FLAC-EOS3 results with the alternative numerical solution (FLAC-TOUGH-EOS9) provided by the BenVaSim secretariat for Problem 1.1, Scenario (e): (a) pressure, and (b) strain evolutions. For these results high gas permeability is assumed to assure that gas pressure remains constant in the TOUGH-FLAC EOS3 solution.

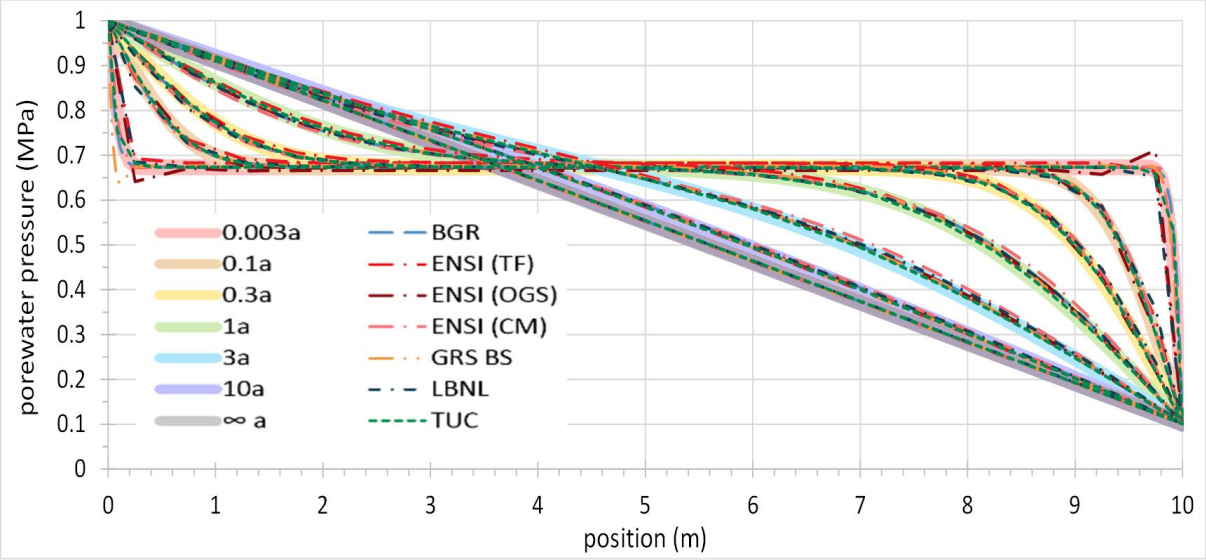

Figure 5-10. Comparison of numerical modeling results of pore pressure profiles at different times (a = years) among different BenVaSim modeling teams (modified from Rutenberg et al., 2018)

5.3 TOUGH-FLAC Modeling of Problem 1.4

In FY19, the BenVaSim has been focused on modeling of Problem 1.4, which involves two-phase (liquid) flow within a partially saturated system, and considered hydro-mechanical coupling in the solution. Figure 5-11 presents an overview of the different scenarios considered for modeling Problem 1.4. As shown in Figure 5-11, the basic geometry of the benchmark problem is 1-D. The model is mechanically confined (i.e., no displacement normal to boundaries) for all sides except the left hand side boundary, which is exposed to constant gas pressure and liquid saturation. The interior of the model domain is subject to the initial total stress of 4MP, gas pressure of 0.2 MPa, and liquid saturation of 0.63.

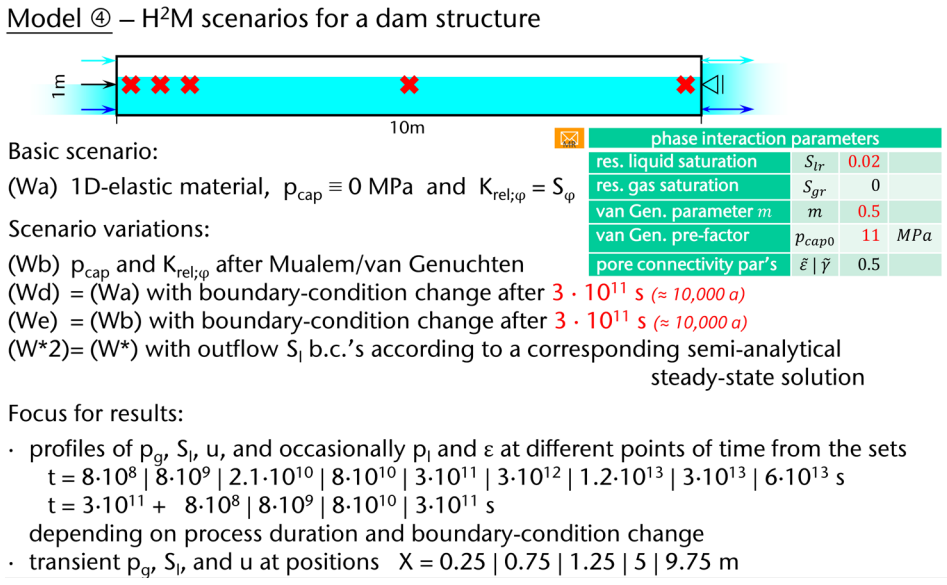

Figure 5-111. Overview of BenVaSim Problem 1.4 with scenarios (a) to (e)

In Figure 5-12, detailed boundary conditions and physical parameters for different modeling scenarios are listed.

model-1.4 scenario:			(Wa)	(Wa2)	(Wd)	(Wd2)	(Wb)	(Wb2)	(We)	(We2)
initial conditions			$\sqrt[3]{\pi^2}$	$\sqrt[3]{\pi^2}$	$\sqrt[3]{\pi^2}$	$\sqrt[3]{\pi^2}$				
total stress	σ_{tot0}	MPa	4	4	4	4	4	4	4	4
poregas pressure	p_{g0}	MPa	0.2	0.2	0.2	0.2	0.2	0.2	0.2	0.2
liquid saturation	S_{l0}		0.63	0.63	0.63	0.63	0.63	0.63	0.63	0.63
boundary conditions ($t = 0a$)										
total stress, lhs	$\sigma_{tot;lhs}$	MPa	4	4	4	4	4	4	4	4
poregas pressure, lhs	$p_{g;lhs}$	MPa	3	3	3	3	3	3	3	3
liquid saturation, lhs	$S_{l;lhs}$		0.5	0.5	0.5	0.5	0.5	0.5	0.5	0.5
poregas pressure, rhs	$p_{g;rhs}$	MPa	0.5	0.5	0.5	0.5	0.5	0.5	0.5	0.5
liquid saturation, rhs	$S_{l;rhs}$		0.9	1/7	0.9	1/7	0.9	1/7	0.9	1/7
changed boundary con's ($t \approx 10{,}000a$)										
total stress, lhs	$\sigma_{tot;lhs}$	MPa			3	3	$1/7 \approx 0.143$		3	3
poregas pressure, lhs	$p_{g;lhs}$	MPa			2	2	$7/33 \approx 0.212$		2	2
liquid saturation, lhs	$S_{l;lhs}$				0.5	7/33			0.5	7/33
poregas pressure, rhs	$p_{g;rhs}$	MPa			4	4			4	4
liquid saturation, rhs	$S_{l;rhs}$				0.35	0.35			0.35	0.35
Mualem/van Genuchten parameters										
residual liq. saturation	S_{lr}						0.02	0.02	0.02	0.02
residual gas saturation	S_{gr}						0	0	0	0
van Gen. parameter	m						0.5	0.5	0.5	0.5
van Gen. pre-factor	p_{cap0}	MPa					11	11	11	11
pore connectivity par's	$\tilde{\varepsilon} \mid \tilde{\gamma}$						0.5	0.5	0.5	0.5

parameters		
E	650	MPa
ν	0	
ϕ	0.33	
K	$2.5 \cdot 10^{-21}$	m^2
α	1	
η_l	10^{-9}	$MPa \cdot s$
K_l	2,220	MPa

Michael Kuhlberg
Chair for Waste Disposal and Geomechanics

BenVaSim project

Figure 5-12. Boundary conditions and physical parameters for different scenarios defined in BenVaSim Problem 1.4

We used a rather coarse mesh with 20 elements in TOUGH-FLAC to model the problem. We chose the Scenarios 1.4a, 1.4a2 and 1.4b and compared the results with TUC and ETH/ENSI results presented at the Berkeley Workshop in October of 2018.

Figures 5-13 and 5-14 show the results of pore gas pressure simulated by LBNL TOUGH2-FLAC compared with ETH/ENSI TOUGH3-FLAC and TUC's FLAC-TOUGH. We compared the results at 25, 250, 650, and 2500 years (reaching steady state). As we can see, our results agree quite well with both and, particularly, with TUC's FLAC-TOUGH, which used rather a fine mesh. During the simulated 2500 years, because of the very high gas pressure (3MPa) on the left hand as a constant boundary condition, the system gas pressure was gradually increased from 0.2 MPa until it reaches steady state.

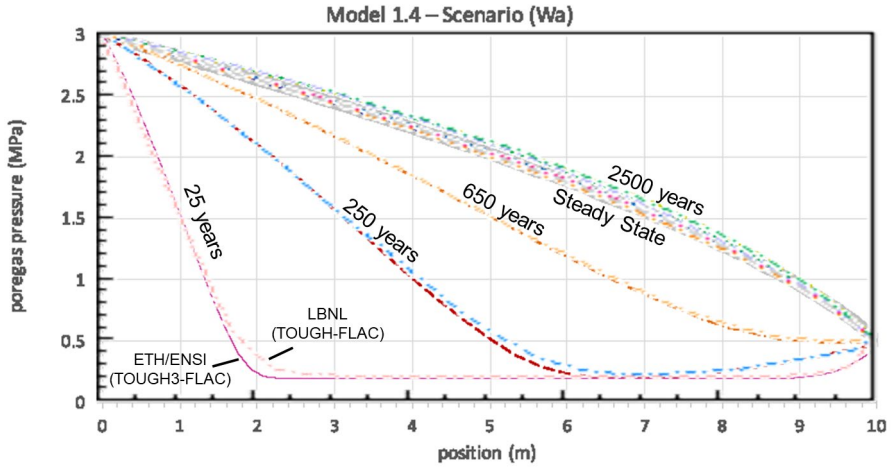

Figure 5-13. Scenario 1.4a results: gas pressure simulated by TOUGH2-FLAC and its comparison to ETH/ENSI TOUGH3-FLAC.

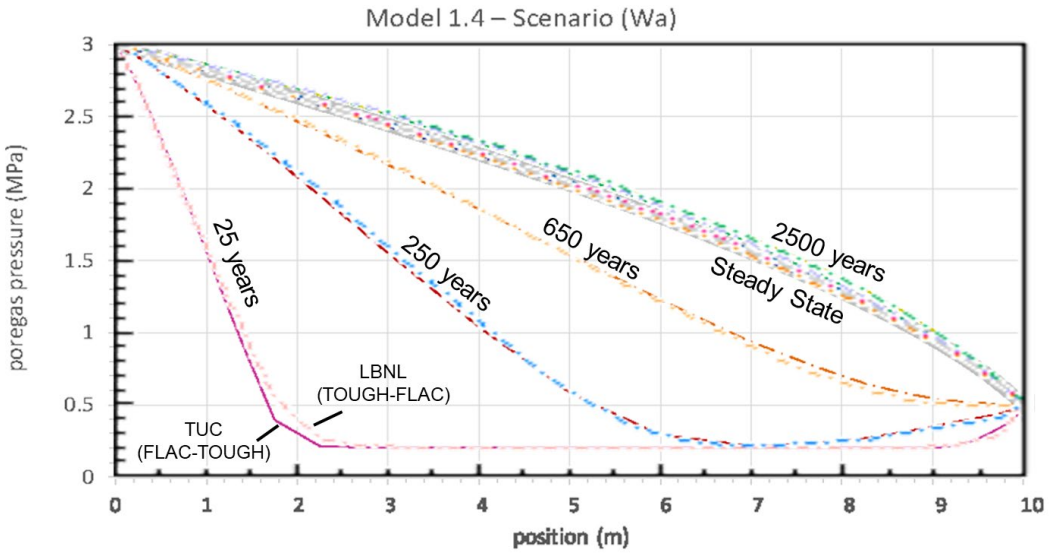

Figure 5-14. Scenario 1.4a results: gas pressure simulated by TOUGH2-FLAC and its comparison to TUC's FLAC-TOUGH.

Figure 5-15 shows the results of simulations of liquid saturation at 25, 10,000, and 100,000 years and steady state simulated by LBNL TOUGH2-FLAC and its comparison with ETH/ENSI TOUGH3-FLAC. A good agreement of simulated results was obtained, although a coarse mesh was used. The change of liquid saturation reflects the boundary conditions on the left and right sides, which slightly below and high above the initial liquid saturation. At the end, the system reaches steady, with a liquid saturation building up the left hand side, while a big jump remained at the right hand side. Such a boundary condition may not be reasonable in the real condition. Thus, a comparison of results obtained by different simulators for extreme cases provided confidence toward future applications of numerical codes.

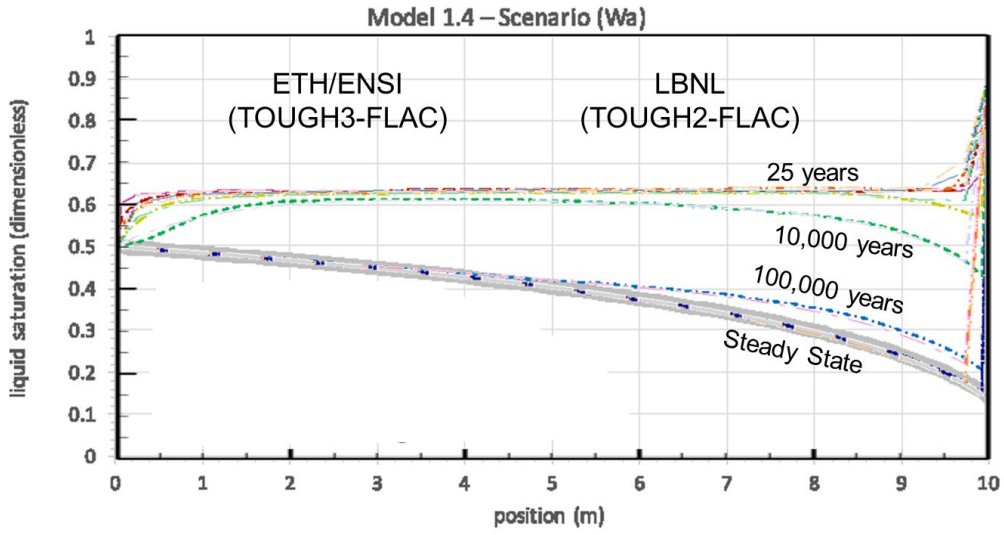

Figure 5-15. Scenario 1.4a results: liquid saturation simulated by LBNL TOUGH2-FLAC and its comparison to ETH/ENSI TOUGH3-FLAC.

We further calculated the strain and displacement calculated by LBNL TOUGH2-FLAC and compared the results with those calculated using ETH/ENSI TOUGH3-FLAC, which are shown in Figures 5-16 and 5-

17. Note that in TOUGH2-FLAC, we estimated the pore-compressibility (as described in Section 5.2 of this report) and simplified the simulation to one-way coupling. Note that for a large and dynamic deformation in the porous media, such a treatment (simplifying the coupling to one-way with reasonable estimation of pore-compressibility) may not be very accurate. But for the current scenario the effectiveness of such a treatment is proven by the agreement of the results shown in Figures 5-16 and 5-17. We see that the gas pressure pressed the 1-D dam to deform from the left hand. With the buildup of the pore pressure in the domain, more deformation and displacement occurred gradually until reaching steady state.

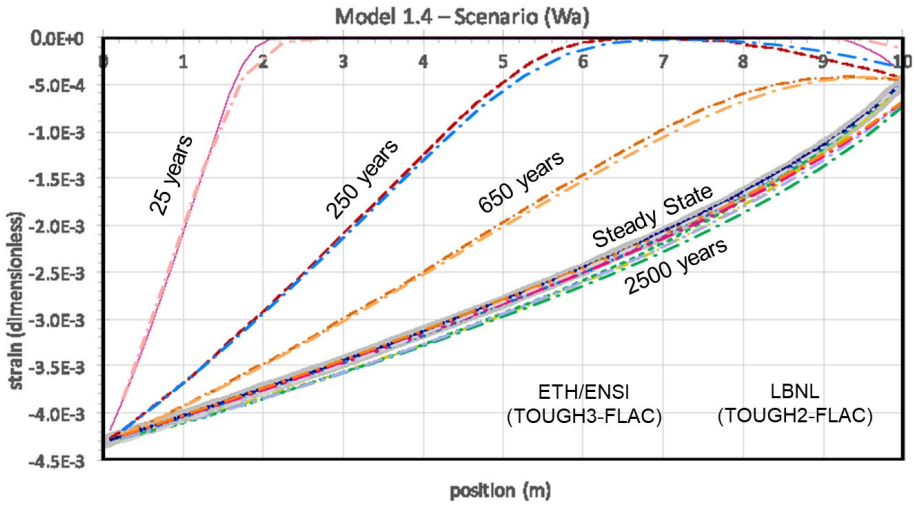

Figure 5-16. Scenario 1.4a results: strain simulated by LBNL TOUGH2-FLAC and its comparison to ETH/ENSI TOUGH3-FLAC.

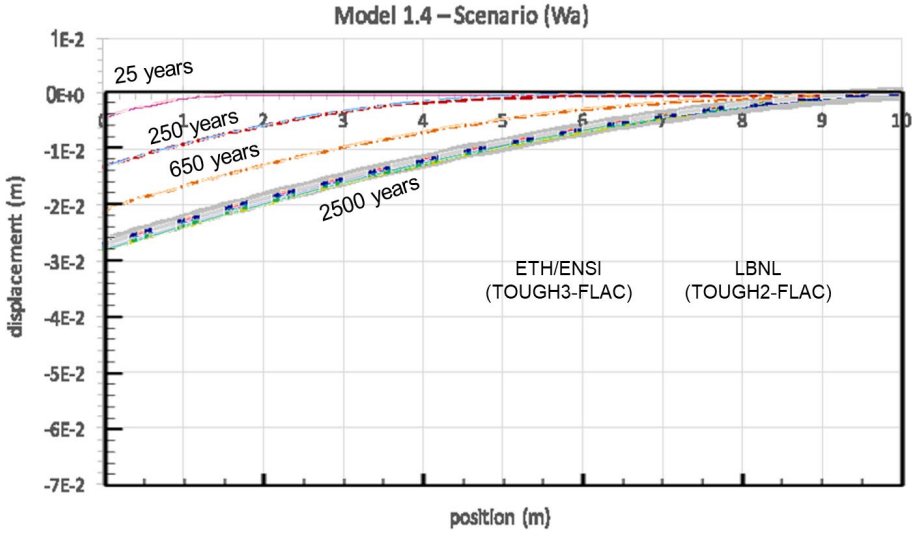

Figure 5-17. Scenario 1.4a results: strain simulated by LBNL TOUGH2-FLAC and its comparison to ETH/ENSI TOUGH3-FLAC.

As shown in Figure 5-12, Scenario 1.4a2 changes the right-hand side boundary condition of liquid saturation to 1/7. Such a drop would completely change the system behavior, which necessarily avoid the jump of liquid saturation even reaching steady state as designed in Scenario 1.4a (as shown in Figure 5-15). Figures 5-18 and 5-19 show the results of gas pressure and liquid saturated calculated by LBNL TOUGH2-FLAC and TUC FLAC-TOUGH. We compared the results at 25, 250, 650, 2500, 10,000, 100,000, and 380,000 years (reaching steady state). As we can see, the pore pressure builds up gradually in the domain,

similar to what we see in Scenario 1.4. Whereas, the saturation of liquid gradually drops in the domain until it reaches steady state, with nonlinear gradient toward the right hand side of the model domain. We see good agreement between the two simulators and with the analytical solution at the final state.

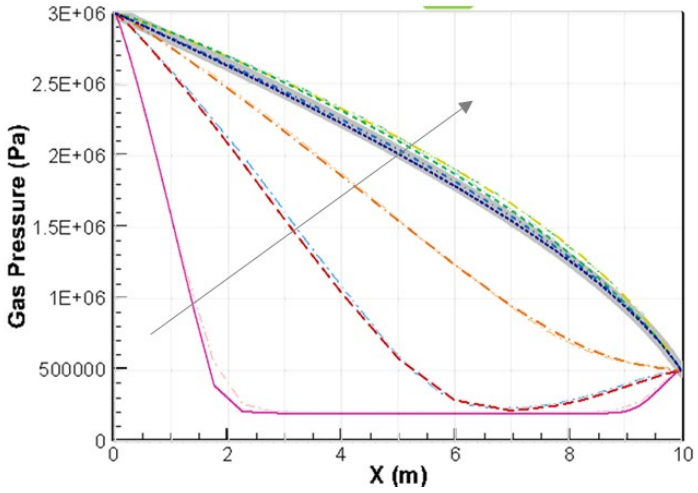

Figure 5-18. Scenario 1.4a2 results: gas pressure simulated by TOUGH2-FLAC and its comparison to TUC's FLAC-TOUGH. Here the arrow denotes the direction of time evolution.

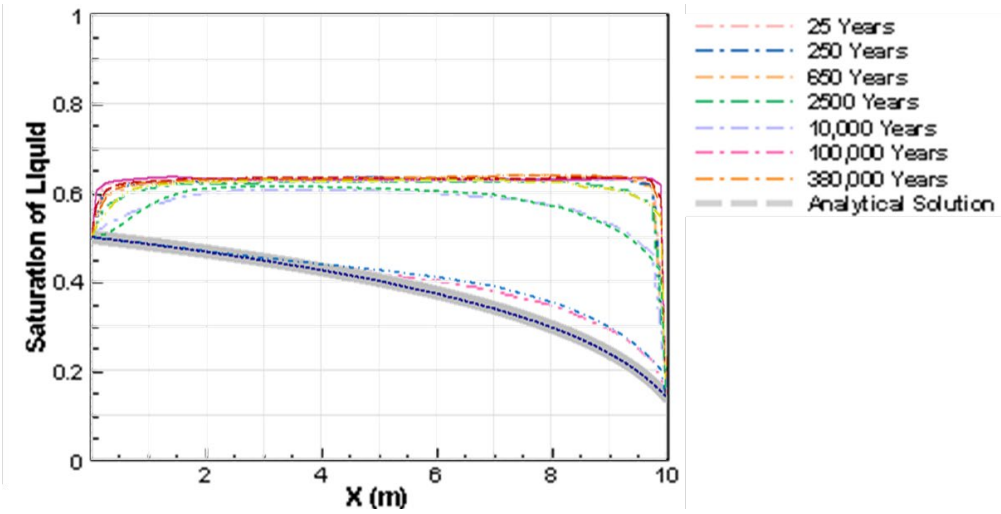

Figure 5-19. Scenario 1.4a2 results: saturation of liquid simulated by TOUGH2-FLAC and its comparison to TUC's FLAC-TOUGH.

5.4 TOUGH-FLAC Modeling of Problem 1.5

Problem 1.5 involves two-phase (liquid) flow within a partially saturated system, considering hydro-mechanical coupling in the solution. The domain is still 1-D, so that it is easier to compare the results. A notable change from 1.4 is that the domain is heterogeneous, consisting of backfill and drift seal material used to simulate a simplified nuclear waste disposal site. Figure 5-20 presents an overview of the different scenarios considered in Problem 1.5. The model is mechanically confined (no displacement normal to boundaries) for all sides except the left hand side boundary, which is exposed to a constant gas pressure

and liquid saturation. The interior of the model domain is subject to the initial total stress of 4MP, gas pressure of 0.2 MPa, and liquid saturation of 0.63.

Model ⑤ – H²M scenarios for a backfilled and sealed drift

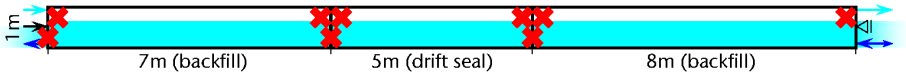

Basic scenario:

(Wa) two different parameter sets for backfill and drift seal, 1D-elastic materials, phase interactions *(M/vG)*

Scenario variations *(all based on (Wa))* :

(Wb) $p_{cap} \equiv 0$ MPa and $K_{rel;\varphi} = S_\varphi$
(Wc) "dummy seal" *(only backfill everywhere)*
(Wd) more permeable seal *(larger K)*
(We) only H² processes
(Wf) seal with lower suction *(M/vG parameters equal to those of the backfill)*
(Wg) softer backfill material *(lower E)*
(Wh) coarser backfill material *(larger ϕ)*

Focus for results:

· profiles of p_g, S_l, u, & ε *(for scenario (Wb))*
at t = 5·10⁶ | 5·10⁸ | 2·10⁹ | 5·10⁹ | 5·10¹⁰ | 5·10¹¹ s & steady state *(FTK: 2.5 to 5 ·10¹² s)*
≈ 0.16 | 16 | 63 | 160 | 1,600 | 16,000 a

· transient p_g, S_l, & u at positions X = 0.25 | 6.75 | 7.25 | 11.75 | 12.25 | 19.75 m /
transient u at positions X = 0 | 7 | 12 m instead

Figure 5-20. Schematic of BenVaSim Problem 1.4 with scenarios (a) to (e)

Figure 5-21 provides a summary of boundary conditions and physical parameters used for simulations of the base modeling Scenario (1.5a).

Basic scenario:

(Wa) two different parameter sets for backfill and drift seal, 1D-elastic materials, phase interactions *(M/vG)*

material parameters		backfill		drift seal	
Young's modulus *(drained)*	E	200	MPa	650	MPa
Poisson's ratio	ν	0		0	
porosity	ϕ	0.3		0.2	
intrinsic permeability	K	$2 \cdot 10^{-19}$	m^2	10^{-20}	m^2
Biot coefficient	α	1		1	
residual liquid saturation	S_{lr}	0.1		0.1	
residual gas saturation	S_{gr}	0		0	
van Genuchten parameter m (or λ)	m	0.4		0.35	
van Genuchten pre-factor	p_{cap0}	5	MPa	6	MPa
pore connectivity parameters	$\tilde{\varepsilon}$ & $\tilde{\gamma}$	0.5		0.5	

steady state with FTK: t = 3·10¹² s *(≈ 100,000 a)*

phase properties			
liq. bulk modulus	$\tilde{K}_l$	2,220	MPa
liquid density	ρ_l	1,000	kg/m^3
liquid viscosity	η_l	10^{-9}	$MPa \cdot s$
gas viscosity	η_g	$1.8 \cdot 10^{-11}$	$MPa \cdot s$

initial conditions			
total stress	σ_{tot0}	4	MPa
pore-gas pressure	p_{g0}	0.2	MPa
liquid saturation	S_{l0}	0.63	

boundary conditions			
lhs total stress	$\sigma_{tot;lhs}$	4	MPa
lhs pg. pressure	$p_{g;lhs}$	3	MPa
lhs liq. saturation	$S_{l;lhs}$	0.5	
rhs pg. pressure	$p_{g;rhs}$	p_{g0}	
rhs liq. saturation	$S_{l;rhs}$	S_{l0}	

Figure 5-21. Boundary conditions and physical parameters for Scenario 1.5a defined in BenVaSim

We used 100 elements (each element is 0.2m wide) in TOUGH-FLAC to model the problem, as shown in Figure 5-22. We chose the Scenarios 1.5a,b, e, and compared some of the results with TUC results obtained by FLAC-TOUGH. Scenario 1.5e is a special case of 1.5a only considering flow, while 1.5b does not consider capillary pressure and assumes relative permeability is a function which is equal to saturation.

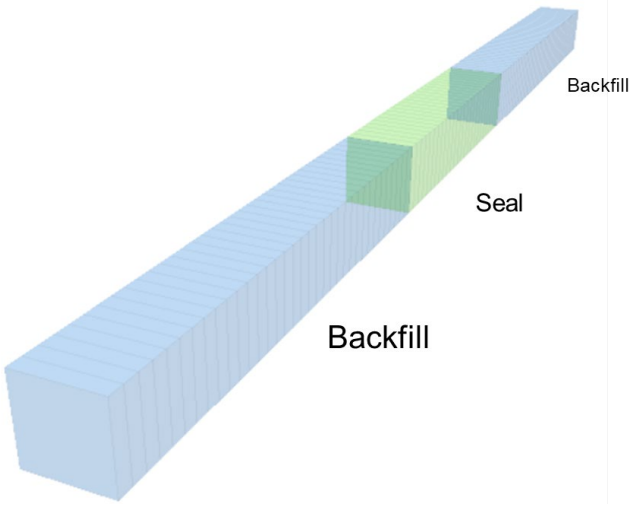

Figure 5-122. TOUGH2-FLAC mesh for BenVaSim Problem 1.5

Figures 5-23 and 5-24 show the results of the liquid saturation and the pore water pressure calculated by LBNL TOUGH2-FLAC and a comparison with TUC's FLAC-TOUGH. We compared the results at 0.16, 16, 63, 160, 1600, 16,000 and 160,000 years (reaching steady state). Overall, our results agree quite well with TUC's FLAC-TOUGH. The liquid within the left side backfill is gradually displaced by the gas. Similar trend is found at the right side backfill and in the seal at 160 years. Because the seal has less permeability than the backfill, the dissipation of the liquid occurs through the two ends of the seal, leading to a small amount of water at its center at 1600 years. Impacted by the fixed liquid saturation at the left and right sides (0.5 and 0.63), in the seal the water pressure builds up a gradient with a higher pressure at the right and uniformly drops to steady state in the seal.

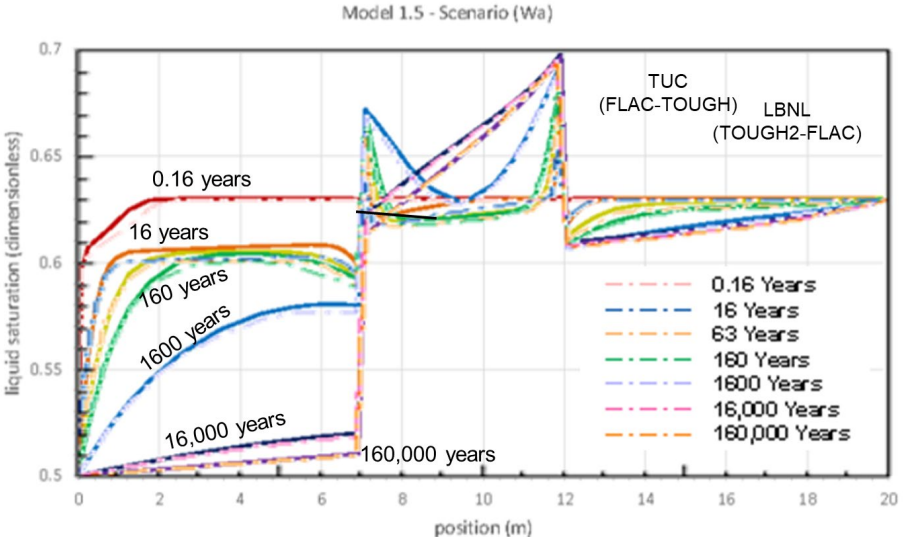

Figure 5-23. Scenarios 1.5a and 1.5e results: liquid saturation simulated by TOUGH2-FLAC and its comparison to TUC's FLAC-TOUGH.

Figure 5-24 shows liquid pressure is shown for Scenario 1.5a and 1.5e, with comparison to TUC FLAC-TOUGH. Overall, the two model agree quite well on pore water pressure. The largest deviation is found at

16 years, which may be partially due to rounding error of transferring seconds to years by TUC. Another explanation is the van-Genuchten model parameters. As we can see, the magnitude of the negative pore water pressure reduces at the left side backfill due to increase of the gas pressure. Later, the magnitude of negative water pressure increases due to the deformation of the sample. The pore water pressure in seal is mostly influenced by its saturation as the seal is less deformable than the backfill.

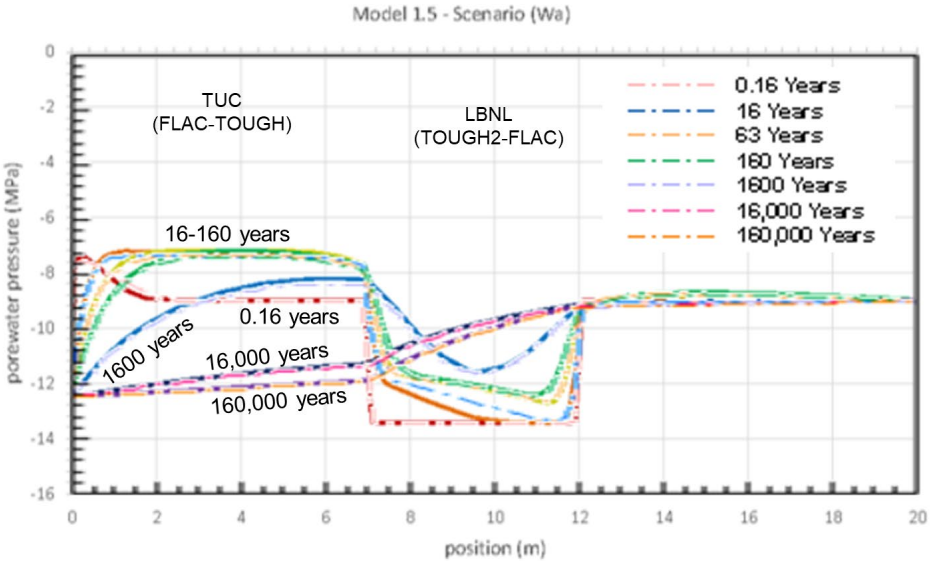

Figure 5-24. Scenario 1.5a and 1.5e results: pore water pressure simulated by TOUGH2-FLAC and its comparison to TUC's FLAC-TOUGH.

Figure 5-25 shows gas pressure results simulated by LBNLTOUGH2-FLAC and TUC FLAC-TOUGH are compared. Despite the large deviation at 16 years, the two models agree well. We see the buildup of gas pressure from left to right, with a much larger gradient in the seal due to low permeability. And both models showed the same gas pressure distribution after 63 years (note that it takes much longer for the liquid to reach steady state).

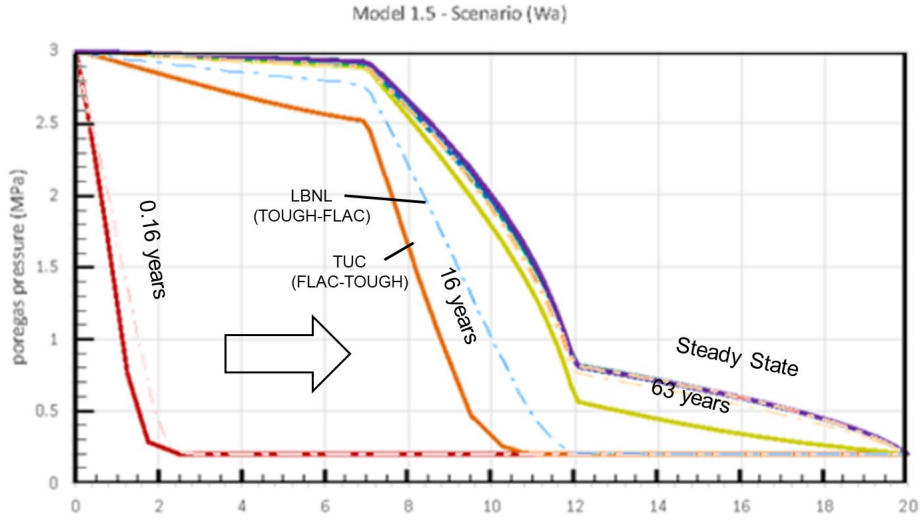

Figure 5-25. Scenarios 1.5a and 1.5e results: gas pressure simulated by TOUGH2-FLAC and its comparison to TUC's FLAC-TOUGH.

We further compared the displacement calculated by TOUGH2-FLAC and TUC's FLAC-TOUGH. In the left hand side of the backfill, the displacement increases with the increase of pore water pressure until 160 years. Then, with the decrease of the pore water pressure, the displacement decreased until it reached steady state at 160,000 years. In the seal zone, the strain (i.e., the gradient of the displacement) is smaller due to a stiffer material. We see good agreement between the simulators except for a small deviation occurring at 16 years.

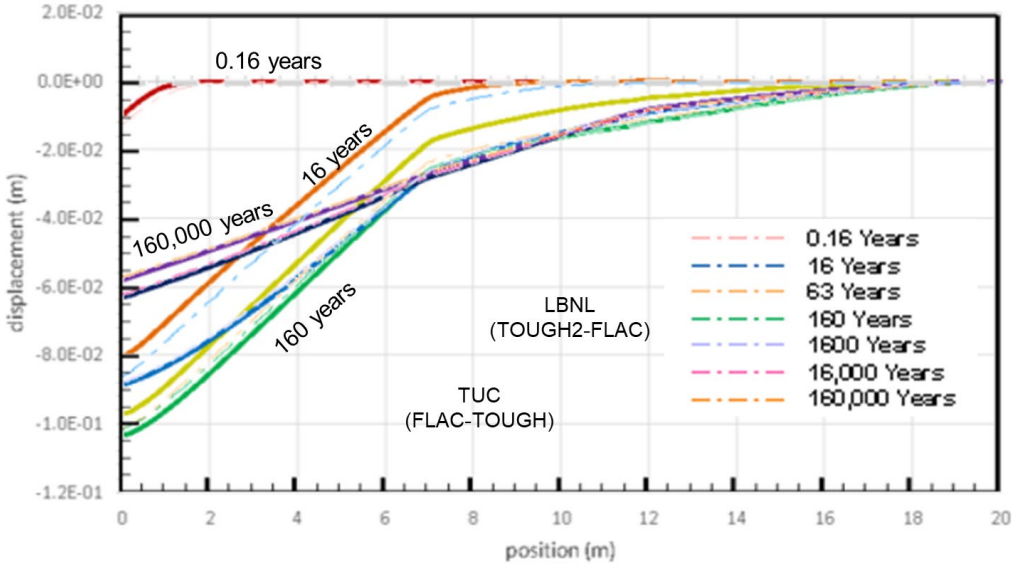

Figure 5-26. Scenario 1.5a results: displacement simulated by TOUGH2-FLAC and comparison to TUC's FLAC-TOUGH.

We also simulated Scenario 1.5b, in which the capillary pressure and relative permeability were different from 1.5a and 1.5e. As there are no results to compare from other teams, we only show the results by LBNL TOUGH2-FLAC—gas pressure, liquid saturation, and displacements, shown as Figures 5-27, 5-28, and 5-29. The results are at 0.16, 16, 63, 160, 1600, 16,000 and 160,000 years.

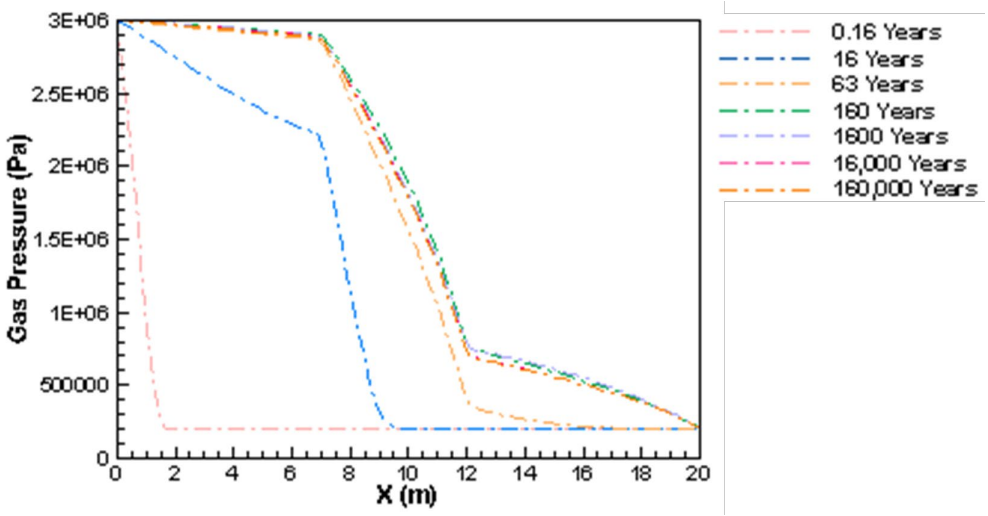

Figure 5-27. Scenario 1.5b results: gas pressure simulated by TOUGH2-FLAC

As we can see in Figure 5-27, first the gas pressure gradually builds up in the domain and reaches steady state at 16,000 years. As shown in Figure 5-28, the increase of gas saturation displaces the liquid gradually,

leading to a gradual drop of liquid pressure until 160,000 years reaching steady state. Meanwhile, the displacement in the system gradually increases until 16,000 years, reaching steady state (shown in Figure 5-29). We will compare these results with those from other teams, when those are available.

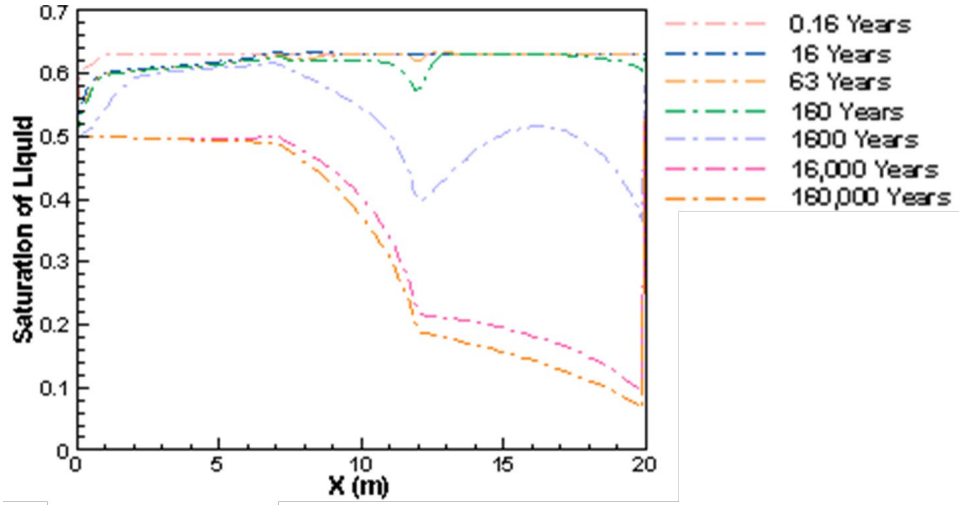

Figure 5-28. Scenario 1.5b results: liquid saturation simulated by TOUGH2-FLAC

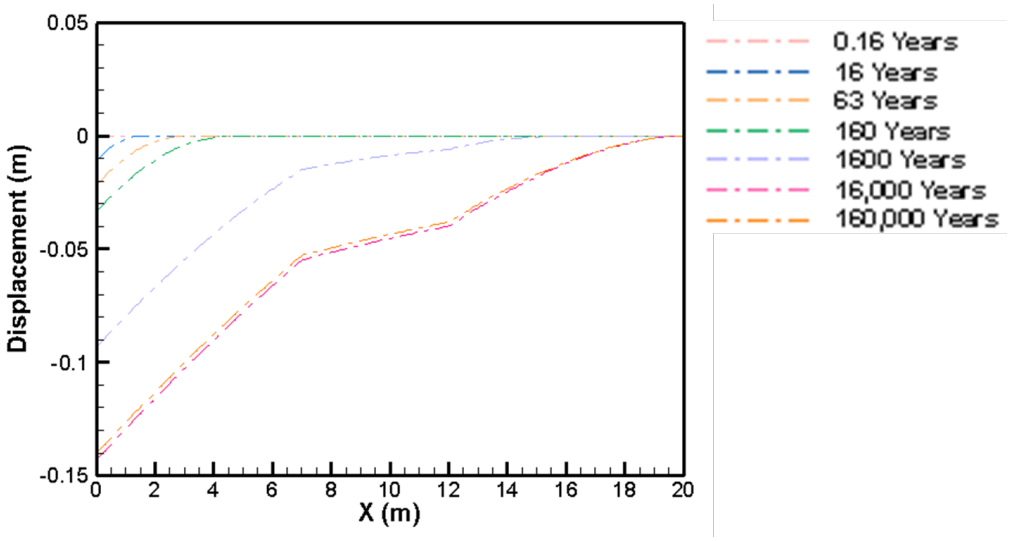

Figure 5-29. Scenario 1.5b results: displacement simulated by TOUGH2-FLAC

5.5 Summary and Plans for BenVaSim

All Scenarios (a) to (e) of Problem 1.1, Scenarios 1.4a and 1.4a2, 1.5a, 1.5b and 1.5e were simulated with TOUGH-FLAC, and good agreements were achieved with either analytical solutions or alternative numerical solutions provided by the BenVaSim secretariat at Clausthal University (TUC). We are planning to continue next with Problem 1.5 and 2-D examples once the problems are well set and described. In the future, we will be able to present more complete model comparison among the several BenVaSim participants.

This page intentionally left blank.

6. MODELING OF SMALL-DIAMETER BOREHOLE TEST

This section presents the status of the TOUGH-FLAC coupled THM modeling of the small-diameter borehole tests. During the course of the development of this experiment, the model simulations are expected to include both pre-test and post-test simulations, i.e., before and after the actual experiments are performed at WIPP. Key questions that the pre-test modeling can help answer are:

- How much heat load to apply?
- How much will the borehole close?
- What inflow rates to expect?
- How to design the monitoring system (i.e., borehole and sensor locations, mechanical pressure, ERT)?

Subsequently, the post-test modeling can be used to

- Model observed brine inflow and closure
- Calibrate and fine-tune constitutive model parameters (creep and damage)
- Learn about brine migration—intergranular, intragranular (brine-inclusions), thermal pressurization, and damage induced

A number of TH and THM simulations, including parameters studies, were presented in our FY17 progress report (Rutqvist et al., 2017). A concise summary of key results related to some of the questions was provided in the FY18 report (Rutqvist et al., 2018). In this section, we provide results of additional simulations related to some of the field test activities conducted at the WIPP site, particularly, related to Phase 1 “shake-down testing” in existing boreholes and the upcoming Phase 2 experiments in recently drilled boreholes (Mills et al., 2019; Stauffer et al., 2019).

6.1 Model Setup

The original model setup developed in Rutqvist et al. (2017; 2018) were based on a generic proposed layout of a test borehole of 10.2 cm (4 inch) in diameter and 6.1 m deep, with some monitoring boreholes located about two borehole radius distances from the test borehole. Because of symmetric and isotropic conditions, such as isotropic stress, the model simulations were conducted using either 1-D radial or 2-D axisymmetric model geometry, as shown schematically in Figure 6-1. The current design of the Phase 1 shake-down test and the upcoming Phase II experiment allows for 1-D radial and 2-D axisymmetric modeling for preliminary predictions and sensitivity analysis. Later, when conducting interpretative modeling of the Phase II experiment, other model geometries, such as full 3-D, might be developed if deemed necessary. One difference to be considered is that the actual diameter of the test hole is 12.2 cm (4.8 inch).

The 1-D axisymmetric geometry is modeled in TOUGH2 and TOUGH-FLAC as a 9° piece-of-a-cake model that is 1 m thick, i.e. corresponding to a 1 m section of the borehole. The inner boundary is at a radius that is equal to the borehole radius, and the outer boundary of the model domain is placed at the radius of 5 m. The outer model boundary is subject to constant fluid pressure, temperature and stress, whereas lateral, top and bottom boundaries are no-flow and no displacement normal to the boundary surfaces.

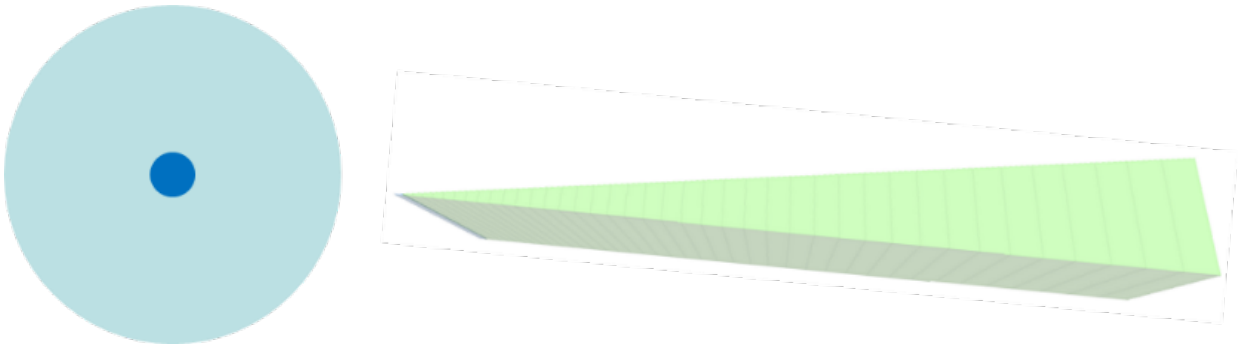

(a)

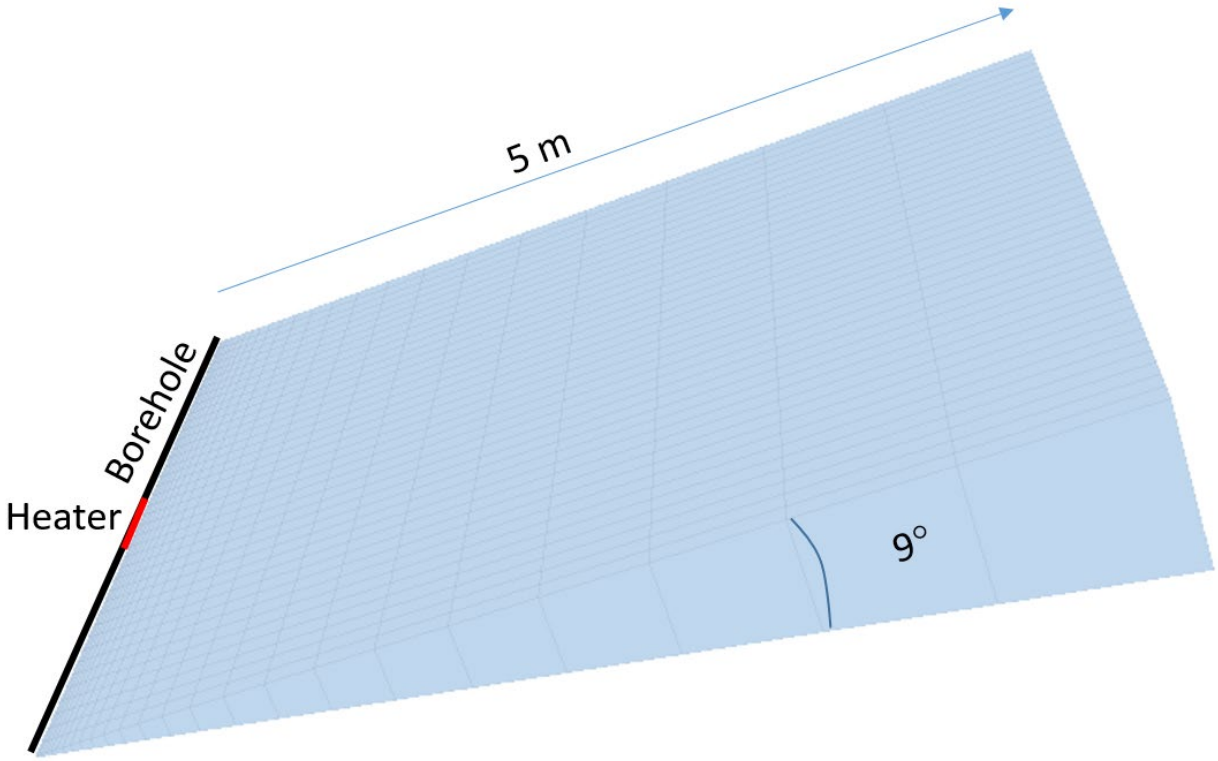

(b)

Figure 6-1. Axisymmetric model geometry simulated in TOUGH2 and TOUGH-FLAC as a 9° piece-of-cake model that is 1 m thick. Thus, 1 m of the borehole is modeled corresponding to a (a) 1-D axisymmetric model, and (b) 2-D axisymmetric model.

6.2 Material Properties and Initial Conditions

Basic material properties and initial conditions used in modeling of the small-diameter borehole experiment are listed in Tables 6-1 and 6-2. In general, many of these parameters have been developed over the past few years during applications of TOUGH-FLAC associated with the application of *Lux/Wolters* constitutive THM model for rock salt to various scenarios, including generic repository simulations as described in previous milestone reports (Rutqvist et al., 2014; 2015; 2016). Thus, some of the parameters have not been derived for specific application to the WIPP site, and therefore further refinements of parameter values can be done in the future using previous and new experimental data on WIPP salt.

Table 6-1. Mechanical and flow properties of natural salt.

Property [unit]	**Value**
Grain density, ρ [kg·m^{-3}]	2,200
Bulk modulus, K [MPa]	16,650[b]
Shear modulus, G [MPa]	7,690[b]
Thermal expansion coefficient, α_T [K^{-1}]	4×10^{-5}
Biot's parameter, α [-]	0.003 [a]
Relative permeability function	Corey
Residual liquid saturation, S_{lr} [-]	0.1
Residual gas saturation, S_{gr} [-]	0
Van Genuchten's λ [-]	0.6
Van Genuchten's P_0 [MPa]	5.7[a]
Van Genuchten's S_{lr} [-]	0.01

[a]non-constant value
[b]values are damage- and healing- dependent

Table 6-2. Initial conditions and parameter values.

Parameter [unit]	**Value**
Saturation, S_l [-]	1
Porosity, φ [-]	0.01 to 0.001
Permeability, k [m^2]	1×10^{-22} – 4.9×10^{-21}
Specific heat, C [J·kg^{-1}·K^{-1}]	860
Thermal conductivity, λ [W·m^{-1}·K^{-1}]	4
Initial stress, σ [MPa]	14.8
Initial fluid pressure, P [MPa]	5.9 –12

The initial stress at the WIPP site is taken as 14.8 MPa, based on the weight of the overburden rock. The stress field is assumed to be isotropic, which is reasonable as a result of long-term creep deformations

(Hansen, 2003). The values of bulk and shear modulus given in Table 7-1 are somewhat lower than the usually quoted values in the WIPP reference model, K = 20.7 GPa, and G = 12.4 GPa. These elastic properties will have some effect on the initial elastic response during the simulated drilling, but does not impact the longer-term creep deformation and borehole closure.

For the creep deformations, we used the Lux/Wolters model parameters that we previously applied in TOUGH-FLAC modeling of *in situ* experiments at Asse Mine and other generic salt mechanical studies (Blanco-Martín et al., 2015a, b). These parameters were not specifically developed for WIPP salt, but in the FY17 progress report (Rutqvist et al., 2017), we validated the creep parameters for WIPP by modeling borehole closure at historic field experiments at WIPP. We also compared the creep results to the results of the alternative WIPP constitutive creep model available in FLAC^{3D}. As shown in Rutqvist et al. (2017), we found that the rates of calculated and measured borehole closure for those historic WIPP experiments were in agreement, which gives confidence to the constitutive model parameters used for prediction borehole closure at the proposed small-diameter experiments.

The selected hydraulic parameters, including porosity and permeability, were justified in the FY17 progress report (Rutqvist et al., 2017), and are based on field observations at the WIPP site (e.g., Roberts et al., 1999; Beauheim et al., 1997). The pore pressure is a parameter difficult to measure *in situ* in salt. It is generally believed that pore pressure in undisturbed salt at the WIPP site could be somewhere between hydrostatic pressure (approximately 5.9 MPa) and lithostatic (approximately 14.8 MPa). In simulation results presented in this section, an initial pore pressure of 12 MPa (a few MPa less than lithostatic) was used.

6.3 Pre-test Modeling of Borehole Closure and Brine Inflow

In FY17 and FY18, model simulations were conducted based on the potential test design as presented in Kuhlman et al., (2018). These were THM simulations of borehole closure and brine-inflow using TOUGH-FLAC with the *Lux/Wolters* THM constitutive model. We simulated two cases corresponding to the first two borehole experiments proposed by Kulhman et al. (2017):

Case 1: 200 days of brine-inflow with no heat load (non-heated borehole)

Case 2: 30 day of no heat followed by 90 days of heating up to 120 °C (heated borehole)

The Case 2 involves an assumed initial time of an open borehole for 30 days before the test equipment is completely installed and the heater is turned on. Also, we included an additional 80 days after the heater was turned off to study potential effects of the rapid cooling on the inflow and borehole closure rates.

Figures 6-2 to 6-6 present key results for a set of base-case properties with an initial undisturbed permeability of halite of 0.1×10^{-21} m^2, an initial porosity of 0.01 (i.e., 1 %), and an initial fluid pressure of 12 MPa, i.e., a few MPa less than lithostatic, and close to 100% relative humidity in the test borehole.

Figure 6-2 shows the temperature and pressure evolution at two points, one at a radius of 0.067 m, which is close to the borehole wall, and one at a radius of 0.17 m. The thermal pressurization is shown as a spike in fluid pressure right after the turn-on of the heater at 30 days. This pressure spike is up to 20 MPa at 0.17 m radius. The pressure then declines due to filtration toward the open borehole. At 0.067 m, the pressure increase is very small due to damage induced permeability enhancement and proximity to the open borehole.

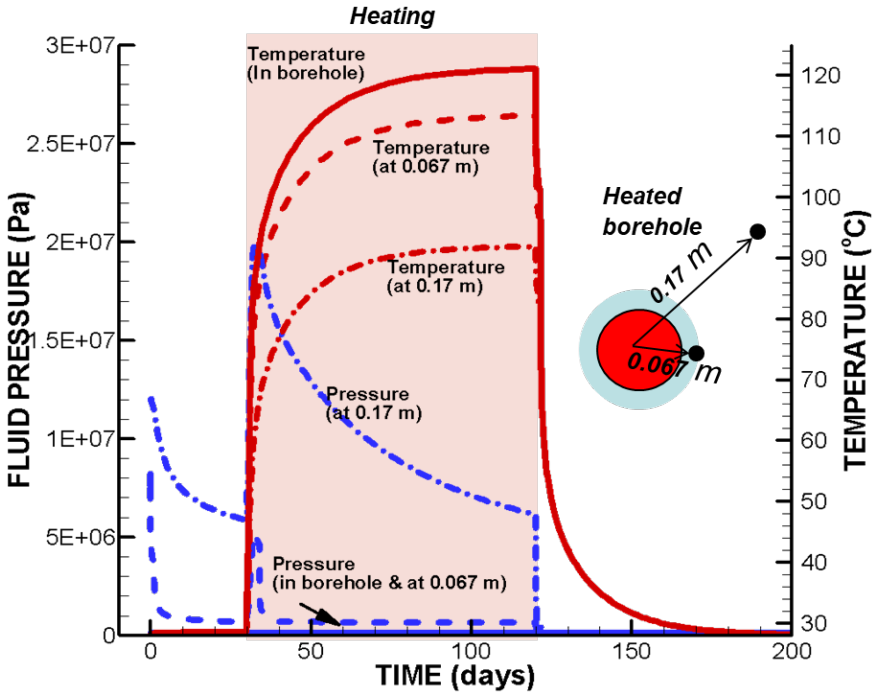

Figure 6-2. TOUGH-FLAC simulated pressure and temperature response close to the borehole for a small-diameter borehole test at WIPP.

Figure 6-3 shows the evolution of the borehole closure. The key results from this figure are that the borehole closure is very small, practically negligible, during the first 30 day of a non-heated open hole. The closure during that time period is only about 0.3 mm. After turning-on of heating, the closure rate is dramatically increased and finally after 90 days of heating, the borehole closed almost 1 cm, which is about 10% of its original diameter.

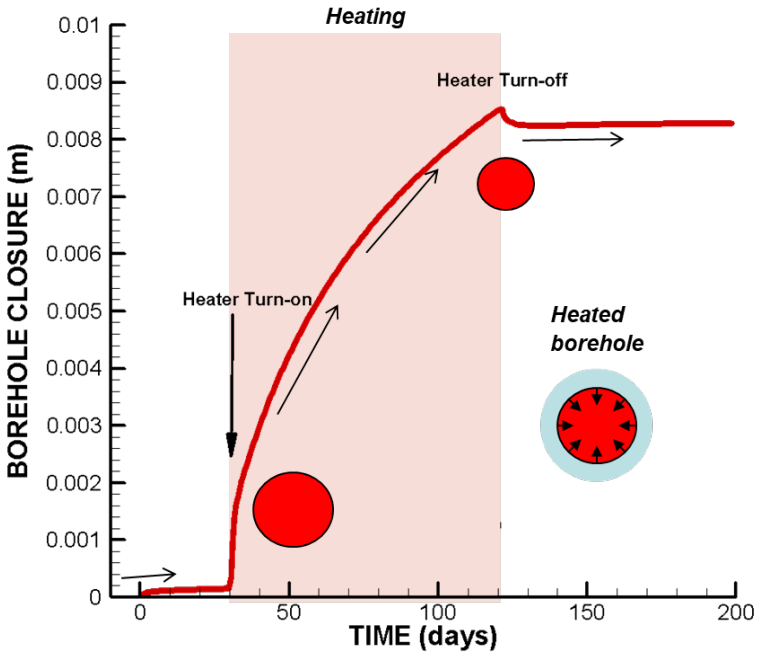

Figure 6-3. TOUGH-FLAC simulated borehole closure for a small-diameter borehole test at WIPP.

The brine-inflow rate shows a very complex behavior, associated with THM-induced changes (Figure 6-4). First, during the initial 30 days, the inflow rate goes toward a steady inflow rate of about 3-4 grams per day (per meter of a borehole length). This inflow rate is consistent with field observations at WIPP (Rutqvist et al., 2017; Kuhlman et al., 2018). Then there is a spike in inflow rate right after the heater turn-on. This spike is due to a combination of enhanced permeability induced by damage, increased pressure gradient by thermal pressurization, and perhaps reduction in fluid viscosity with temperature. Another spike in inflow rate occurring at about 50 days coincided with more extensive damage development around the borehole. Finally, it was found that the highest inflow rate occurred after turning off the heater at about 120 days. The coupled THM simulation showed that this cooling induced increase in inflow was due to extensive damage around the borehole that occurred as a result of development of cooling induced tensile stress.

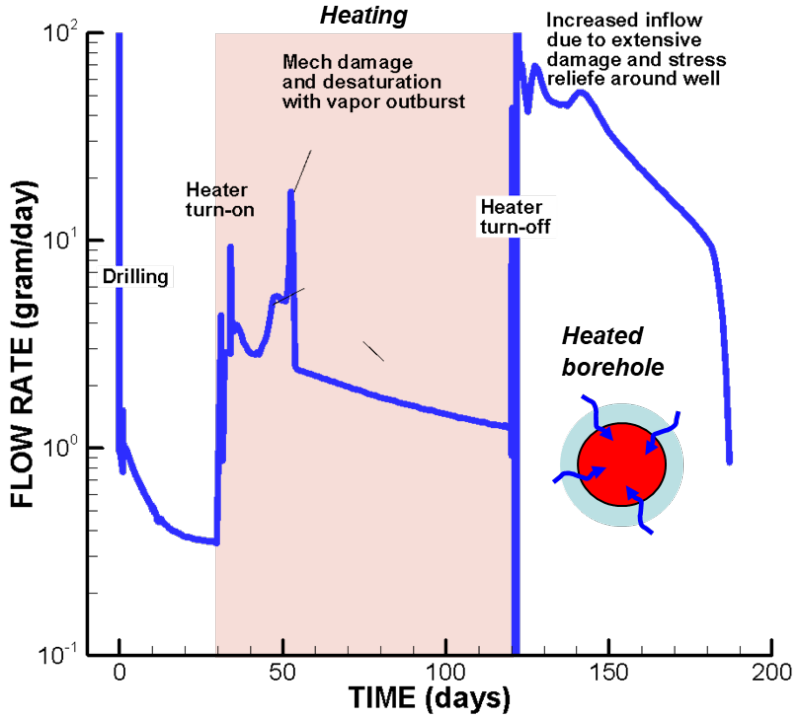

Figure 6-4. TOUGH-FLAC simulated brine inflow rate for a small-diameter borehole test at WIPP.

Figure 6-5 provides an explanation to how such tensile stress can be developed during cooling. The figure shows that a strong increase in tangential stress occurred near the borehole (at 0.067 m and 0.17 m radius) just after the heater was turned on. Such increase in tangential stress, while the radial stress remained low due to proximity to the open borehole, creates an increase in the deviatoric stress. This deviatoric stress induced creep that would tend to relax the thermally created deviatoric stress. Then, after the heater was turned off, cooling-induced tensile strain could have resulted in the tensile tangential stress near the borehole. The model simulations show that these stress changes are able to cause damage and enhance permeability at a distance as far as 1 m from the borehole (Rutqvist et al., 2017). This damage and spike in flow rate during cooling were simulated assuming a sudden heater turn-off, whereas a more gradual reduction of heat power could be applied to prevent such extensive cooling induced damage (Rutqvist et al., 2017).

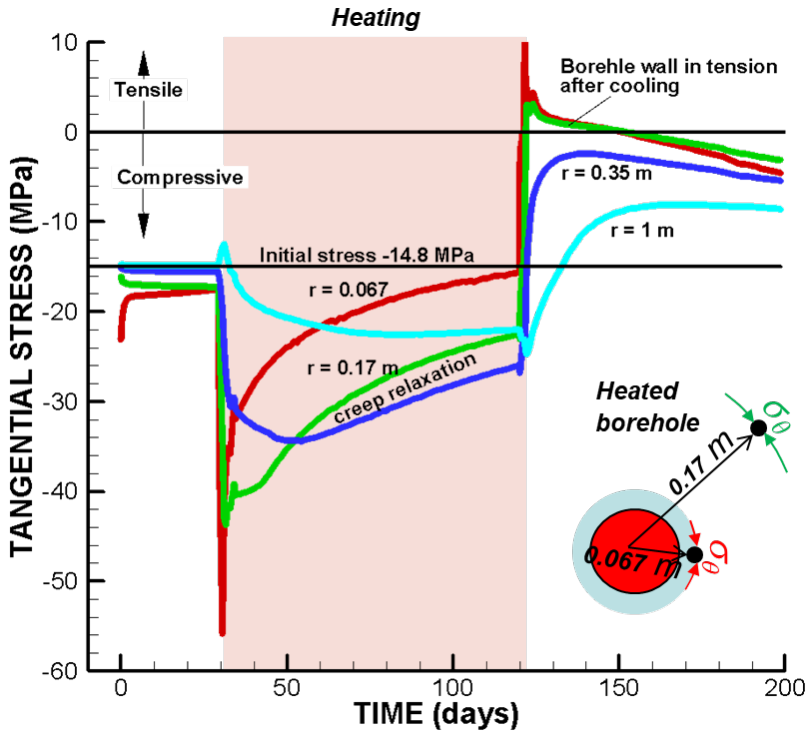

Figure 6-5. TOUGH-FLAC simulated tangential stress evolution at different radius for a small-diameter borehole test at WIPP.

6.4 Modeling Phase 1 shakedown test

The Phase 1 of the heated borehole experiments was conducted as a "shakedown" (Kulhman et al., 2018; Stauffer et al., 2019). Its purpose was to learn the logistical challenges of working underground at WIPP, while working through technical challenges in the field test design before the larger and more expensive Phase 2 experiment. The most important aspects of the Phase 1 experiments for model development have been the implementation of different heat sources and monitoring of water production during the tests. Modeling of the Phase 1 experiment showed early that temperature in the salt was substantially overestimated, assuming efficient thermal transfer from the heater to the borehole wall and into the salt formation (Stauffer et al., 2019).

Modeling of the shakedown experiment was conducted considering coupled temperature, fluid flow and geomechanics. The pre-test modeling described in Section 6.3 indicated that substantial creep closure of the borehole would occur along with heating. However, observations at the shakedown experiment did not indicate such behavior. Stauffer et al. (2019) found that the heat transfer from the heating element to the salt host rock was not very efficient. Increasing temperature of the heater to 120 °C only resulted in few degrees temperature changes at a distance of about 1 foot into the host rock. Stauffer et al. (2019), found that this could be simulated if assuming an insulating air-gap of low thermal conductivity between the heater and the host rock.

Here a similar approach is applied to simulate the temperature evolution as observed in the Phase 1 shakedown test. That is, a 2-D axisymmetric model is applied with a heater about 0.2 m long and with an air-gap of low thermal conductivity between the heater and the salt host rock. Temperature of the heater is set to 120°C. The air-gap thickness was determined based on the thickness of the numerical element and the thermal conductivity of the simulated air-gap, and calibration of model parameters was conducted based

on a reasonable match between simulated and observed temperature (Figure 6-6). The axisymmetric model was modified such that borehole diameter is 12.2 cm (4.8 inch). Moreover, in these model simulations some of the input parameters were set equal to those used in Stauffer et al. (2019) for their final modeling of the Phase 1 tests. That is, the salt host rock thermal conductivity $\lambda = 5.25$ W/mK, permeability $k = 1\times10^{-21}$ m^2, and porosity $\phi = 0.001$. These parameters are within the range of those in Table 6-2, except for the thermal conductivity, which is significantly higher. The modeling results also show that fluid pressure is not impacted by the temperature, i.e. no significant thermal pressurization impacts the inflow.

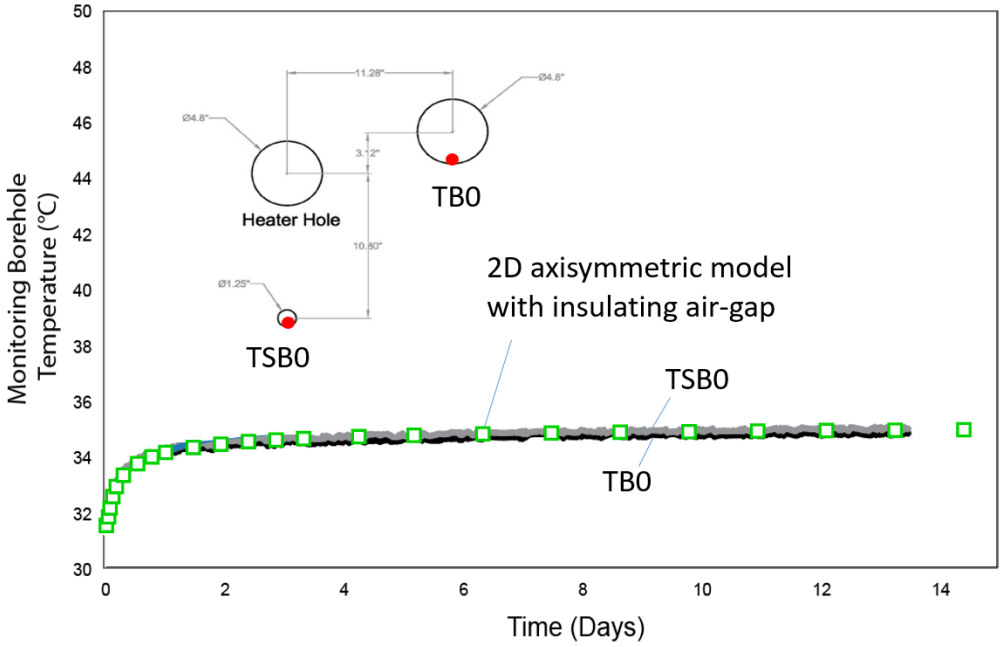

Figure 6-6. 2-D axial symmetric model results of temperature evolution at a point located at 24 cm radius, and comparison to observe temperatures at the Phase 1 borehole heater (Observed temperature from Stauffer et al., 2019).

Having achieved good agreement in the temperature field for the 2-D axial symmetric model, we conducted 1-D axial symmetric model simulations to be able to relate back to the results of strongly coupled thermo-hydro-mechanical responses predicted in Section 6-3. Again, a 120°C constant temperature is applied in the wellbore, an insulating air-gap is simulated in the model to match the observed temperature evolution at the two monitoring boreholes. In this case the shape of the temperature evolution is not in perfect agreement due to the 1-D axial symmetric simplification in modeling (Figure 6-7). However, the modeling consistently shows only a few degrees temperature increase at this distance of about 24 cm from the heater borehole.

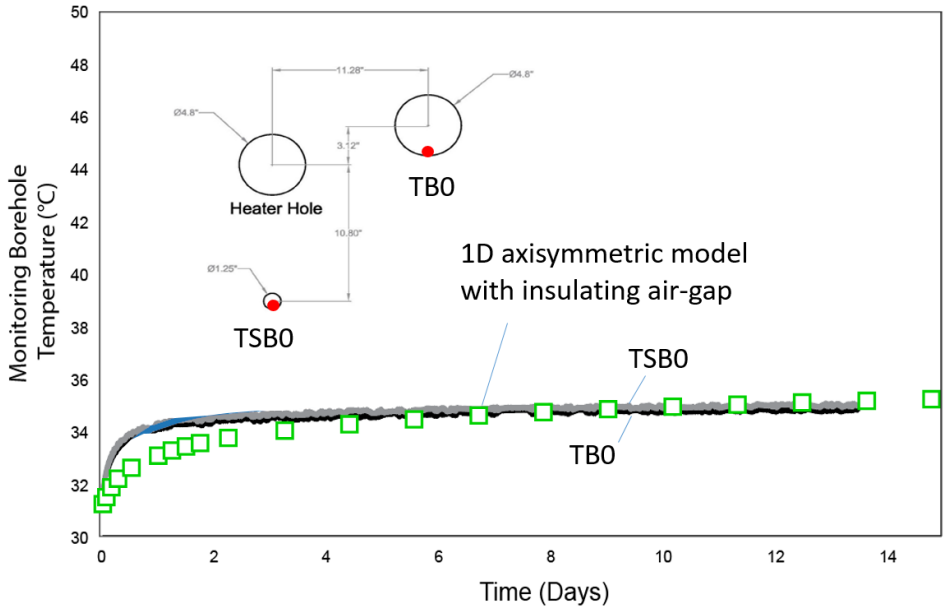

Figure 6-7. 1-D axial symmetric model results of the temperature evolution at a point at a 24 cm radius with comparison to observed temperature at the Phase 1 borehole heater test (Observed temperature from Stauffer et al., 2019).

Figures 6-8 through 6-10 show the evolution of temperature, fluid pressure, borehole closure and mass inflow. In these simulations the initial pressure was set to 12 MPa. The constant temperature heating of 120°C was applied instantaneously at time zero along with relative humidity of 30% in the well. This causes an initial high inflow rate that levels out and become steady at about 3 grams/day after 30 days (Figure 6-9b). Because the temperature increase within the host rock is minor, no significant thermal pressurization occurs (Figure 6-8). Moreover, the borehole closure is minor, less than 0.5 mm after 30 days (Figure 6-9a). This is consistent with field observations. The inflow rate is unaffected by thermal and mechanical effects and the cumulative inflow rate are in good agreement with field observations (Figure 6-10). The inflow rate was here calculated over a 1 m long borehole section (i.e. corresponding to the distance from the heater to the packer). Permeability was set to $k = 1\times10^{-21}$ m^2, and porosity $\phi = 0.001$. This is consistent with the results of Stauffer et al. (2019), who applied a full 3-D model, but with the same permeability and porosity values.

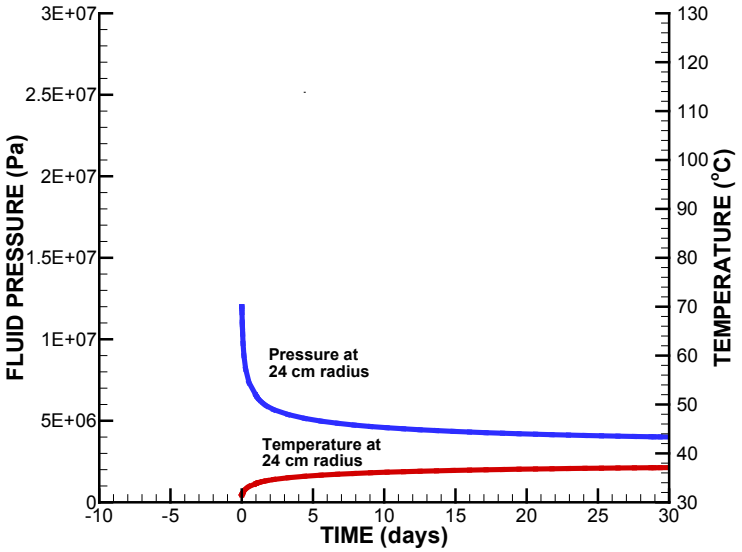

Figure 6-8. Simulation results of temperature and pressure at about 24 cm from the heated borehole.

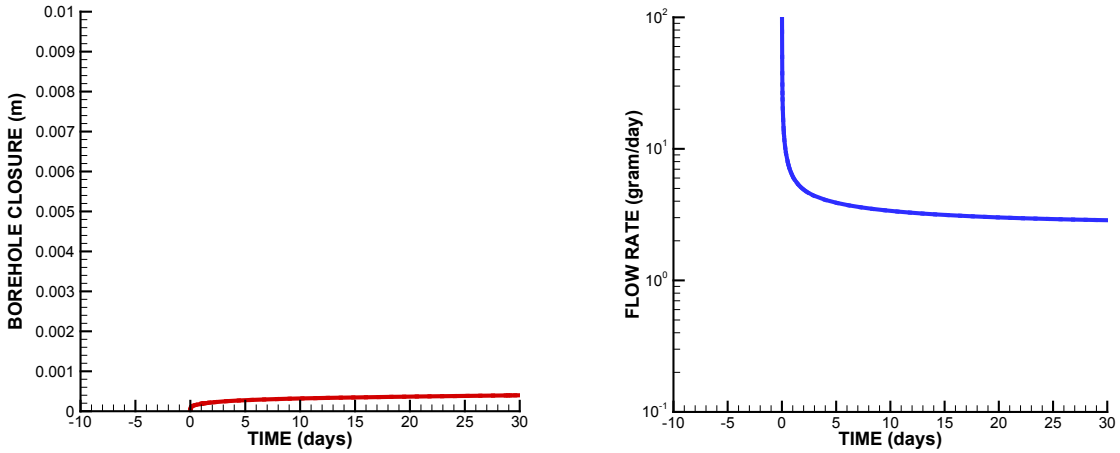

(a) (b)

Figure 6-9. Simulation results of (a) borehole closure, and (b) inflow rate for the Phase 1 borehole heater test.

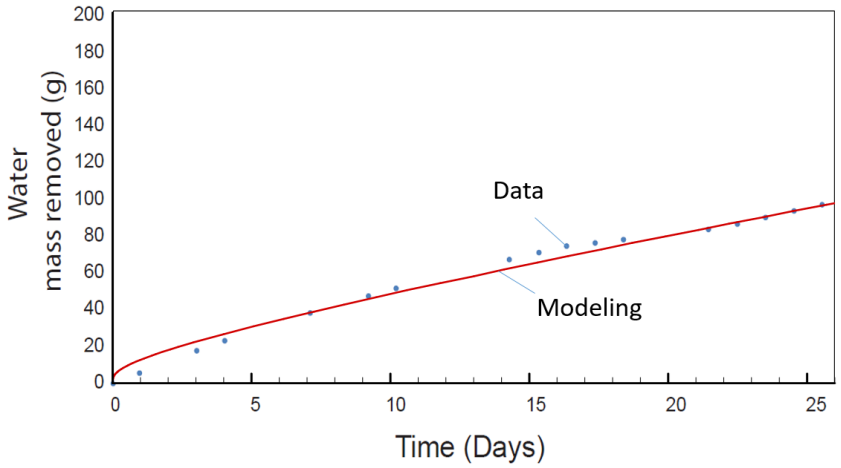

Figure 6-10. Simulated mass of water removed from the surrounding rock considering a 1 m long borehole sections with comparison to water mass removed from the borehole during the Phase 1 shakedown experiment (data from Stauffer et al., 2019).

6.5 Additional pre-test modeling of the Phase 2 experiment

The heater design has been updated for the Phase 2 experiment (Mills et al., 2019). A 750-Watt quartz lamp infrared heater will be mounted with disc-shaped reflectors installed on either end of the heater to confine the radiative energy to approximately an 18-in (45.7 cm) long interval of the borehole wall (Mills et al., 2019). Studies in the laboratory have shown that this heater is efficient for providing heat transfer into the host rock. Modeling conducted by Stauffer et al. (2019) using a full 3-D model indicated that a borehole temperature of up to 140 °C could be achieved with the 750-Watt heater.

A complementary model simulation was conducted with TOUGH2 using a 2-D axial symmetric model with a 40 cm heater element applied in the 12 cm diameter borehole. The heating schedule given in Section 6.3 was applied: 30 days open unheated borehole, followed by heating at a constant power of 750 W for 90 days. As in Stauffer et al. (2019), the thermal conductivity of the salt host rock was set to 5.25 W/mK. The results of the temperature evolution shown in Figure 6-11 shows that temperature in the borehole could reach 140 °C or greater. Moreover, at a distance of about 1 ft, temperature increased to over 70°C and to about 40°C about 1 m from the heater.

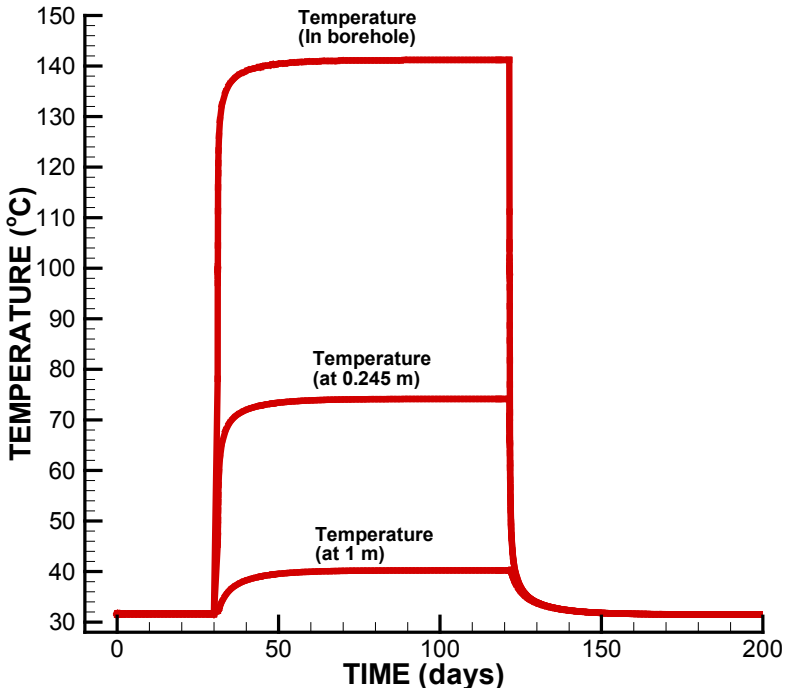

Figure 6-11. Results of 2-D axisymmetric temperature modeling for a 750-Watts 18-inch long heater leading to borehole temperature exceeding 140 °C.

The temperature distribution at the end of the 90-day heating period is shown in Figure 6-12. The fact that two independent models predict similar temperature evolution provides additional confidence in this pre-test modeling results.

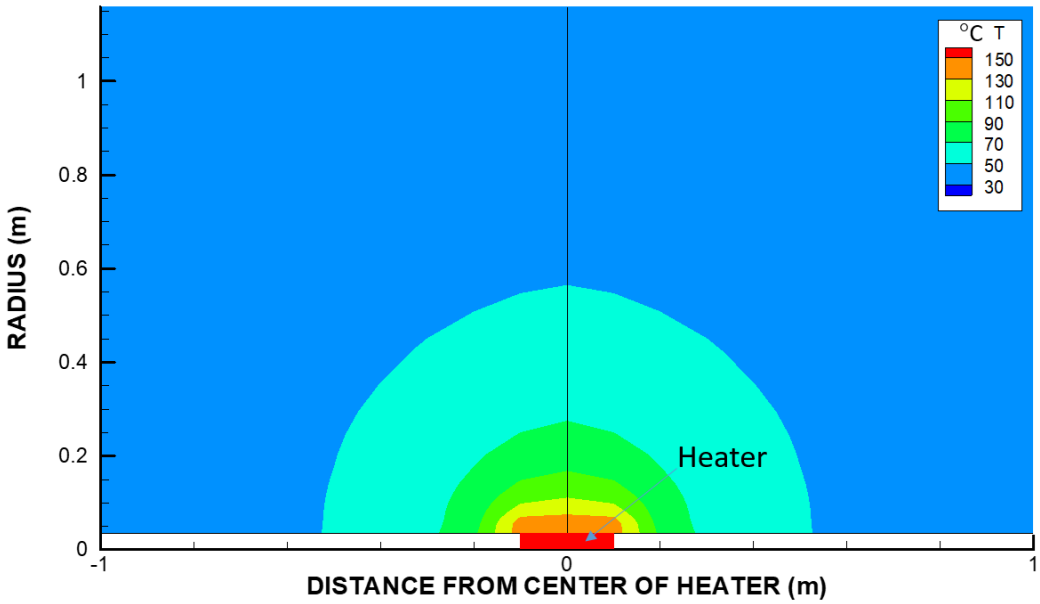

Figure 6-12. Temperature distribution at the end of the 90 days heating period based on 2-D axisymmetric modeling results for a 750-Watts 18-inch long heater.

Figure 6-13 shows the fluid pressure evolution indicating that thermal pressurization is quite minor for the assumed permeability k = 1×10^{-21} m^2 and porosity ϕ = 0.001. Comparison with Figure 6-2 shows that substantial thermal pressurization occurs in the case of a lower permeability and higher porosity. Overall, phenomena of substantial thermal pressurization in the field experiment remain uncertain.

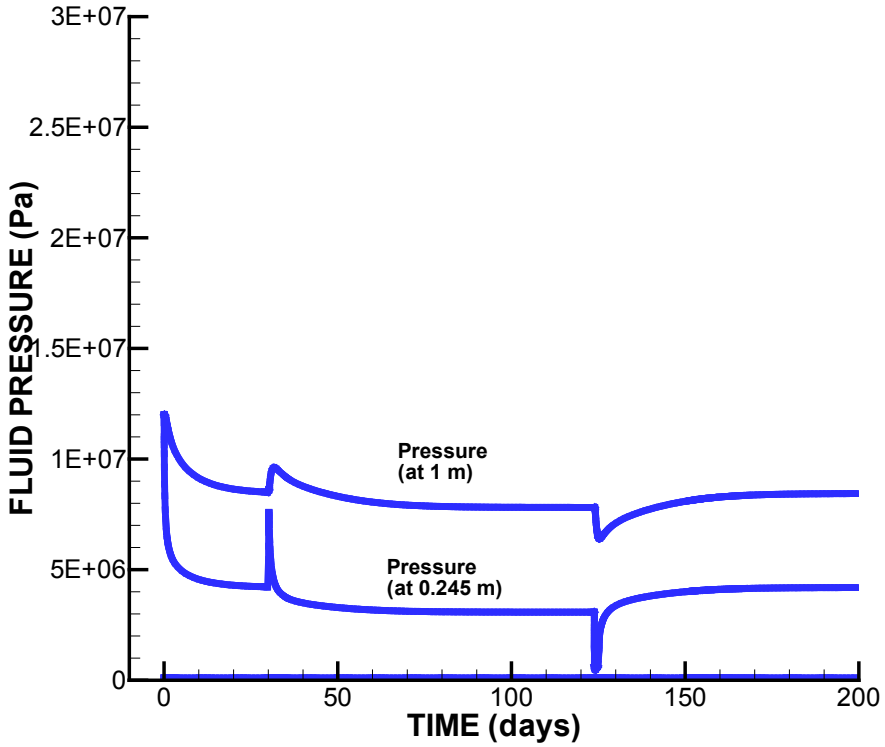

Figure 6-13. Pressure evolution from the results of 2-D axisymmetric modeling for a 750-Watts 18-inch long heater.

6.6 Discussion and Future Work on Heater Test Modeling

In general, the THM simulations of the heated borehole test indicate strong impact of mechanical changes on inflow, and a strong effect of the elevated temperature on the rate of the borehole closure. However, there are a number of uncertainties in the input material parameters, which can be better constrained by modeling of the actual experiment. For example, the initially connected intergranular porosity is uncertain, and its value may substantially impact the coupled THM processes related to thermal pressurization. If porosity is small, the pressure increase due to thermal pressurization will be smaller. Further, in this case the Biot's coefficient is assumed to be very low (0.003), as could be expected for salt. Its value will have a pronounce effect on whether poroelastic stress develops with pressurization and how the pores can deform with pressurization. This will impact the pressure increase caused by thermal pressurization. The change in permeability due to dilatancy is another factor that is expected to impact inflow during heating and cooling induced damage. These uncertainties can be reduced and material parameters can be better constrained by interpretative modeling of monitoring data at the planned small diameter test.

Related to monitoring, modeling shows that at the proposed monitoring boreholes located at about two radii from the test borehole, significant changes in pore pressure, stress and strain are expected to occur. The responses are expected to occur at the distance of r = 0.17 m. However, most strain occurs within one radius of the borehole and the dilatant strain in this region is causing most of the borehole closure. In the case of a low relative humidity in the borehole, drying will occur close to the borehole. Desaturation of the intergranular pores can also occur as a result of damage and associated dilation causing the increase in

porosity. The changes in the moisture content may cause significant resistivity changes that could be monitored using electric resistivity tomography (Rutqvist et al., 2017).

The heat power of 750 W for an 18-inch long heater could increase the borehole temperature to over 140°C. Modeling of coupled processes indicates that rapid changes in heat power (up or down) could cause an additional mechanical damage. Modeling will help assess how to prevent additional mechanical damage. Gas injection within the monitoring holes might be used to monitor how permeability of the halite changes with time, e.g., how long it will take for the salt rock to be sealed after a damaging event. Moreover, the closure rate under various temperatures is of relevance for the long-term salt host rock behavior. This experiment can provide a good opportunity to study creep under low deviatoric stress and borehole closure under the influence of temperature changes.

In terms of modeling, the 1-D and 2-D axisymmetric models are useful and efficient, but might be complemented with a full 3-D model of the site. This will be determined once the field data become available for interpretative modeling.

7. GEOPHYSICAL MONITORING OF THMC PROCESSES DURING SALT HEATER TESTING

7.1 Introduction to geophysical monitoring in salt

Geophysical monitoring of THMC processes in salt is challenging due to the inaccessibility of the formation around heat generating sources, the extremely low permeability, high ductility of the rock salt, and failure of electronic sensors in the high temperature environment.

In salt rock, the key thermo-hydrological processes induced by heat include strong mechanical deformations, brine migration, as well as formation and closure of fractures. Geophysical methods provide a way to better monitor THMC processes in rock salt formations, because they can be applied to remotely monitor the effects of heat generating sources. In addition, geophysical methods provide spatially and temporally dense datasets to be used for monitoring dynamic processes in heterogeneous media. As part of the SFWST program, we are developing geophysical methods for monitoring the THMC processes in salt rock at the Waste Isolation Pilot Plant (WIPP) during heater tests. For this report, we focus on electrical resistivity and optic fiber techniques based on distributed sensing methods. Before discussing results and update for the WIPP tests, a brief technical background for both of technologies is provided below.

7.1.1 Electrical Resistivity Method

Electrical resistivity signals are inherently dependent on hydrological properties – permeability and porosity, as well as a geochemical composition of media. Permeability change, pore fluid migration and brine inclusion movements and redistribution driven by thermal forcing can produce changes in electrical signals. A review of electrical resistivity methods can be found in Rubin and Hubbard, 2005; Atekawana and Slate, 2009. In salt formations, pore structure alteration induced by excavation and thermal stresses are taken place along with fluid migration and redistribution. Time lapse electrical studies have the capability to provide spatially distributed information on these processes. Changes in pore fluid ionic strength due to precipitation/dissolution and changes in temperature can also change electrical signatures. A geological material typically has a temperature coefficient of a few percent per degree depending on rock properties.

Electrical methods have been utilized in limited past studies to monitor brine migration in salt, for example in the Asse mine in Germany in a 2004-2007 experimental campaign (ADDIGAS, 2008). Brine migration was visualized in this study demonstrating the capability of the electrical resistivity method for brine tracer injection monitoring in rock salt formations. In our study, the electrical properties of WIPP salt rock was characterized in the lab at LBNL in previous studies, and the correlation between volumetric water content and electrical resistivity is shown below in Figure 7-1 (Stauffer et al., 2015).

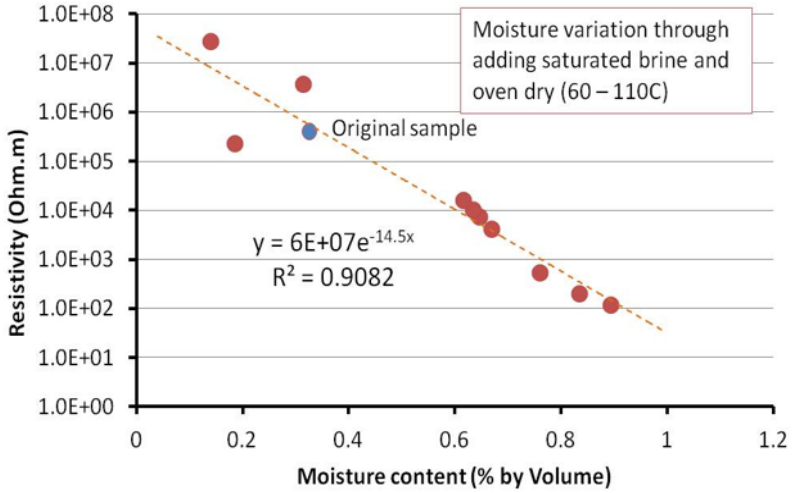

Figure 7-1. Relationship between the resistivity and moisture content for the WIPP salt rock.

Figure 7-1 indicates an inversed exponential relationship between the moisture content and resistivity (R^2>0.9). A five orders of magnitude increase in resistivity (from ~100 ohm.m to >10M ohm.m) were observed when the volumetric moisture content dropped from ~0.9% to 0.1%. Such a significant change in resistivity with a small variation of moisture content (within 1%) indicates a great sensitivity of resistivity to moisture content in WIPP rock salt.

7.1.2 Fiber Optic Sensing

Distributed fiber optic sensing to measure temperature and strain changes will also be applied during the WIPP heater test. LBNL has leading expertise in the application of fiber based distributed sensing approaches for various subsurface processes.

The development of optic fiber based distributed sensing can date back to the late 1980s starting with temperature applications. Initially developed at Southampton University and commercialized by York Systems. DTS is based upon changes in optical properties of commercial telecom fibers as a function of temperature, which can be detected by light from a laser pulse that is backscattered back to a detector at the beginning of the fiber. Over the course of 25 years the accuracy and spatial resolution of both Raman and Rayleigh based instruments have continued to improve, while costs for the surface electronics have also declined. The spatial resolution of a typical fiber detector based on Raman backscattering is 1 m, and new developments using Rayleigh scattering technology have resulted in much improved resolution (millimeter to centimeter) in recent years. For the WIPP heater experiment, Rayleigh based technology will be used with mm scale spatial resolution. For experiments that benefit from spatially density measurements, the advantages of DTS over tradition discrete sensors is readily apparent. Where each discrete temperature sensor such as a thermistor or resistance temperature detector (RTD) requires between 2 to 4 insulated copper conductors to be connected to a data logger or multiplexer, a distributed fiber-optic cable contains a glass strand the size of a hair that can provide thousands of measurements every few meters using Rayleigh technology. Limitations of the DTS arise from the difficulty in performing absolute calibrations on the systems response, which can vary as a function of laser diode performance within the DTS unit. The optical fiber coatings dictate the working temperature of the fibers. For installations at temperatures below 85 °C standard acrylate coatings are appropriate. A higher temperature acrylate coating is available for use at temperatures up to 150 °C. At temperatures beyond 150 °C and below 300 °C a polyimide coating is appropriate. The fiber optical cable that will be used at WIPP is based on polyimide coating that can be used in high temperature conditions. As part of LBNL's previous scoping studies to evaluate the application of distributed fiber-optics to monitor thermal processes in rock salt, a small heating experiment was set up.

A heater was used to apply uniform heating along the central vertical axis of the can. The temperature distribution measured using the fiber-optic technique compared well with the discrete RTD measurements.

7.2 Small Borehole Heater Test

Before the comprehensive heater test, a small borehole heater test was conducted on the draft floor close to the comprehensive test site to evaluate the feasibility of the electrical resistivity tomography approach for rock salt formations due to limited availability of existing data for WIPP site.

A schematic design of the test layout is shown in Figure 7-2. The left sub-figure shows the vertical cross section of the layout indicating the positions of the two ERT wells, and the two shallower wells between the ERT wells are used for heating and brine tracer injection test as indicated on the figure. The figures on the right show the actual layout of the boreholes on the draft floor as well as the distances between the boreholes. Note that due to the failure of the first attempt (heater-old) of the heater borehole where the heater malfunctioned, a second borehole (borehole – new) was installed and was functioning well for the test. In addition, there is a thermal couple borehole indicated on the right sub-figure as well. 5 thermo-couples were installed in the wells to track changes of formation temperature due to heating.

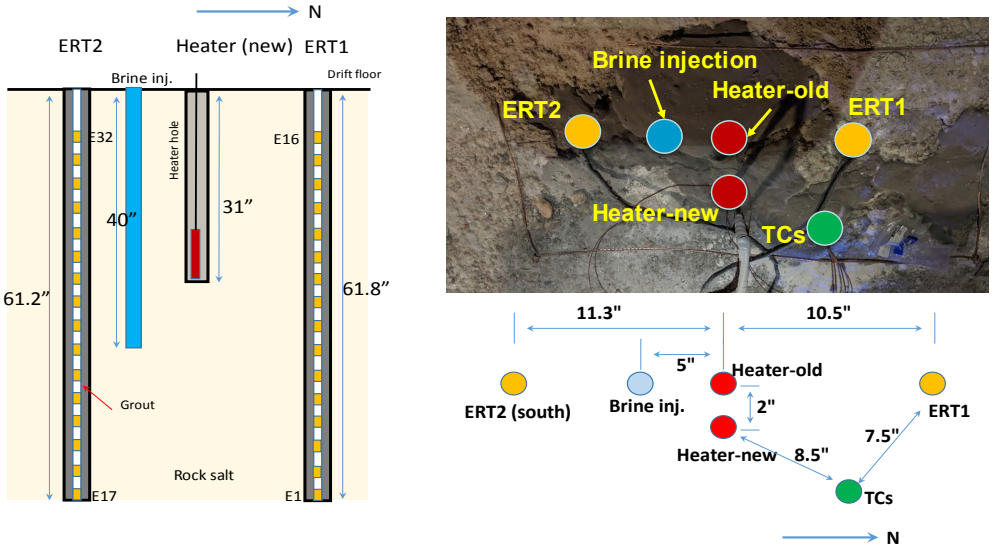

Figure 7-2. The configuration of the Electrical Resistivity Tomography (ERT) system during the small borehole tests. Left: vertical cross section of the setup; right: surface/top view of the setup showing the geometric arrangements and distances of the boreholes.

Except the brine injection borehole, all other boreholes were grouted to ensure good contact between the sensors or electrodes and the formation. The annulus of the electrode boreholes (between the PVC pipe and borehole wall) are filled with salt doped grout. The grout was left to cure for at least a month prior to beginning the test to ensure the electrodes have a good electrical connection with the salt. The MPT DAS-1 Electrical Impedance Tomography System is the ERT controller (Figure 7-3), and provide the current source and data acquisition routine. The heater temperature was targeted at 120 °C.

Figure 7-3. Photographs of MPT DAS-1 Electrical Impedance Tomography System that was used for ERT data acquisition.

Specifically, the primary objective of the experiments are as follows:

1. Evaluate the grouting method in terms of electrode/heater coupling with formation
2. Evaluate contact resistance between electrodes
3. Baseline electrical resistivity structure of the salt formation
4. Evaluate heater and controller performance
5. Monitor short-term resistivity change from heating and brine injection
6. Evaluate electrical safety hazard caused by active electrical current injection into the ground

Grouting of the ERT electrodes and the cartridge heater was carried out by pouring cement directly into the annulus of the boreholes after the PVC pipes were inserted. Based on the contact resistance tests, this grouting method seems to work fairly well in terms of providing good contacts between the electrodes. The contact resistance between the electrodes within the same borehole was mostly within a few hundred ohms, and those between the boreholes were mostly within 2K ohms, which suggests good coupling between the electrodes and the salt formation, as well as a low resistance of the rock salt formation. This is very encouraging given the expected low moisture content of the salt formation.

Two baseline ERT datasets were acquired before heater test commenced. Each data acquisition took about 1 hour with roughly 2000 data points. The processing of the acquired raw data requires the application of an inversion algorithm that computes resistivity models that match the observed potential field data. Due to the large contrast of the resistivity between rock salt and grout, the geometry of each component needs to be taken into consideration explicitly. Figure 7-4 shows the inversion model setup. The left figure shows the vertical cross section of the model; the top right figure shows the view from the surface; the middle figure shoes an enlarged view of the ERT borehole meshing; and the bottom right figure shows the resistivity values used for the different components of the model and their color representation in the figures. A roughly one order of magnitude difference in resistivity between rock salt and grout is applied based on laboratory measurements.

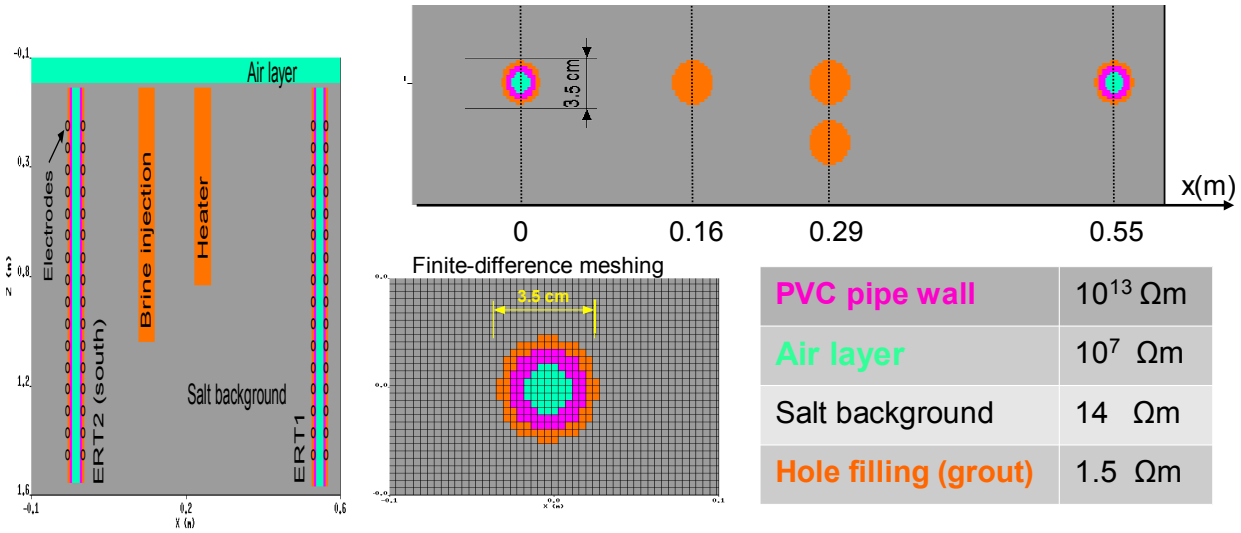

Figure 7-4. Numerical model setup for the inversion of the ERT datasets during the experiment.

The post-processing of the ERT data is carried out using the EMGeo code developed at LBNL, and was conducted in 3-D space. Once the correct model was established and initial QA/QC of data was performed. The processed data yields reasonable fitting of the model with the data. Figure 7-5 shows the baseline conductivity structure from ERT.

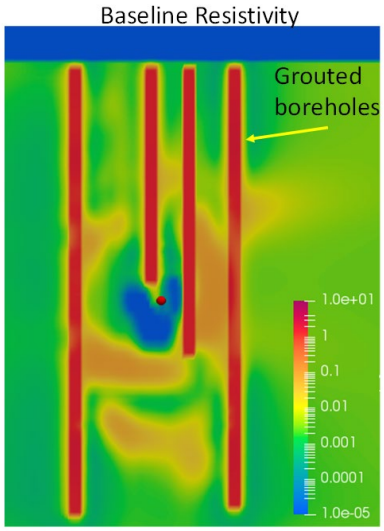

Figure 7-5. Baseline electrical conductivity (S/m) structure based on ERT inversion from baseline data acquisition before heating and brine injection experiment.

The warm colors in Figure 7-5 represent high electrical conductivity, and the locations of the grouted vertical boreholes are clearly indicated in the figure. Figure 7-5 also reveals heterogeneous distribution of the structure indicating potential fast flow pathways with potentially higher permeability for flow migration. Figure 7-6 shows a 3-D threshold view of the baseline conductivity structure highlighting the presence of the high conductivity features in the rock salt formation.

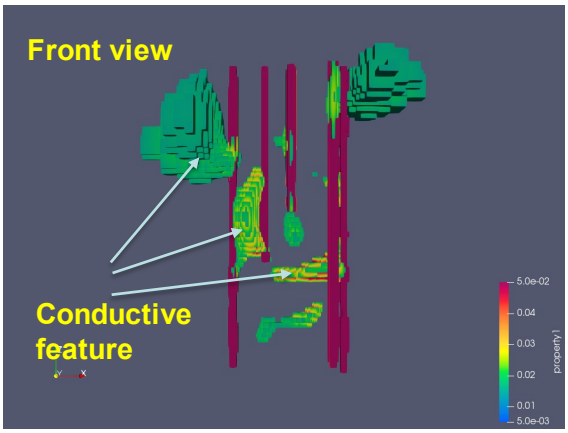

Figure 7-6. 3-D threshold view of the baseline electrical conductivity (S/m) structure highlighting the location of high conductivity features in the rock salt formation.

The interpreted ERT tomograms is expected show changes in resistivity distribution with time. Changes in apparent resistivity can be attributed to changes in temperature and brine content since salt heterogeneity and added metal equipment in the test should not change with time. ERT may be able to image an expanding dry-out region surrounding the heat source, especially if the salt temperature around the heater exceeds the brine boiling point (promoting dry-out).

Heating and brine injection experiments were conducted after the baseline data acquisition. Temperature of the heater was step-wise increased until the final test temperature of 120 °C was reached, and then kept constant for the duration of the experiment. The brine injection experiment was conducted while the heating was ongoing, but at steady state condition. For brine injection experiment, 990 ml of brine equilibrated with the WIPP salt overnight, and then was poured into the open borehole under no added injection pressure. Monitoring of the ERT data was carried out once every couple of hours. The discussion below will focus on the brine injection results since the change due to minimal heater test duration was small.

Figure 7-7 shows a comparison of the conductivity structure and the change of the conductivity due to brine injection that indicates brine pathways. As can be seen from Figure 7-7, the primary brine migration pathway followed a particular pattern that match well with the conductivity feature visualized in the baseline structure (left). This suggests the presence of a high permeability path in that particular direction, but not others, highlighting the capability of ERT in identifying preferential flow paths during tracer tests.

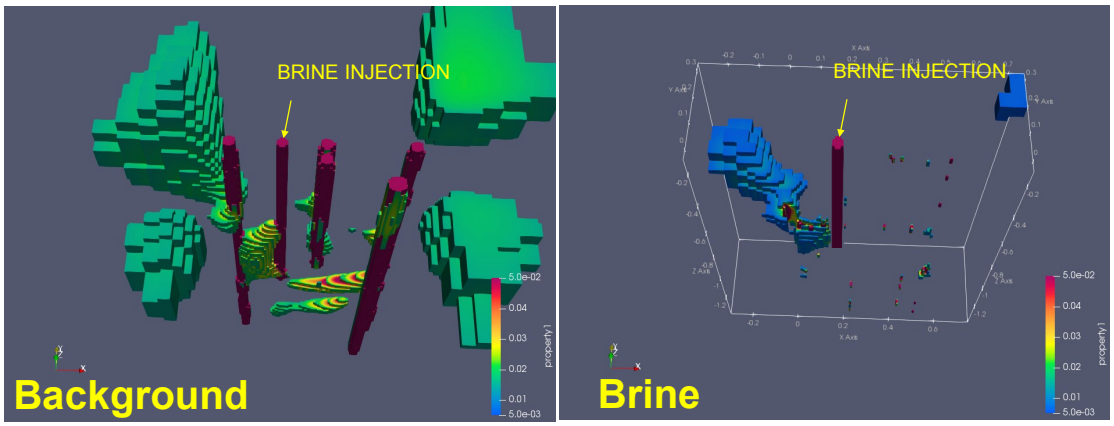

Figure 7-7. Comparison of the 3-D structures between the baseline conductivity features before brine injection and the geometry with increased conductivity indicating the brine migration pathway.

To further explore the type of information ERT can offer, a detailed visualization of brine migration pathway overlaid on top of the baseline structure is shown in Figure 7-8. Note that the baseline high conductivity feature is highlighted in dark red color, while the brine flow path is shown in green/blue. Note that the two vertical, high conductivity features represent two wellbores. The key feature highlighted in the figures is that the brine migration paths overlapped only with the top section of the high conductivity (dark red) feature between the wells, but not the bottom half. This suggests that only the top half of the formation likely has high permeability that allowed fast brine migration. While the bottom part has high conductivity, it didn't allow for brine migration to occur, suggesting a high conductivity, yet low hydraulic permeability feature. This is likely a compacted, low permeability clay rich feature, but direct validation is not available.

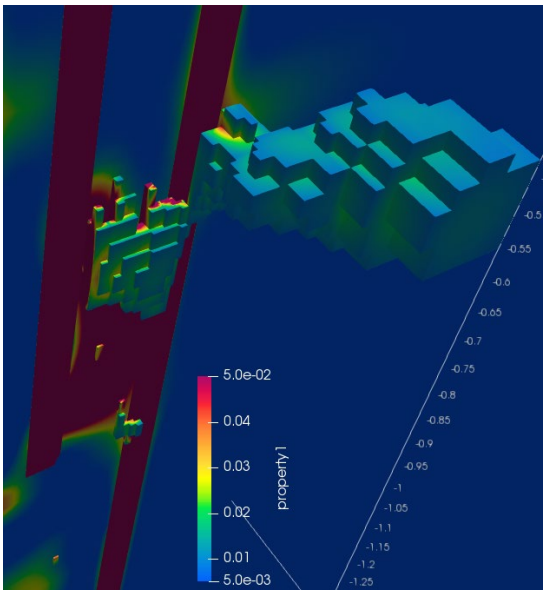

Figure 7-8. Overlap of the baseline conductivity structure (dark red) with the brine migration pathway (green/blue) highlighting the variability of the rock salt formation in their hydrological properties that have vast implications for brine migration pathway.

To briefly summarize what we have learned from the small borehole tests, we highlight the following conclusions:

- Field ERT monitoring visualized a 3-D resistivity structure of rock salt, suggesting possible flow paths,
- Significant change of electrical resistivity is observed due to variation in brine saturation suggesting great sensitivity of ERT for brine migration monitoring in rock salt,
- Brine tracer injection followed (partial) high conductivity feature confirming high permeability paths and
- Demonstrated ERT is a great visualization/monitoring tool for rock salt and brine migration processes.

7.3 Comprehensive heater test update

The small borehole ERT experiment discussed above provides a preliminary feasibility test in preparation for the comprehensive heater. For the comprehensive tests, two identical plots were setup with one as the "heater" plot, and the other as the unheated "control" plot. A diagram of the borehole layout for the plot is shown below in Figure 7-9.

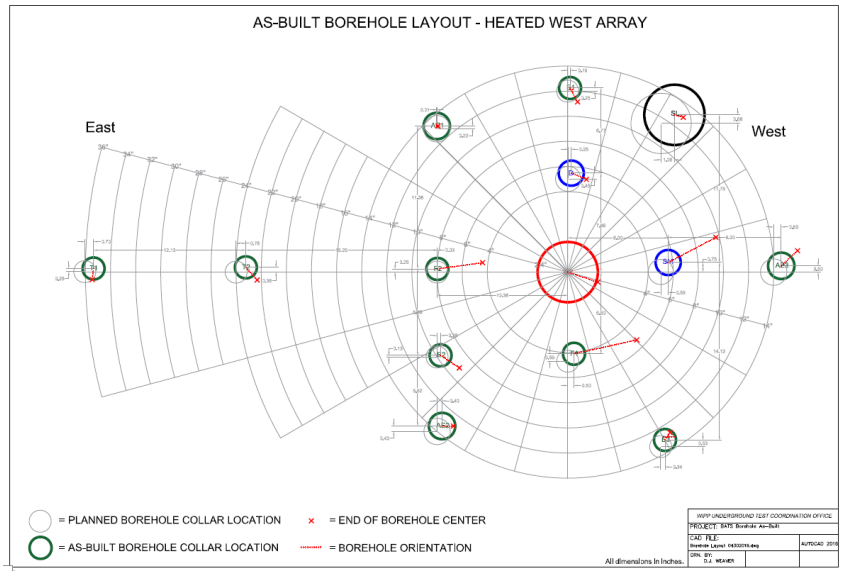

Figure 7-9. Borehole layout diagram for the comprehensive heater test experiment.

The boreholes installed for the experiments can be grouped into three groups: a heater hole, a sampling hole, and a set of monitoring holes. The largest central hole is used to house the heater via a packer system. The large borehole on the top right corner is the sampling borehole, which will also be used for tracer experiments. Amongst the monitoring boreholes, ERT, fiber optic, acoustic emission and thermal couple sensors will be installed to provide a comprehensive set of technologies to understand brine migration behavior during heating tests. Tracer tests will also be conducted to understand brine flow paths.

Figure 7-10 shows the actual borehole layout showing the position of the center heater hole and the ERT and fiber optic holes, which were completed in June 2019 with grout. The grout was injected, using a hand

pump, into the boreholes via the opening inside the PVC pipes used to host the sensors. Both the ERT and fiber sensors were installed by using 1" diameter PVC pipe. Similar to the small borehole test, 16 electrodes were installed for each ~20' borehole with a one foot spacing between adjacent electrodes. As a result, there are 48 total electrodes for each of the heated and unheated plots. A few thermocouples were installed for each of the ERT and fiber boreholes to provide discrete temperature measurements for either calibration or comparison. As for the fiber boreholes, due to the brittleness of the fiber sensor, Kapton tapes as well as electrical tapes were applied along the whole length of the fiber to protect sensor during subsequent grouting. This worked well as the tests after grouting indicated the proper working condition of the fiber sensors. Also note that two fiber optic sensors were installed in each borehole for separate strain and temperature measurements.

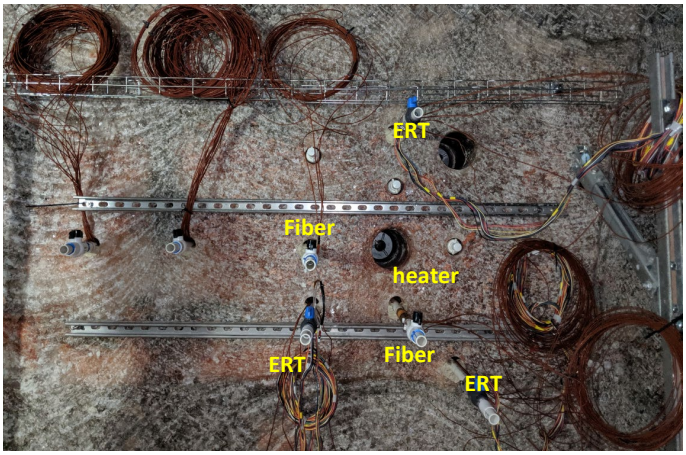

Figure 7-10. Picture of the borehole layout for the comprehensive heater test experiment, showing the position of the ERT and fiber boreholes that were completed in June 2019.

A close up view of the boreholes is shown below in Figure 7-11.

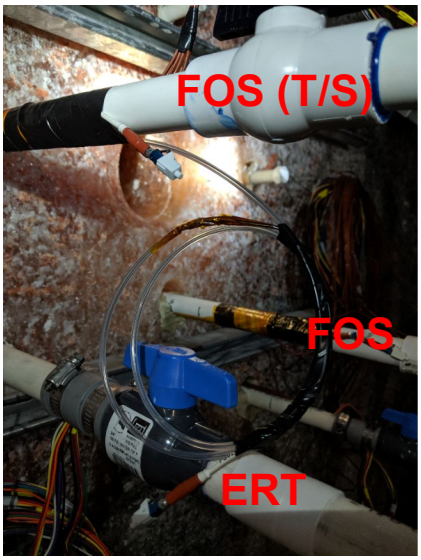

Figure 7-11. A close-up view of the ERT and fiber boreholes installed at the heater test site.

Currently, the sensors and instrument that need to be prepared for starting the experiment is close to be completed. Once the site is setup in terms of infrastructure, i.e., power, lighting, the experiments are ready

to start. Before starting the experiments, baseline datasets will be acquired to ensure every sensor is working properly and is producing reliable data. Currently, ongoing activity also includes numerical modeling studies for sensitivity analysis in order to design data acquisition algorithm with the most efficiency. These numerical tests will be completed before commencing the actual experiment.

8. SUMMARY OF FY19 PROGRESS AND FUTURE WORK

In FY19, LBNL's work on coupled Salt R&D have continued with the design and implementation of the small-diameter borehole test at WIPP in coloration with Sandia National Laboratories (SNL) and Los Alamos National Laboratory (LANL), with much more emphasis on field work in addition to the coupled THM modeling support. We have continued our international collaboration with Technical University of Clausthal (TUC) on upgrading TOUGH-FLAC with improved salt constitutive models, whereas most efforts have been focused on field work at WIPP for implementing geophysical monitoring methods and on modeling the small-diameter diameter borehole test. Some of the progress highlights are as follows:

- TOUGH-FLAC has been upgraded to latest versions of the respective TOUGH and FLAC^{3D} software and newly updated salt constitutive models from TUC implement and tested.
- The dual-continuum model for considering brine-inclusion migration has been completed, verified, and is ready to be tested using experimental data.
- TOUGH-FLAC are being tested and verified within the international BenVaSim project, providing confidence building especially related to the accuracy of the sequential coupling approach.
- Coupled THM modeling of the small-diameter borehole experiment at WIPP has been completed for Phase I (shake-down tests) and for pre-test modeling of Phase II.
- Through field investigation at WIPP, we have demonstrated ERT is a great visualization and monitoring tool for rock salt and brine migration processes
- ERT and fiber optics have been installed in the small-diameter borehole for geophysical monitoring of coupled processes during the upcoming heating experiment.

In FY20 we expect to work intensively with the small-diameter borehole test at WIPP in coloration with Sandia National Laboratories (SNL) and Los Alamos National Laboratory (LANL), including field work for geophysical monitoring and interpretative coupled processes modeling of the experiment. At the same time, LBNL will continue international collaboration with TUC and BenVaSim for testing and validation of the TOUGH-FLAC simulator. The small-diameter experiment at WIPP will provide a very important data set for validation of numerical models, including for processes related to brine migration, heat transfer and mechanical deformations.

This page is deliberately left blank.

9. ACKNOWLEDGMENTS

This work was supported by the Spent Fuel and Waste Disposition Campaign, Office of Nuclear Energy, of the U.S. Department of Energy under Contract Number DE-AC02-05CH11231 with Lawrence Berkeley National Laboratory.

This page intentionally left blank.

10. REFERENCES

ADDIGAS, Advective and Diffuse Gas Transport in Rock Salt Formations, Final Report, GRS, 2008

Anthony T.R., and Cline H.E. (1971) The thermal migration of liquid droplets through solids, *Journal of Applied Physics*, 42:3380–3387.

Atekwana E.A. and Slater L.D. (2009) Biogeophysics - A new frontier in Earth science research, reviews of geophysics, 47, RG4004 Battistelli A., Calore C., Pruess K. (1997) The simulator TOUGH2/EWASG for modelling geothermal reservoirs with brines and a non-condensible gas. *Geothermics*, 26(4): 437-464.

Battistelli A. (2012) Improving the treatment of saline brines in EWASG for the simulation of hydrothermal systems. In Proceedings TOUGH Symposium 2012, Berkeley, 17-19 September 2012.

Benz T. (2007) Small-strain stiffness of soils and its numerical consequences. Ph.D. thesis: University of Stuttgart (Germany).

Beauheim R.L., Ait-Chalal A., Vouille G., Tijani S.-M., McTigue D.F., Brun-Yaba C., Hassanizadeh S.M., van der Gissen G.M., Holtman H., and Mollema P.N. (1997) INTRAVAL Phase 2 WIPP 1 Test Case Report: Modeling of Brine Flow Through Halite at the Waste Isolation Pilot Plant Site. SAND97-0788. Albuquerque, NM: Sandia National Laboratories.

Biot M.A. (1941) General theory of three dimensional consolidation. *Journal of Applied Physics*.12:155–164.

Birkholzer J.T., and Rouvé G. (1994) Dual-continuum modeling of contaminant transport in fractured formations, In: Computational Methods in Water Resources X, A. Peters et al. (eds.), Kluwer Academic Publishers, Amsterdam, The Netherlands.

Blanco-Martín L., Rutqvist J., and Birkholzer J.T. (2015a) Long-term modelling of the thermal-hydraulic-mechanical response of a generic salt repository for heat-generating nuclear waste. *Engineering Geology*, 193, 198–211.

Blanco-Martín L., Wolters R., Rutqvist J., Lux K.-H., and Birkholzer J.T. (2015b) Comparison of two simulators to investigate thermal-hydraulic-mechanical processes related to nuclear waste isolation in saliniferous formations. *Computers and Geotechnics*, 66, 219–229.

Blanco-Martín L., Wolters R., Rutqvist J., Lux K.-H., and Birkholzer J.T. (2016) Thermal–hydraulic–mechanical modeling of a large-scale heater test to investigate rock salt and crushed salt behavior under repository conditions for heat-generating nuclear waste. *Computers and Geotechnics*, 77, 120–133.

Blanco-Martín L., Rutqvist J., and Birkholzer J.T. (2017) Extension of TOUGH-FLAC to the finite strain framework. *Comput. Geosci*, 108, 64-71.

Blanco-Martín L., Rutqvist J., Battistelli A., and Birkholzer J.T. (2018) Coupled Processes Modeling in Rock Salt and Crushed Salt Including Halite Solubility Constraints: Application to Disposal of Heat-Generating Nuclear Waste. Transp Porous Med 124:159–182.

Callahan G.D., and DeVries K.L. (1991) Analyses of Backfilled Transuranic Waste Disposal Rooms. Report SAND-91-7052: RE/SPEC Inc. (Prepared for Sandia National Laboratories), Rapid City, SD (USA).

Caporuscio, F.A., Boukhalfa, H., Cheshire, M.C., Jordan, A.B., and Ding, M. (2013) Brine migration experimental studies for salt repositories, LA-UR-13-27240, Los Alamos National Laboratory, Los Alamos, NM. Coussy O., 2004. Poromechanics. 1st ed. Chichester: John Wiley and Sons.

Dean R.H., Gai X., Stone C.M., and Minkoff S.E. (2006) A comparison of techniques for coupling porous flow and geomechanics. *SPE J*,11(1):132–40.

Doughty C. (1999) Investigation of conceptual and numerical approaches for evaluating moisture, gas, chemical, and heat transport in fractured unsaturated rock. J. Contam. *Hydrol* 38 (1– 3), 69– 106.

Hansen F.D. (2003) The Disturbed Rock Zone at the Waste Isolation Pilot Plant. SAND2003-3407, Albuquerque, NM: Sandia National Laboratories.

Hermann W., Wawersik W.R., and Lauson H.S. (1980a) Analysis of Steady State Creep of Southeastern New Mexico Bedded Salt, Sandia National Laboratories, SAND80-0558.

Hermann W., Wawersik W.R., and Lauson H.S. (1980b) Creep Curves and Fitting Parameters for Southeastern New Mexico Rock Salt, Sandia National Laboratories, SAND80-0087.

Hou Z. (2003) Mechanical and hydraulic behaviour of rock salt in the excavation disturbed zone around underground facilities. *International Journal of Rock Mechanics and Mining Sciences*, 40, 725-738. doi:10.1016/S1365-1609(03)00064-9.

Hou Z., Lux, and K.H. (1998) Ein neues Stoffmodell für duktile Salzgesteine mit Einbeziehung von Gefügeschädigung und tertiärem Kriechen auf der Grundlage der Continuum-Damage-Mechanik. *Geotechnik,* 21(3), 259–263.

Hou Z., Lux K.H., and Duesterloh U. (1998) Bruchkriterium und Fließmodell für ductile Salzgesteine bei kurzzeitiger Beanspruchung. *Glueckauf-Forschungshefte*, 59(2), 59–67.

Hou Z., and Lux K.H. (1999) A constitutive model for rock salt including structural damages as well as practice-oriented applications. In: Proceedings of the Fifth Conference on the Mechanical Behaviour of Salt, Bucharest, Romania, 151–169.

Hou Z., and Lux K.H. (2000) Ein Schädigungsmodell mit Kriechbruchkriterium für duktile Salzgesteine auf der Grundlage der Continuum- Damage-Mechanik. *Bauingenieur*, 75(13), 300–307.

Itasca. (2011) FLAC^{3D} (Fast Lagrangian Analysis of Continua in 3 Dimensions), Version 5.0. Minneapolis: Itasca Consulting Group.

Johnson P.J., Boukhalfa H., Weaver D.J., Otto S., Dozier B.L., Stauffer P.H., Mills M.M., Matteo E.N., Kuhlman K.L., Rutqvist J., and Wu Y. (2018) Test Plan Document for Thermal Testing in Salt Test Plan, TP-18-001-REVISION 0LA-UR-17-30762, DMS-SFWD-SFWST-2017-000043.

Jung Y et al. (2017) TOUGH3: A new efficient version of the TOUGH suite of multiphase flow and transport simulators, *Comput. Geosci.*, 108, 2-7.

Kachanov L.M. (1986) Introduction to Continuum Damage Mechanics. 1st ed. Dordrecht: Martinus Nijhoff Publishers.

Kim J., Tchelepi H.A., and Juanes R. (2011) Stability and convergence of sequential methods for coupled flow and geomechanics: fixed-stress and fixed-strain splits. *Comput. Methods Appl. Mech. Eng.,* 200 (13-16), 1591–1606. http://dx.doi.org/10.1016/j.cma.2010.12.022.

Kim J., Sonnenthal E., and Rutqvist J. (2012) A modeling and sequential numerical algorithms of coupled fluid/heat flow and geomechanics for multiple porosity materials. *International Journal of. Numerical. Methods in Engineering*, 92, 425–456.

Kim J., Tchelepi H.A., and Juanes R. (2013) Rigorous coupling of geomechanics and multiphase flow with strong capillarity. SPE J. 18 (6), 1123–1139.

Kuhlman, K. L., M. M. Mills, C. G. Herrick, E. N. Matteo, P. Stuaffer, P. Johnson, H. Boukhalfa, D. Weaver, J. Rutqvist, and Y. Wu (2018), Project Plan: Salt in Situ Heater Test, Sandia National Laboratory, Report: SAND-2018-4673R

Lux K.H. (1984) Gebirgsmechanischer Entwurf und Felderfahrung im Salzkavernenbau: Ein Beitrag zur Entwicklung von Prognosemodellen für den Hohlraumbau im duktilen Salzgebirge. 1st ed. Stuttgart: Ferdinand Enke Verlag.

Lux K.H., Lerche S., and Dyogtyev O. (2018). Intense damage processes in salt rock- a new approach for laboratory investigations, physical modelling and numerical simulation. In proceedings Mechanical Behavior of Salt IX, Hannover, Germany, 12-14 September, 2018.

Mills M., Kuhlman K., Matteo E., Herrick C., Nemer M., Heath J., Xiong Y., Paul M., Stauffer P., Boukhalfa H., Guiltinan E., Rahn T., Weaver D., Dozier B., Otto S., Rutqvist J., Wu Y., Ajo-Franklin J., and Hu M. (2019) Salt Heater Test (FY19) SAND2019-4814 R., Sandia National Laboratories.

Munson D.E. (1997) Constitutive model of creep in rock salt applied to underground room closure, International Journal of Rock Mechanics and Mining Sciences, 34 (2), 233–247.

Munson D.E., and Dawson P.R. (1984) Salt Constitutive Modeling Using Mechanism Maps. The Mechanical Behavior of Salt, Proceedings of the First Conference, Penn M. Langer. Clausthal-Zellerfeld, Germany: Trans Tech Publications. 717-737.

Nutt M. (2012) Used Fuel Disposition Campaign Disposal Research and Development Roadmap (FCRD-USED-2011-000065 REV0), U.S. DOE Used Fuel Disposition Campaign.

Olivella S., Carrera J., Gens A., and Alonso E.E. (1994) Nonisothermal multiphase flow of brine and gas through saline media, *Transport in Porous Media*, 15:271–293.

Pruess K., Oldenburg C., and Moridis G. (2012) TOUGH2 User's Guide, version 2.1. Berkeley: Lawrence Berkeley Natl Lab [Rep LBNL-43134 (revised)].

Ratigan J.L. (1984) A finite element formulation for brine transport in rock salt, *International Journal For Numerical And Analytical Methods In Geomechanics*, 8: 225-241.

Roberts R.M., Beauheim R.L., and Domski P.S. (1999) Hydraulic Testing of the Salado Formation Evaporites at the Waste Isolation Pilot Plant: Final Report. SAND98-2537, Albuquerque, NM: Sandia National Laboratories.

Rubin, Y. and Hubbard S. (eds) (2005) Hydrogeophysics, Springer, The Netherland

Rutenberg M., Feierabend J., Lux K.-H.1, Maßmannn J., Sentís M. L., Graupner B. J., Hansmann J., Czaikowski O., Wieczorek K., Friedenberg L., Hotzel S., Kock I., Rutqvist J., Mengsu Hu M., and Rinaldi A.P. (2018) BENVASIM—A Benchmarking of simulators for modeling TH2M processes in the context of radioactive waste disposal. In Proceedings TOUGH Symposium 2018, Berkeley, 8-10 October 2018.

Rutqvist J. (2011) Status of the TOUGH-FLAC simulator and recent applications related to coupled fluid flow and crustal deformations. *Computers & Geosciences*, 37, 739–750.

Rutqvist J. (2017) An overview of TOUGH-based geomechanics models. Comput. Geosci. 108, 56-63.

Rutqvist J., Blanco Martín L., and Houseworth J. (2012) THM Coupled Process Modeling with TOUGHFLAC to Evaluate the Fate and Transport of Water in a Salt-Based Repository. Report FCRD-UFD-2012-000297.

Rutqvist J., Blanco Martín L., Kim J., Birkholzer J.T. (2013) Modeling Coupled THMC Processes and Brine Migration in Salt at High Temperatures. Report FCRD-UFD-2013-000262.

Rutqvist J., Wu Y.S., Tsang C.F., Bodvarsson G. (2002) A Modeling Approach for Analysis of Coupled Multiphase Fluid Flow, Heat Transfer, and Deformation in Fractured Porous Rock. Int. J. Rock Mech. Min. Sci., 39: 428-442.

Rutqvist J., Blanco Martín L., Mukhopadhyay S., Houseworth J., and Birkholzer J. (2014) Modeling Coupled THMC Processes and Brine Migration in Salt at High Temperatures, LBNL-6718E, Lawrence Berkeley National Laboratory.

Rutqvist J., Blanco Martin L., Molins S., Trebotich D., and Birkholzer J. (2015) Modeling Coupled THMC Processes and Brine Migration in Salt at High Temperatures. Prepared for U.S. Department of Energy, Used Fuel Disposition, FCRD-UFD-2015-000366, LBNL-191216, Lawrence Berkeley National Laboratory.

Rutqvist J., Blanco-Martin L., Hu M., Molins S., Trebotich D., and Birkholzer J. (2016) Modeling Coupled THMC Processes and Brine Migration in Salt at High Temperatures. Prepared for U.S. Department of Energy, Used Fuel Disposition, FCRD-UFD-2016-000439, LBNL-1006308, Lawrence Berkeley National Laboratory.

Rutqvist J., Blanco-Martin L., Hu M., and Birkholzer J. (2017) Coupled THM Modeling In Support of a Phased Salt Field Test Plan. Prepared for U.S. Department of Energy, Spent Fuel and Waste Disposition, SFWD-SFWST-2017-000103, LBNL-2001023, Lawrence Berkeley National Laboratory.

Rutqvist J., Hu M., Wu Y., Blanco-Martín L., Birkholzer J. (2018) Salt Coupled THMC Processes Research Activities at LBNL: FY2018 Progress. Prepared for U.S. Department of Energy, Spent Fuel and Waste Disposition, Prepared for U.S. Department of Energy, Spent Fuel and Waste Disposition, LBNL-2001170, Lawrence Berkeley National Laboratory.

Rycroft C.H. (2009) Voro++: a three-dimensional Voronoi cell library in C++. http://math.lbl.gov/voro++/.

Senseny P.E. (1985) Determination of a Constitutive Law for Salt at Elevated Temperature and Pressure. American Society for Testing and Materials, Reprint 869.

Silva O., Carrera J., Dentz M., Kumar S., Alcolea A., and Willmann M. (2009) A general real-time formulation for multi-rate mass transfer Problems, *Hydrology And Earth System Sciences*, 13: 1399-1411.

Sjaardema G.D., and Krieg R.D. (1987) A Constitutive Model for the Consolidation of WIPP Crushed Salt and It's Use in Analyses of Backfilled Shaft and Drift Configurations. Report SAND-87-1987: Sandia National Laboratories, Albuquerque, NM (USA).

Stauffer P.H., Jordan A.B., Weaver D.J., Caporuscio F.A., Ten Cate J.A., Boukhalfa H., Robinson B.A., Sassani D.C., Kuhlman K.L., Hardin E.L., Sevougian S.D., MacKinnon R.J., Wu Y., Daley T.A., Freifeld B.M., Cook P.J., Rutqvist J., and Birkholzer J.T. (2015) Test Proposal Document for Phased Field Thermal Testing in Salt. LA-UR-15-23154, FCRD-UFD-2015-000077. Los Alamos, NM: Los Alamos National Laboratory.

Stauffer, P. H., Guiltinan, E. J., Bourret, S. M., and Zyvoloski, G. A. (2019) Salt thermal testing in heated boreholes: Experiments and simulations. LA-UR-19-22729, Los Alamos National Laboratory, Los Alamos, NM.

Wang Y. (2011) Research & Development (R&D). Plan for Used Fuel Disposition Campaign (UFDC). Natural System Evaluation and Tool Development, U.S. DOE Used Fuel Disposition Campaign.

Wolters R., Lux K.H., and Düsterloh U. (2012) Evaluation of Rock Salt Barriers with Respect to Tightness: Influence of Thermomechanical Damage, Fluid Infiltration and Sealing/Healing. In: Proc 7th Int Conf Mech Behav Salt (SaltMech7), Paris, 425-434.

Wu, Y.S., and Pruess K. (1988) A multiple-porosity method for simulation of naturally fractured petroleum reservoirs, *SPE Reservoir Engineering*, 3:327-336.